TIME-REVERSAL FOR TIME-VARYING ACOUSTIC COMMUNICATIONS AND A SIMPLE CHANNEL ESTIMATOR

by

Nitisha Sharma

Submitted in partial fulfillment of the requirements
for the degree of Master of Applied Science

at

Dalhousie University
Halifax, Nova Scotia
December 2018

Table of Contents

List of Tables

List of Figures

Abstract

This research work studies and designs a proposed single-input-multiple-output (SIMO) OFDM communications system in MATLAB/Simulink environment, which discusses performance of time-reversal processing on a set of acoustic channels. The test channels for simulations are generated through Bellhop and a MATLAB script. This thesis also studies and analyzes a real experiment from literature using Bellhop to understand why time-reversal worked so well in that particular experiment. Finally, this work develops a basic channel estimator to study its performance in the designed Simulink based communication model.

OFDM signaling is used to accommodate equalization of frequency-selective fading allowing for simple channel equalization as well as the efficient modulation and demodulation via the fast Fourier transform. Repetition encoder/decoder of low rate is used as an error-control measure to combat interference and other adversities in acoustic channels. Multiple data streams are superimposed before transmission in order to enhance spectral efficiency. Iterative decoding and demodulation is applied to iteratively minimize the inter-carrier-interference caused due to the effects of Doppler in time-varying channels and to ultimately recover the original data streams.

Acknowledgements

My journey through this masters has not been easy and I would not have been able to make it this far without support. I would like to thank each individual who has played their parts in this journey and helped me accomplish this goal. My sincere thanks to all my teachers, Prof. Christian Schlegel, family/friends and colleagues, especially Ali Bassam for his readiness for discussions. Finally, a profound gratitude and thanks to Mr. David M. Dzidzornu, Schulich School of Law, Dalhousie University, for his constant support and encouragement through tough times.

Chapter 1

Introduction

The underwater acoustic (UWA) channel is recognized as one of the most difficult communication media in use today. The main factors that account for its difficulty are the time-varying nature of the channel, limited bandwidth for acoustic signals (1 kHz to 50 kHz) due to severe frequency-dependent attenuation of the physical medium, the low speed of sound in water (about 1500 m/s), delay spread at the receiver due to multipath propagation, and the almost unavoidable relative motion between the transmitter and the receiver resulting in Doppler effects.

The multipath effect in an underwater channel (UWC) introduces frequency-selective fading of the original signal and causes inter-symbol interference (ISI) in the received signal. The longer the channel delay-spread, the more ISI. Due to this multipath nature of the UWC, the transmitted signals experience distortions, which need to be compensated for at the receiver before we can retrieve the original signal. Hence, proper channel modelling and equalization techniques are required.

Adaptive multichannel equalization methods, such as multichannel decision feedback equalization (M-DFE) for M channels in the receiver array, have been successfully applied in literature [18]. However, these conventional methods have a large computational complexity involving large delay taps (of the order of 100). In order to avoid complex channel-estimation algorithms and equalization techniques, and save computational complexity, the concept of time reversal (TR) or phase-conjugation in the frequency domain has proven to be an attractive alternative to the conventional methods for a coherent communications system [13].

The following chapter describes the physics of time-reversal, its equivalency and implementation in digital signal processing.

Chapter 2

Background of Time-Reversal

2.1 Time-Reversal as a Concept and Literature Survey

The process of TR involves re-transmission of the received signal at a receiver array back to the source location in a time-reversed form. Due to the principle of spatial reciprocity and linear acoustical properties of the channel, this time-reversed signal is observed to concentrate temporally and spatially at the position of the originally transmitting source, and any modulation added by the receiver can be extracted. This two-way transmission method is called *Active TR or ATR* and has been experimentally proven to be successful upto mid-frequency band (3-4 kHz) [4].

TR exploits spatial diversity to gain spatial and temporal focusing of the signal. The temporal focusing (or pulse compression) mitigates ISI resulting from the multipath channel and spatial focusing allows to attain a high signal-to-noise ratio (SNR) at the intended receiver. Therefore, TR also enables multiuser communications without any explicit use of multiplexing techniques.

For ATR, let us explore its mathematics. If $s(t)$ is the original signal transmitted from the source (ps) towards an M-array transceivers, the received signal at the i^{th} transceiver, $r_i(t)$, is simply the convolution of the original signal with the channel impulse response $h_i(t)$ at the i^{th} transceiver at that time.

$$r_i(t) = s(t) * h_i(t). \tag{2.1}$$

Now, this received signal is time-reversed and re-transmitted from the M-elements. Assuming the channel is time invariant during the round trip delay, the re-transmitted signal received at the source position ps, can be written as:

$$S_{ps}(t) = \sum_{i=1}^{M} r_i(-t) * h_i(t) = s(-t) * \left[\sum_{i=1}^{M} h_i(t) * h_i(-t) \right] \approx s(-t) \tag{2.2}$$

The term in bracket, called the q-function $q(t)$, approaches a Dirac delta function in an ideal channel case. Hence, the original signal can be retrieved back in time-reversed form. We can therefore say that the two way communication performs self-equalization and is characterized by this q-function.

In practice, $q(t)$ depends on various channel parameters (the number of multipaths, number of transmitters (M) and their spatial distribution, etc.) and hence $q(t)$ is not exactly equal to the delta function. As a result, the time-reversed signal at source ps is not completely ISI free and has some residual inter-symbol interference. This residual ISI degrades the performance of TR and its effects become significant especially for high-order constellations required in high data-rate communication systems, and needs to be compensated for in the system for a reliable communication [14].

From the signal processing point of view, using Eq. 2.2, TR is simply a sum of spatio-temporal matched filering perfomed at each receiver in the SIMO system and requires only one-way transmission as shown in Fig. 2.1. This type of TR is called *Passive TR or PTR*, and has been sucessfully demonstated in [10]. The known or estimated channel impulse responses (CIRs) are required to conduct matched-filtering at the receiver elements.

It is found in [17] that the performances for the active and passive TR approaches are theoretically identical. Due to simplicity of the application of PTR, it has been extensively exploited in various studies and has been extended for its use in time-varying channels and used in conjunction with OFDM techniques for higher spectral efficiency. Since TR communications performs temporal focusing, the equivalent channel response of the SIMO system shortens and hence allows the usage of short prefixes in OFDM signals over the acoustic channels.

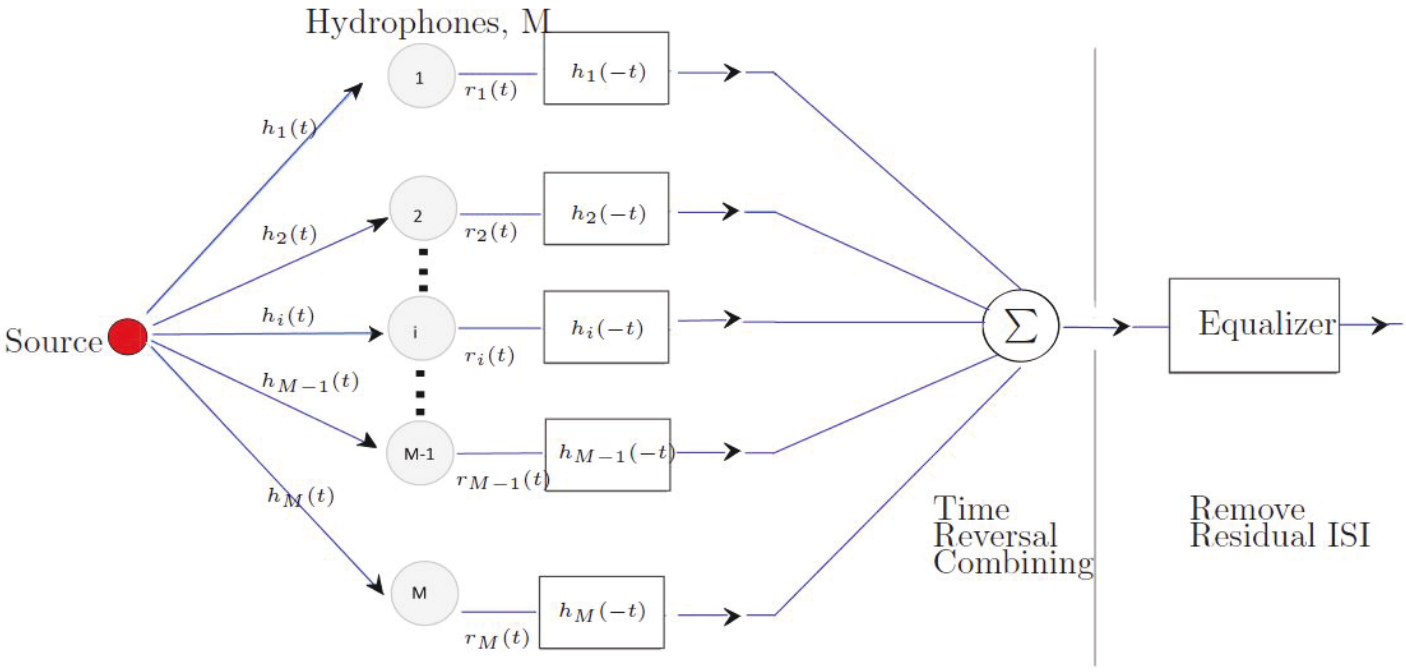

Figure 2.1: Block diagram for passive TR [13].

Advantages of Passive over Active TR

The following advantages of PTR over ATR are the reasons of our choice of using PTR for the simulation work in chapter 7.

1. Passive TR is simpler. Unlike PTR, Active TR involves a number of transducers which can both receive and transmit.

2. In active TR, extra time is needed for the re-transmission to happen, which might take up to a few seconds. In real scenarios, the channel might change during this round-trip delay of the transmission, which would violate the stationary assumption of the channel during return-transmission.

3. In time-varying channels, active TR can not be used. However, PPC (Passive Phase Conjugation) or passive TR can be designed to adapt to the time-variations of the channel.

2.2 Compensation for the Residual ISI Using Equalization

There is always some residual ISI in the signal after performing time-reversal processing. It was shown in [17] that the performance of time-reversal saturates with an increasing SNR due to the residual ISI. Moreover, the estimated/assumed CIRs required for matched-filtering in case of passive TR do not exactly match the actual CIRs and add up to extra distortion in the signal. To eliminate the effects of the remaining ISI, an adaptive single channel equalization after TR processing is often followed. A fairly common adaptive equalization technique based on decision feedback equalizer (DFE), called TR-DFE, has been well exploited in the literature and exhibits nearly optimal performance [13].

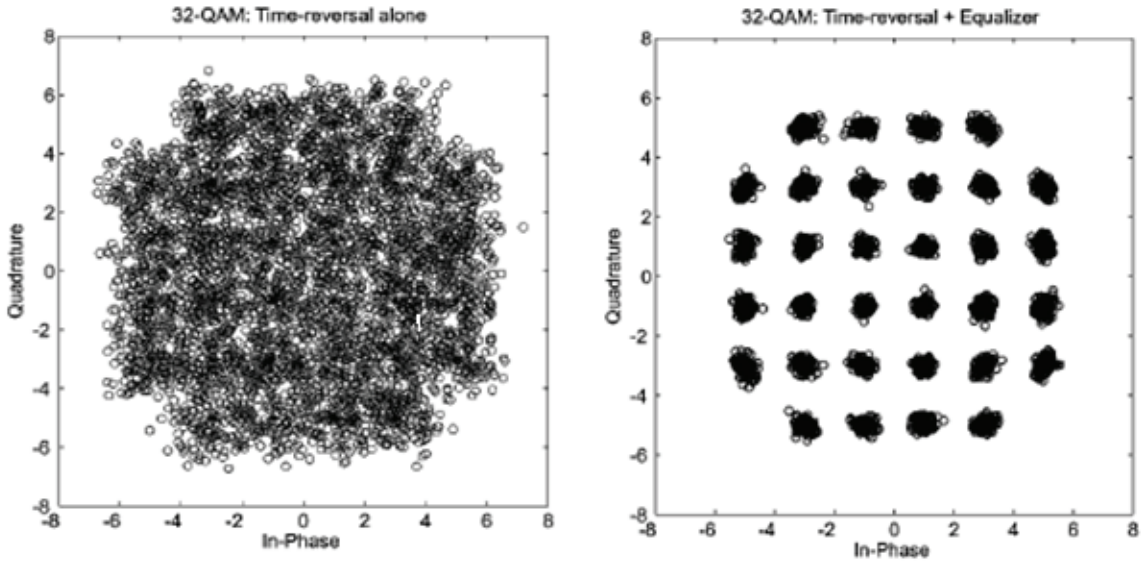

Figure 2.2: Performance of 32-QAM taken from [14] for illustration: a) with, and b) without using an adaptive equalizer.

In [14], the performance of TR-DFE was experimentally tested against that of solely active TR and showed a significant increase in post-equalization SNR due to the following single-channel equalization. In this paper, high-order constellations such as 32 QAM were used for transmission. A comparison of the performance in form of constellation diagrams for the two cases is shown in Fig. 2.2 for illustration. For this experiment, TR was applied in 50 m deep shallow water for a 2 km range with a 14-element billboard array (8.4-m long) using a carrier frequency of 3.5 kHz with a

bandwidth of 1 kHz. The symbol rate was 500 symbols/s and each communication sequence was 10 s long. Fig. 2.2 (a) shows saturation in the performance for a high constellation scheme when no equalization is applied. Whereas a significant improvement in the performance of the system with an adaptive DFE can be seen in Fig. 2.2 (b).

In another paper [15], it was shown that only 4 elements in the receive array (i.e. $M = 4$) with an appropriate spatial-diversity were sufficient to provide nearly an error-free performance using TR-DFE.

2.3 TR For Time-Varying Channels

For a SIMO system with M-receivers, a conventional adaptive multichannel-DFE (M-DFE) requires M-feedforward filters, a single feedback filter, and M phase-tracking units. The filter coefficients can either be calculated using estimates of the CIRs or tracked using algorithms like least mean square (LMS). Though adaptive M-DFEs have been enforced successfully in UWA channels, these offer high computational complexity. In contrast, TR-DFE offers reduced complexity while theoretically providing similar performance as M-DFE [13]. The advantages of using TR-DFE over M-DFE are: 1) Need of smaller number of equalizer taps due to shortened impulse response given by the q-function. 2) TR-DFE requires tracking of only an averaged single phase, which varies slower than the M independent phases in M-DFE. 3) It requires only one forward FIR filter in contrast to M forward filters.

Passive TR can be applied to time-varying channels by using the initial channel estimates from training symbols at the beginning of the data packet. For a fast varying channel, we need to frequently track the channel to avoid any mismatch in the estimated and actual CIRs so that the performance of TR is not compromised. For this purpose, either frequent probe signals can be added while compromising the data rate or channel tracking can be continuously performed using the previously detected symbols in decision-directed-mode without compromising the data rate. Another alternative is using TR-DFE on a block-by-block basis. In this method, the signal is transmitted within the duration of the coherence time, where the channel can be assumed to be time-invariant. Once the channel changes, the CIR values are updated

depending on the previously detected symbols. A succesful study on application of the TR-DFE on real data from an experiment is discussed in [16] for a slowly time-varying channel. In this paper, LMS algorithm was used to track the channel continuously.

A block-based TR-DFE was demonstrated successfully for both in both shallow and deep water. It was tested for various frequencies (50 Hz–30 kHz) with different bandwidths (from a few hertz to 20 kHz), exploiting spatial or temporal diversity or both and achieving a high spectral efficiency. For channels with high Doppler spread, no TR based approach is yet reported [13].

2.4 Definition, Characteristics, and Importance of the q-Function

In [21], it is shown that there are a few universal properties of the q-function which hold true regardless of the acoustic frequencies, source-receiver depth, delay spread and sound-speed profiles of the channel, and the signal fluctuations due to random media or source-receiver motion. The mathematical derivation in [22] deduces that the q-function is a time-dependent sinc function.

a) Sidelobes:

The sidelobes in the q-function cause inter-symbol interference and hence deteriorate the Bit-Error-Rate (BER) performance of the TR process. In order to reduce the effect of these sidelobes, spatial diversity is used [21]. The idea is to choose receivers in a VLA (Vertical Line Array) with varied spread of side-lobes so that the summation over the different array elements averages out and suppresses the sidelobes of the q-function. 15 receivers were used in [21] to sufficiently suppress the side-lobes as shown in Fig. 2.3. Spatial diversity also diminishes the phase fluctuations of the received signal, which is of concern in coherent schemes.

In [21], three different channel models (simulation and real models) with different acoustic frequencies, sound speed profiles, and source-receiver depths were compared. It was demonstrated that the BER results against the number of receiver-channels and standard deviation of the phase fluctuations of the received symbols in all the cases are of the same order of magnitude for 16 channels, q-function is dependent on these 16 channels.

For the real ocean-experiment, 16 channels of the VLA were used, covering a depth of 30 to 90 m. The VLA was deployed in water of 99.2-m depth. The source was deployed 4 m above the bottom; the bottom depth was 103 m. The source-receiver range was approximately 10 km. BPSK signals of bandwidth of 500 Hz were transmitted with a carrier frequency of 3550 Hz [21]. The channel was found to be highly coherent over the transmission length of 17 s.

b) The Main-Lobe:

The main lobe of the q-function also contributes to causing interference. The studies/experiments presented in [21] reveal that the phase fluctuations of the received BPSK symbols decrease with multiple (receiver) channels, and the variance of the imaginary part in the constellation decreases while that of real part remains almost unchanged. The overlapping of main-lobes in adjacent symbols causes constructive and destruction interference on the real axis and hence a spread on the real axis is expected. The reason for a large variance of the real part is the interference caused by the main-lobe of the q-function.

The main-lobe interference is dependent on the signal bandwidth and the data rate. To reduce the effect of this interference, either more bandwidth or a lower date rate can be used. Another option is to deploy a decision-feedback-equalizer at the receiver after the TR process.

c) Peak-to-Sidelobe Ratio:

In a q-function, the peak-to-sidelobe ratio is of great importance. This ratio helps in deciding the number of channels required to obtain acceptably low BER. Through studies in [21], it is shown that all the side-lobes of the q-function should be at least 0.1 times smaller than the main-lobe level, i.e. a peak-to-sidelobe ratio of 10 dB is required to achieve BER results of 0.5-1%. In the studied experiments, 16 channels were mostly adequate to yield an acceptable 10 dB peak-to-sidelobe ratio.

The following chapter provides a general discussion on how sound travels underwater, various factors influencing it, and the channel models used to replicate channel conditions. Its understanding becomes necessary for the purpose of reliable/suitable transmissions and further investigation in simulation models like Bellhop.

a)

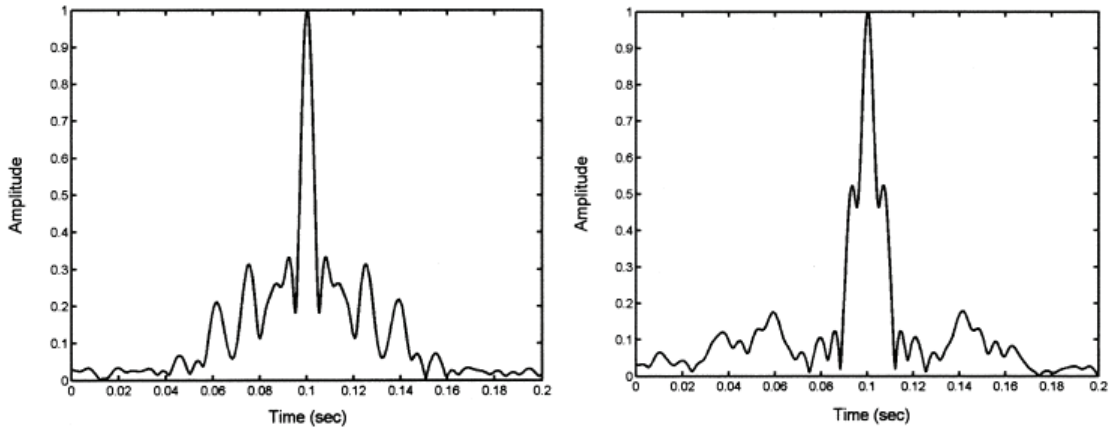

b)

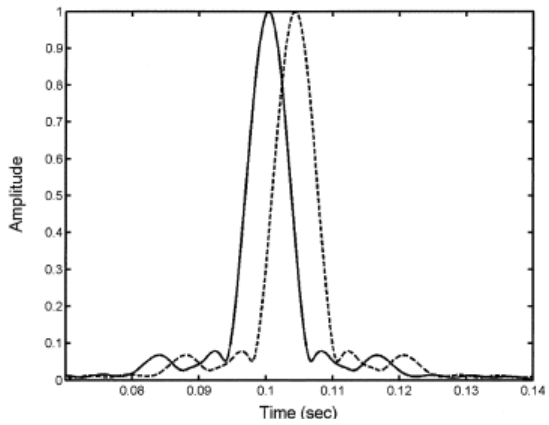

Figure 2.3: q-function taken as an illustration from [21] for a) two receivers at two different depths and b) 15 receivers altogether (solid line). The dashed line is the delayed q-function by a symbol length.

Chapter 3

Channel-Modeling for UWA Channels

3.1 Propagation of Sound in an Underwater Acoustic Channel

Sound waves are pressure changes which travel in form of alternating compressions and rarefactions of the medium in a plane parallel to the displacement of the medium, so what we have is called longitudinal waves. The acoustic wave equation describes how sound evolves in time and 3-D space, and can be utilized using the appropriate boundary and medium conditions. For an elastic medium, it is defined as

$$\nabla^2 p - \frac{1}{c^2}\frac{\partial^2 p}{\partial t^2} = 0$$

where ∇^2 is the Laplace operator, p is the acoustic pressure, and c is the speed of sound.

As sound propagates away from a sound projector, it experiences effects such as attenuation of the signal strength, spreading of the wave, reflection, and refraction from the ocean boundaries and the subsea layers.

Since any subsea body of water is physically enclosed between the top and bottom boundaries, depending on the nature and conditions these boundaries, the propagation of sound becomes complex. Not only that, but its propagation is also highly dependent on the different sound speeds that are formed in a water column which typically change with the geographical location, horizontal range, and season at the time of experiments. The two boundaries of the ocean reflect, scatter, or transmit the sound waves impinging on them depending on their angles and the nature of the surface. The top oceanic surface is mostly reflective. The effect of the bottom surface is, however, more complex due to the uncertainties associated with its material, softness/hardness, and depth of its layers.

3.1.1 Transmission Loss

As an acoustic signal radiates through an UW medium, it suffers an energy loss which is defined as the *Transmission Loss* (TL). TL, at any location away from the source, is calculated in terms of intensity of the signal at that point, I_1, with respect to that at the reference point I_0. Here, the reference point is considered to be located at a distance of one yard from the source. The expression for TL is given by [19] as

$$\text{TL [dB]} = 10 \log \frac{I_0}{I_1}. \tag{3.1}$$

3.1.2 Sources of Loss

The factors contributing to weakening of the signal energy can be categorized under two main phenomena: spreading and attenuation.

Geometric Spreading

Spreading is the effect that happens when a signal spreads out from its source. The TL due to spreading is inversely dependent on range. Theoretical models have been designed to approximate the effects of spreading underwater. These are: spherical and cylindrical spreading. In both the models, the medium is assumed to be homogeneous and having no sound-speed variations.

If sound waves do not hit any of the two boundaries of the ocean, they radiate uniformly in all directions from the projector and the spreading is called spherical. This usually happens when a source is located in the middle of the ocean far away from the surfaces. However, if the sound waves hit any of the surfaces, spreading is no more spherical and can sometimes be modeled as cylindrical. In this type of spreading, the waves are assumed to uniformly radiate over the surface of an imagined cylinder, where these surfaces are ocean boundaries. The dissipation incurred from spherical and cylindrical spreading in form of TL is inversely proportional to the square of the range (r^2) and to the linear range (r) respectively.

Attenuation

Sea-water as a propagation medium is dissipative in nature. The main phenomena which lead to attenuation of signal energy are absorption, scattering and leakage.

This loss in signal strength varies linearly with range and is expressed in dB per unit distance.

Absorption is mainly caused by refraction between two layers and the viscosity of the medium as well as chemical reactions occurring in it. For the propagation of high frequencies, the dominant factor for attenuation is viscosity, whereas it is chemical reactions that limit transmission of low frequencies. Ionic relaxation of magnesium sulfate ($MgSO_4$) and boric acid ($B(OH)_3$), two of the salts found in sea water, are found to be the most relevant factors for absorption of frequencies below 100 kHz and 1 kHz respectively [19].

Absorption of sound is a function of range, frequency, and depth. It varies inversely with range, proportionally with square of the frequency and inversely with depth.

3.1.3 Speed of Sound

The speed of sound in water changes with variations in temperature, pressure, and salinity. Sound travels faster in water than air at a speed of approximately 1500 m/s.

Colladon and Sturm were the first researchers to investigate the speed of sound underwater. Using a simple bell experiment, they approximated its speed by 1435 m/s. Typically, sound travels at 1500 meters per second in sea water at 1000 kilopascals, 3% salinity, and 10°C. A CTD (Conductivity, Temperature, Depth) device can be used to measure sound speed. Variations in the speed of sound vary strongly with the depth of the water column and are highly important in studying ray-tracing. The variation of sound speed with water depth is called the Sound Speed Profile (SSP). A typical example of a SSP is shown in Fig. 3.1.

Generally, temperature decreases and pressure increases with depth as shown in Fig. 3.2. Near the top surface, pressure is lowest, and temperature is highest and is the dominant factor of sound speed. As a result, sound speed is highest. As we go deeper, temperature decreases in the thermocline and hence also the speed of sound. With higher depths, even though the temperature continues to fall, pressure becomes dominant and sound speed starts rising again. This reality is clearly seen in Fig. 3.1. The channel corresponding to the lowest sound speed is known as SOFAR (Sound

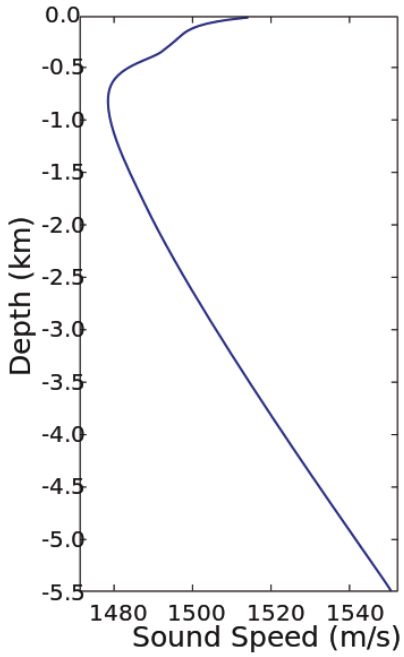

Figure 3.1: An example of the SSP in the Pacific Ocean taken from [20].

Fixing and Ranging), and is suitable for long range propagation of sound waves.

3.2 Modeling of the Propagation of Sound and Bellhop

The wave equation with the necessary boundary conditions is used to describe the propagation of sound under water. Multiple numerical and analytical models have been developed to simplify this equation and approximate acoustic trajectories. These different models are based on different theories such as ray theory, wave number integration techniques, etc. The most common and straightforward of all is based on ray theory and is more proper for high-frequency-acoustics.

Ray theory presents a simple visualization of the propagation of sound in form of rays, which travel perpendicular to the wavefronts of the acoustic signal and progress in the direction of flow of acoustic energy. The laws of reflection and refraction hold for acoustic signals as they do for optical signals. The limitation of ray acoustics is that it is a valid approximation of the wave equation only for high frequencies and does not account for the effects of diffraction. This model is mainly used for short-range acoustics. Another assumption is that the dimensions of obstacles in the medium through which sound travels are much bigger than the wavelength of the

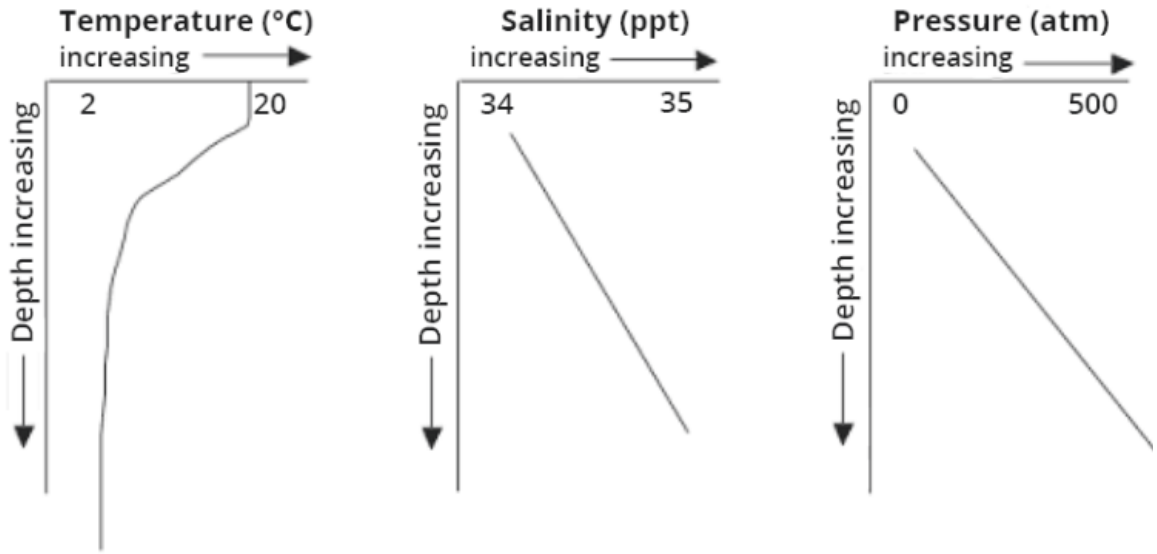

Figure 3.2: Profiles of temperature, salinity and pressure with depth [8].

acoustic signal. If this condition is not satisfied, then the effects of diffraction become dominant and can not be dealt by basic ray theory.

Rays take the form of straight lines when sound travels through a homogeneous medium, where sound-speed remains spatially constant. However, if the medium is in-homogeneous, where the speed of sound is dependent on spatial coordinates as discussed above, then the rays follow curved paths and represent effects like reflection, refraction, transmission.

Ray-tracing is a computational technique to calculate the sound ray-trajectories through a channel of varying sound speed, absorption coefficients, reflection and refraction coefficients. This is achieved by analyzing the behavior of sound rays originating from the source in small increments against the given SSP profiles and other conditions of the channel. By definition, ray-tracing is frequency-independent, which means that the ray traces are valid for all the acoustic frequencies [7]. Among others, Bellhop is a commonly used software for tracing rays. The usage and other details of this software are discussed in the next chapter [9].

Chapter 4

Bellhop

4.1 A Guide to Bellhop and its Input/Output Parameters

Bellhop is a ray tracing program based on ray-geometry and spreading laws of sound in water. It is a helpful tool that allows to visualize the ray paths, estimate the amplitude-delay arrival information reaching the receiver, calculate transmission losses in the medium, etc. The theory of Gaussian beams is used in Bellhop for calculating acoustic pressure.

There are many input parameters to Bellhop which specify conditions of the sea/ocean and the setup of the transmitter/receiver. The inputs like sound-speed-profile, depth of the ocean, geometric locations of the transceiver, range, and launching angles of beams originating from the source are fed into a file called environmental file with an extension .env. It is the basic file for a Bellhop program. There are other supporting files that can be associated with this .env file to provide more information about the system. For example, there could be a bathymetry file to specify the range dependency of the bottom of the ocean; an altimetry file to specify the ocean top; .brc and .trc files to state bottom and top reflection coefficients.

Based on these input parameters, one can generate visuals illustrating multiple effects and providing useful information on the sound propagation under the specified channel conditions. The output file with a .arr extension, called the arrival information file, describes the amplitude-delay profile of the echoes of the acoustic signal. Another file with a .ray extension illustrates the trajectories of propagation of sound. This file is capable of producing only those rays which reach the receiver while ignoring others. This particular kind of plot is an "eigenray" plot. There are other insightful output files like .shd file, which calculates the losses during transmission of the signal and plots shadow zones indicating regions where the signal is obstructed to reach.

4.1.1 Sound-Speed Profile

As explained in section 3.1.3, SSP provides information on the variations in sound-speed with depth under water. The various sound speeds with their respective depths can be fed inside an environmental file. An example of this is shown in Fig. 4.4, where various sound speeds from 0 to 50 m of the ocean depth are provided.

4.1.2 Bathymetry

A bathymetry file with an extension .bty contains particulars of the bottom of the ocean, specifying depth of water at different ranges. When there is a bathymetry file to be used as a supporting file, one adds a "*" in the bottom specification line of the. env file for Bellhop to look for it.

4.1.3 Transmitter/ Receiver Configuration

Transceiver configuration is one of the important factors in deciding ray propagation. The depths of placement of sources and receivers and the ranges between them in specified in the .env file. Depths are stated in meters while ranges in kilometers. An example of this is given in Fig. 4.4.

4.1.4 Running Simulations and Analyzing Ray Traces

Once the .env file is ready with appropriate input parameters, one can generate ray-plots for the specific channel scenario by simply running the .env file using the following command:
bellhop(title_of_the_environmental_file).

To plot ray-trajectories of sound signal from source, one can choose "R" option in the "Run Type" line of the .env file as in Fig. 4.4. Similarly, to plot an eigen-ray visualization, "E" can be used in the same line.

The rays are plotted using different colors depending on whether the ray hits one or both boundaries of the ocean [9]. The black colored rays are the rays which undergo surface and bottom reflections. Blue rays undergo only bottom reflections. Red rays encounter no reflections at all, neither from the surface nor from the bottom.

In the next section, an analysis of a real experiment which was performed in Italy is presented using Bellhop. The reason of choice of this particular experiment for analysis was to understand why time-reversal worked so well in this case.

4.2 A Channel Study from the Literature and its Analysis

Focused Acoustic Fields 2004 (FAF-04) Experiment:

In [14], active TR combined with a DFE equalizer (TR-DFE) was successfully demonstrated using a 2-D billboard array (BBA) at a 2-km range in 50-m-deep shallow water for high-order constellations such as 8-PSK, 16-QAM, 32-QAM near Elba Island, Italy. The carrier frequency used was 3.5 kHz with 1 kHz of bandwidth. The achieved data rates for the three modulation schemes were 500 symbols/s, with bit rates of 1500, 2500, and 2500 bps respectively. Each communication sequence was 10-s long. Important experimental settings and results obtained during the experiment through time reversal processing are tabulated in 4.1.

Parameter	**Value**
Range	2 km
Water Depth	50 m
Source-receive Array Type	14-element Billboard
Receiver Depth	24.5 m - 32.9 m
Source Depth	34 m
Carrier Frequency	3.5 kHz
Sampling Frequency	12 kHz
Bandwidth	1 kHz
Communication Sequence Length	10 s
Symbol Rate	500 symbols/s
Modulation Schemes Tested	8-PSK, 16-QAM, and 32-QAM
Bit Rates	1500, 2500, and 2500 bps
BER (Bit Error Rates)	about 0.027%, 1%, and 5.4%

Table 4.1: Experimental setup and achieved results using TR without equalization.

Fig. 4.1 displays the BBA receiver arrangement. Only 14 elements of the receiver array in dotted rectangle were used for the experiment.

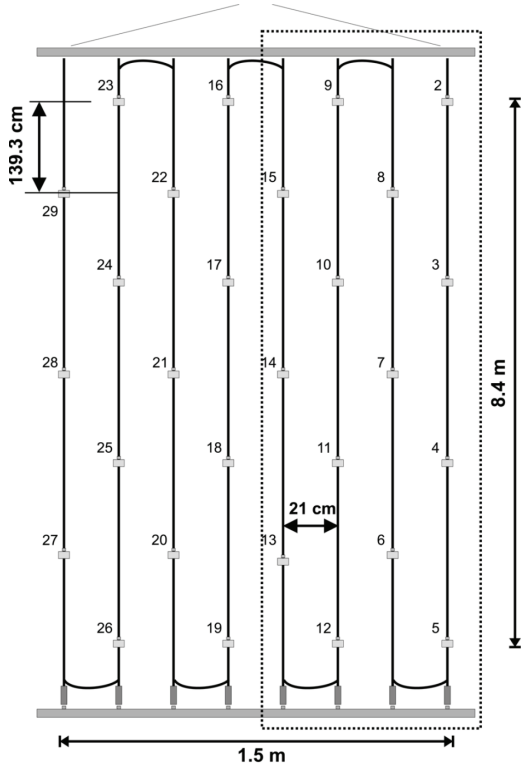

Figure 4.1: Billboard array arrangement taken from [14].

Bellhop Analysis:

We studied the FAF-04 experiment using Bellhop software to understand its remarkable achievements in terms of the high-data-rates obtained using TR processing.

A key point in understanding these results has been the given sound speed profile (SSP) for the experiment, and deployment positions of the source and receiver array. The measured SSP from the CTD experiments with the positioning of the BBA receiver are presented in Fig. 4.2 alongwith the closely developed SSP in Bellhop for our analysis.

For Bellhop simulations, only 4 elements of the 14-element BBA structure are considered at depths of 24.5 m - 32.9 m, since we are more interested in understanding the impact of reception depth-wise along the receiver array. Horizontal elements in the BBA structure of the original experiment were simply kept to provide horizontal discrimination in reverberation returns [14].

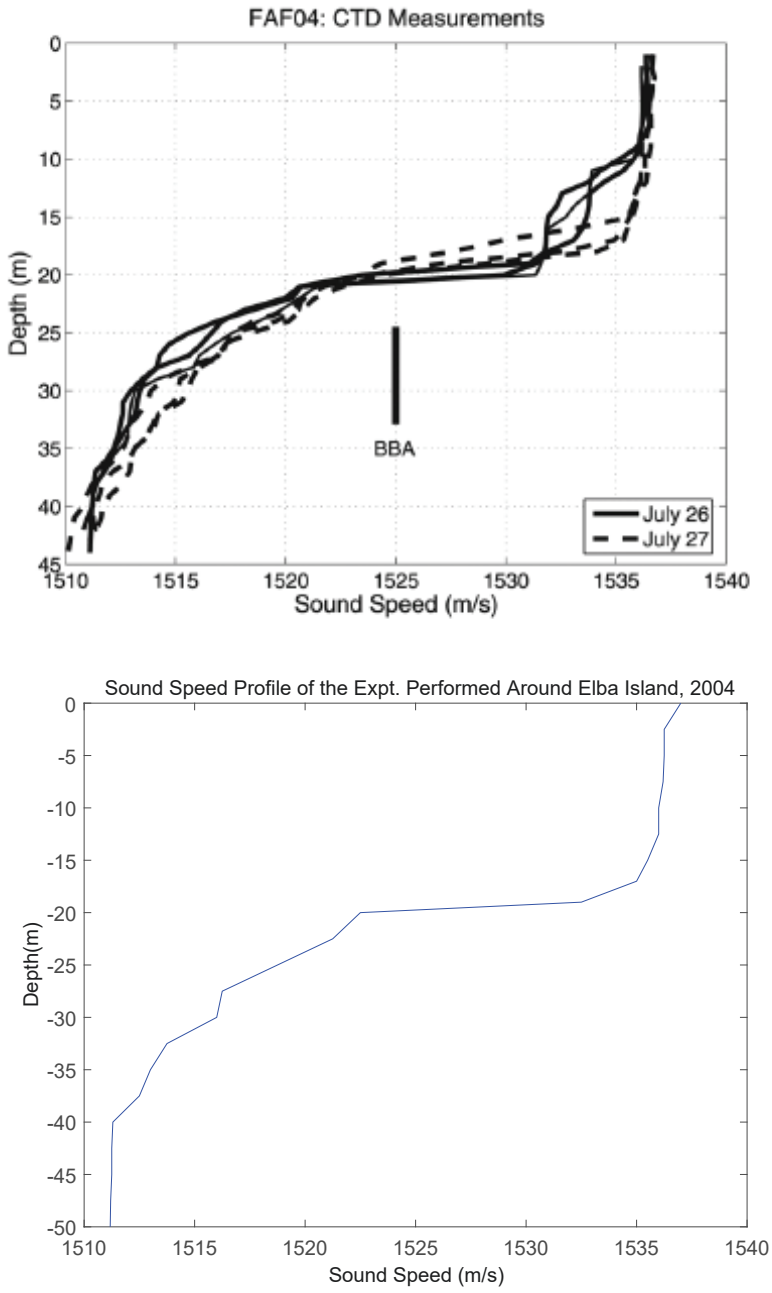

Figure 4.2: Measured SSP from the FAF04 experiment [14] (above) and generated SSP used in the Bellhop simulation (bottom).

Using Bellhop, the ray traces of sound propagation are plotted to obtain a sense of how energy is propagating in the channel for the given setup, shown in Fig. 4.3. However, not all of these rays reach the deployed receivers. To plot only those specific rays that actually reach the desired receiver elements (24.5 m - 32.9 m), eigenrays are plotted in Fig. 4.5 using the "eigenray" option in the environmental file of Bellhop. For simplicity, the number of beams used to generate raytrace and eigenray plots are 500 and 5000 respectively.

For these ray plots, launching angles of the source are varied between $-90°$ and $+90°$ from the horizontal to take into account all the possible angles of sound propagation. By convention, negative angles indicate rays launched towards the surface and positive angles towards the bottom.

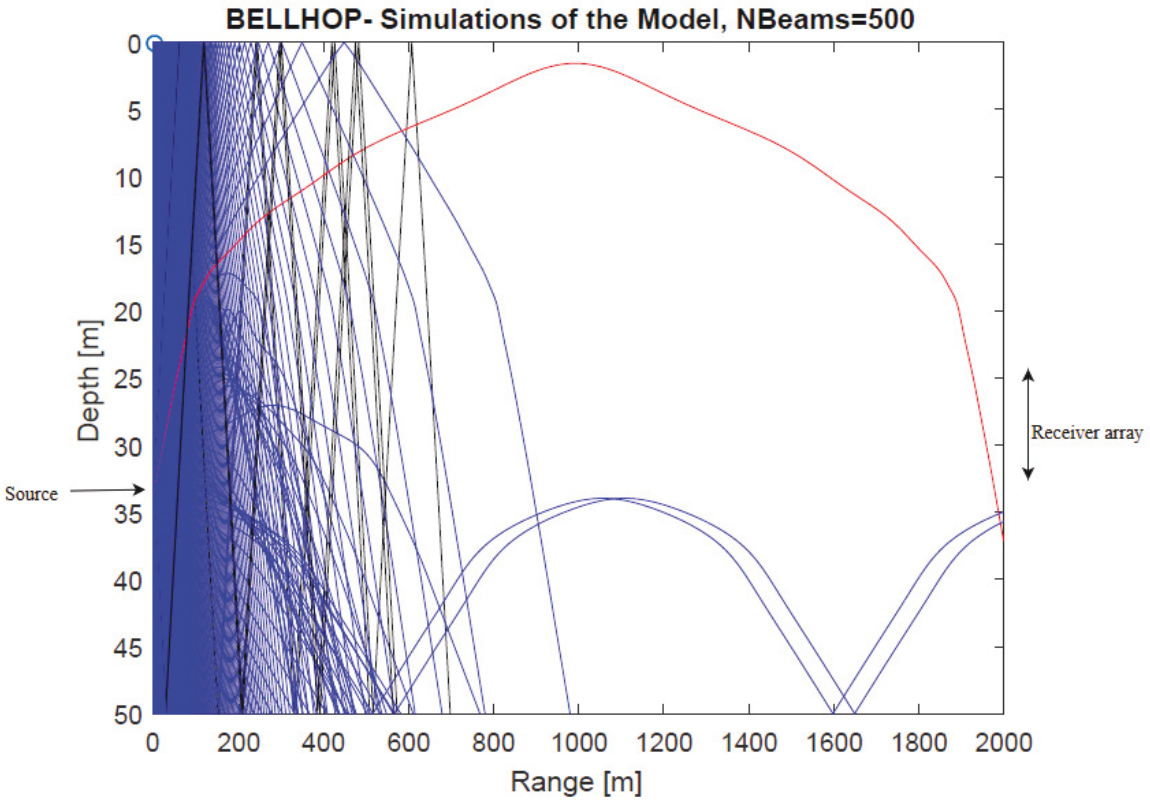

Figure 4.3: Ray traces for the SSP of Fig. 4.2 with the source at 34 m and the receivers between 24.5 m - 32.9 m.

An environmental file used to produce Bellhop plots is shown in Fig. 4.4 and Fig. 4.6 displays the generated amplitude-delay profile for the setup at all the 4 receivers under

study. Fig. 4.7 shows the simulated transmission losses (in dB) as sound propagates with depth and range.

```
'Simulations of the Model, NBeams=500'      ! Title
3500                                        ! Frequency Hz
1                                           ! Number of media
'SVF'                                       ! Sound Speed Profile OPTIONS1
23 0 50.00                                  ! Depth of the bottom
    0.0     1537       /                    ! Sound speed profile
    2.5     1536.25    /
    5.0     1536.25    /
    7.5     1536.20    /
    10.0    1536.00    /
    12.5    1536.00    /
    15.0    1535.50    /
    17.0    1535.00    /
    18.0    1533.75    /
    19.0    1532.50    /
    20.0    1522.50    /
    22.5    1521.25    /
    25.0    1518.75    /
    27.5    1516.25    /
    30.0    1516.00    /
    32.5    1513.75    /
    35.0    1513.00    /
    37.5    1512.50    /
    40.0    1511.30    /
    42.5    1511.25    /
    45.0    1511.25    /
    47.5    1511.20    /
    50.0    1511.18    /

'A' 0.0                                    ! OPTIONS2 acoustic-elastic halfspace for the bottom
 50.0  1550.0 0.0 1.5 0.5/                 ! Bottom line
1                                          ! Number of sources
34 /                                       ! Sources depth
4                                          ! Number of receiver in depth
24.5 32.9/                                 ! Receivers depth
1                                          ! Number of receivers in range
2 /                                          ! Receivers' range km
'R'                                        ! OPTIONS3 Run TypeR/C/I/S
500                                        ! Number of beams number of launching angles
-90 +90 /                                   ! The interval of lauching angles
0.0 50.00 2.00                             ! Step m, bottom depth m, transmission range km
```

Figure 4.4: Bellhop- environmental file

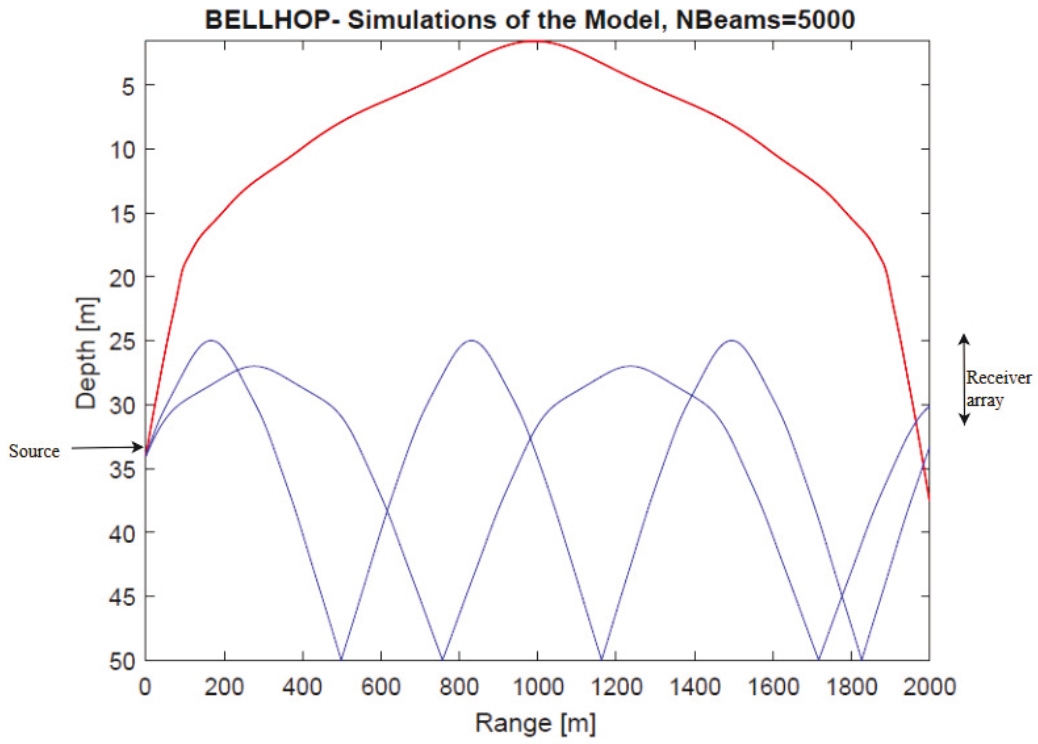

Figure 4.5: Eigenrays for the given SSP with the source at 34 m and the receivers between 24.5 m - 32.9 m.

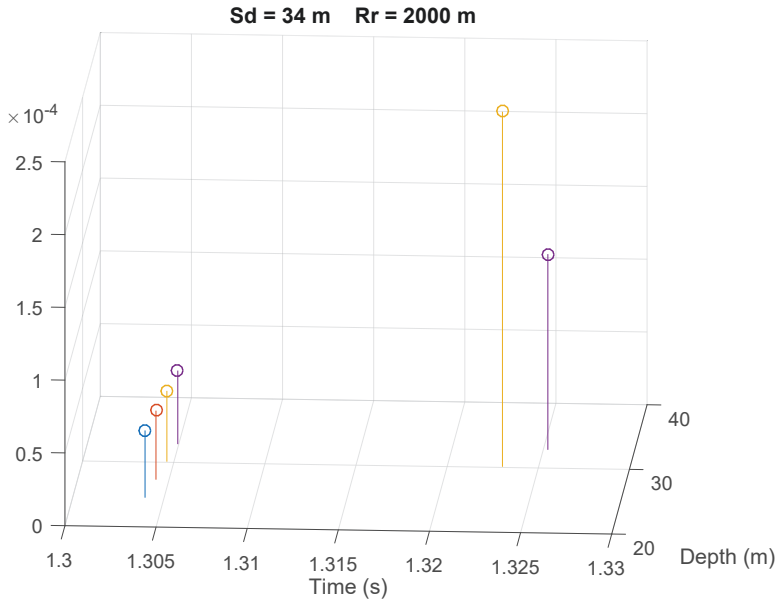

Figure 4.6: Amplitude-delay profile at the 4 receiver depths

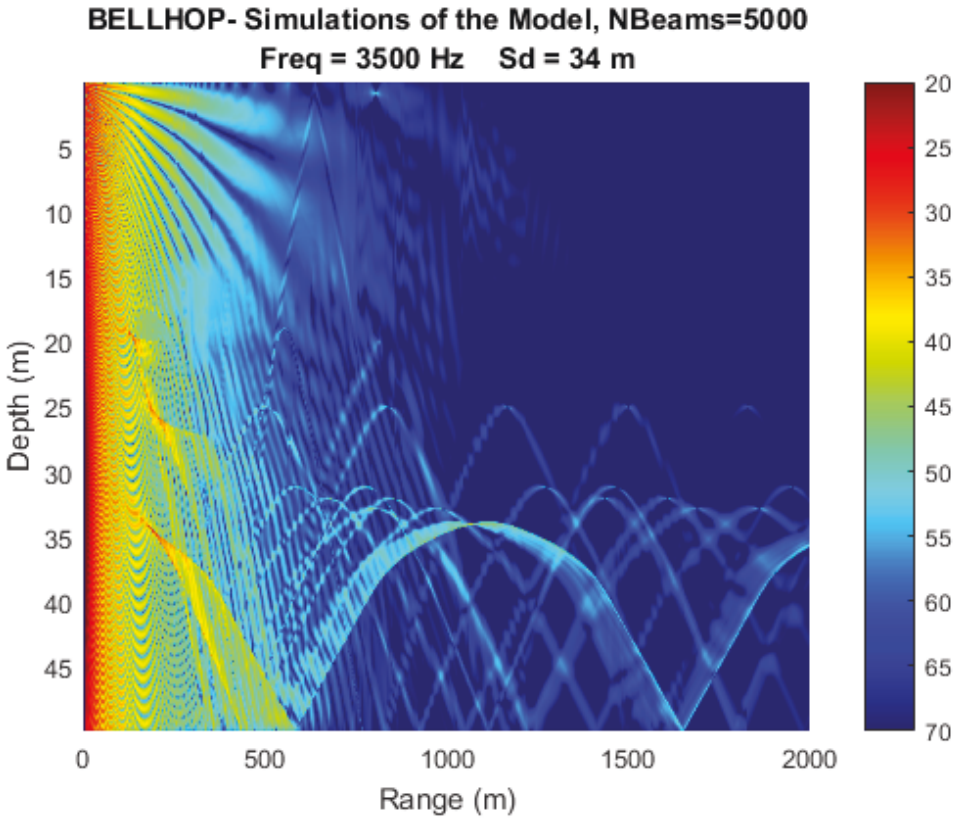

Figure 4.7: Simulated transmission loss for the given setup

Important conclusion from the Bellhop results

It is found from the eigenray plot, Fig. 4.5, that the BBA array receives rays either after bottom reflections or with no reflections from any of the boundaries. It is important to note that there are no surface reflections observed in the received rays and hence no Doppler due to surface waves is introduced. All the rays which involved surface interactions are dissipated before reaching the receiver.

This case of no Doppler (due to surface waves) is a special scenario in the UWA channels, where Doppler is not dominant because of the nature of the SSP and deployment positions of source & receiver. Hence, the channel is benign and time reversal can successfully be applied with high data rates as in [14].

Simulations for Changed Receiver Positions

To understand the reason behind the specific positions of the deployed receiver array in the original experiment, we changed the positions in Bellhop to notice differences

in the patterns of the ray traces and amplitude-delay profiles. The results for two different positions (26 m - 34.4 m and 24 m - 32.4 m) around the original placement of the array are shown in Fig. 4.8- 4.11. It can be seen that with small changes in these positions, the rays face more bottom bounces and the delayed arrivals are either very small in gain and/or hard to distinguish from each other as compared to the results in Figures 6 and 7. This is probably why the receivers were originally placed between 24.5-32.9 m during the FAF-04 experiment.

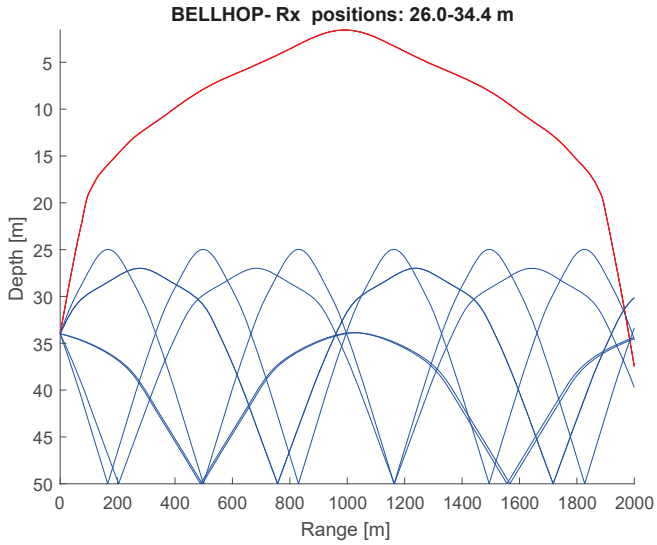

Figure 4.8: Eigenrays for changed receiver positions (26 m - 34.4 m).

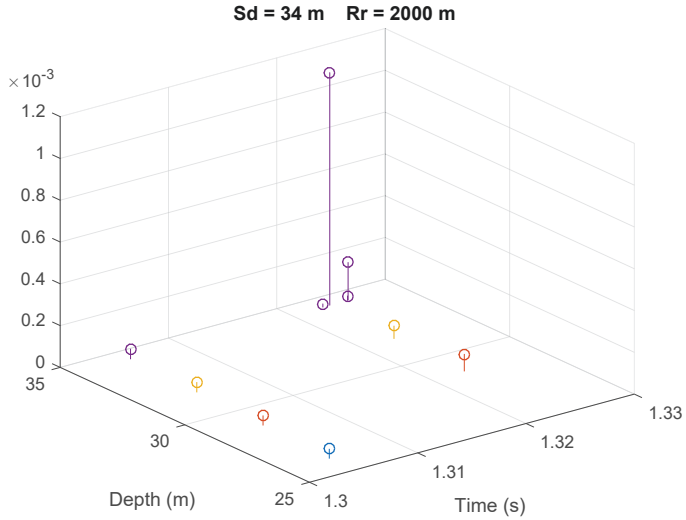

Figure 4.9: Amplitude-delay profile at the 4 receiver depths b/w 26 m - 34.4 m

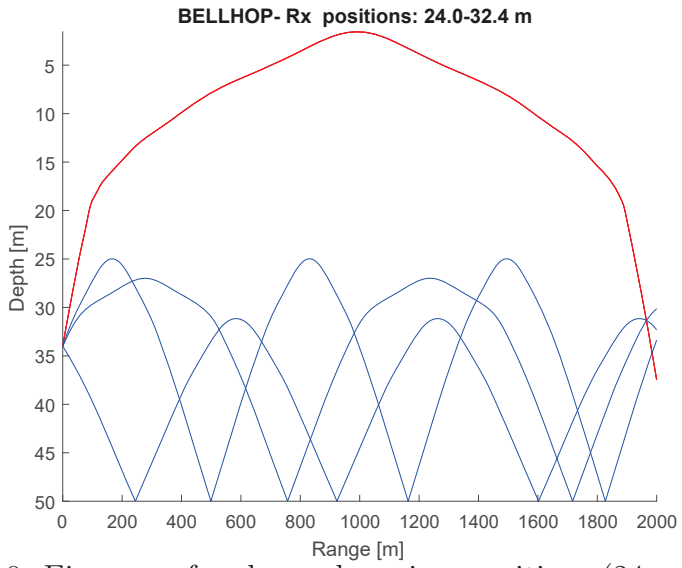

Figure 4.10: Eigenrays for changed receiver positions (24 m - 32.4 m).

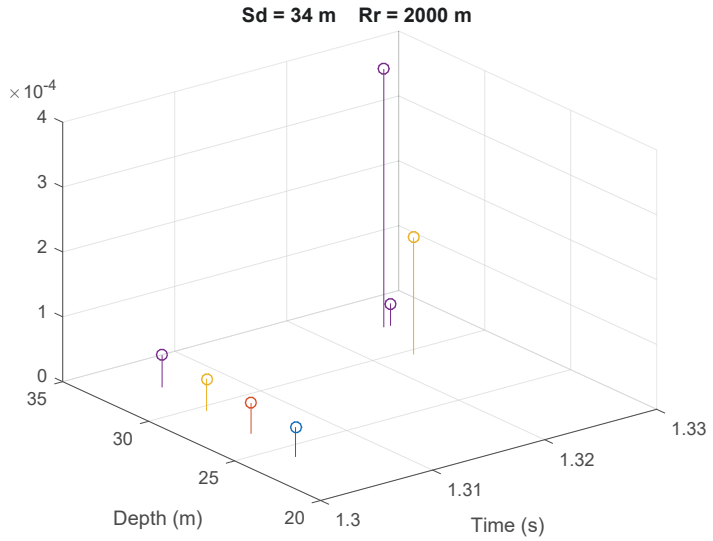

Figure 4.11: Amplitude-delay profile at the 4 receiver depths b/w 24 m - 32.4 m

Chapter 5

OFDM System

For the simulations presented in chapter 7, we have used an orthogonal frequency division multiplexing (OFDM) based Simulink model. This chapter provides a brief introduction to a typical OFDM system, its advantages and structure in time-domain.

5.1 Background

OFDM is one kind of digital modulation scheme based on frequency division multiplexing (FDM) that allows multiple orthogonal subcarriers to simultaneously carry data onto them. OFDM for acoustic channels has recently gained much interest as a multi-carrier modulation technique due to its high transmission rates as compared to single carrier modulation techniques. Among its various advantages like high spectral efficiency, robustness against ISI, fading and time-synchronization errors, a decisive advantage of OFDM is that it can be modulated and demodulated with the low-complexity Fast Fourier Transform (FFT) algorithm [6]. Another decisive advantage of its use in our models is its capability to equalize a frequency-selective channel by simple matrix multiplication in the frequency domain.

The multipath effect adds complexity by introducing frequency selective fading and Inter-Symbol Interference (ISI). One way to overcome the selective fading is to use multi-carrier modulation like OFDM. Through OFDM, a frequency selective channel can be divided into a set of flat fading channels depending on the coherence bandwidth of the channel, which greatly simplifies the equalization procedure at the receiver end. Further, adding the cyclic prefix (CP) to the OFDM frame helps in mitigating the ISI (Inter Symbol Interference) effects. A disadvantages of using OFDM in UWA channels is that the frequency offsets due to Doppler are greatly different for different sub-carrier frequencies because of the wideband nature of the acoustic communication, which in turn leads to serious ICI (Inter Carrier Interference) problem. Also, it

offers high Peak-to-Average-Power-Ratio (PAPR), but advances in linear amplifier technology have made this problem less of an obstacle. The advantages of OFDM technique clearly outweighs its disadvantages and hence the reason of our choice in modeling an UWA channels.

5.2 OFDM structure

An OFDM frame typically consists of CP and data part. CP is nothing but the tail part of an OFDM frame put in the beginning of the frame. The addition of CP serves mainly two purposes: 1) simplifying of the convolution operation by making it circular from linear 2) it adds guard interval in the frame to combat ISI.

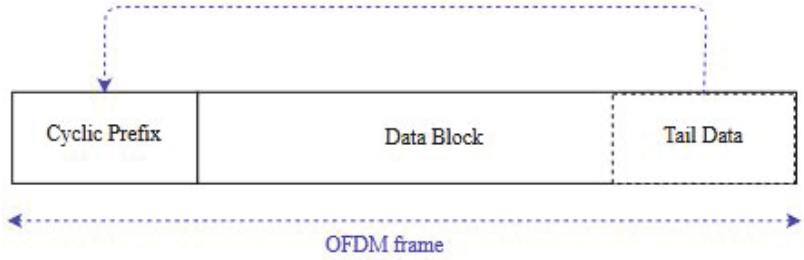

Figure 5.1: An OFDM frame structure.

5.3 Theory and Mathematics

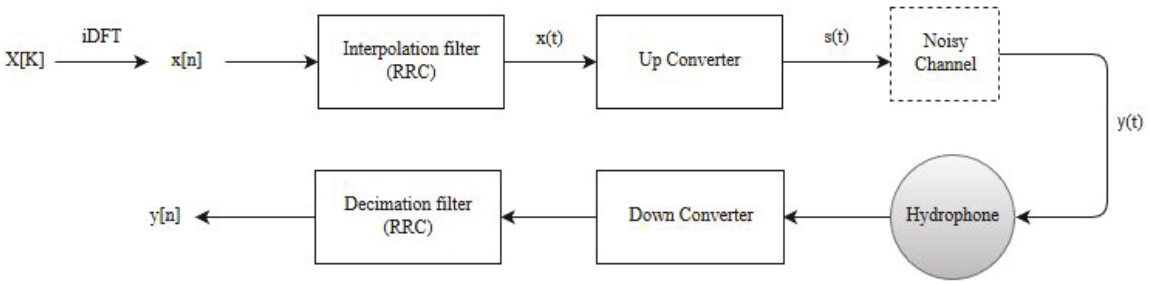

Figure 5.2: A typical communication system.

In our simulation models, data symbols are created in frequency domain from a PSK constellation, represented by $X[k]$ and then transformed to time-domain symbols

using an N-point IDFT as shown in Fig. 5.2. IDFT offers a simple way to generate an OFDM signal to which CP is added before transmission.

The time-domain complex signal in terms of $X[K]$ can be expressed as

$$x[n] = \sum_{k=0}^{N-1} X[k] e^{j2\pi kn/N} \qquad 0 \leq n \leq N-1 \tag{5.1}$$

This time signal then passes through an interpolation filter to convert the discrete-time sequence into a continuous-time signal. A strictly bandlimiting interpolation function would use the function $\mathrm{sinc}(x) = \sin(\pi x)/(\pi x)$, as known from the sampling theorem. However, the $\mathrm{sinc}(x)$ interpolation pulse can easily generate intersymbol interference and is difficult to generate with limited effort. Practically, a root-raised-cosine filter, $g(t)$ with an appropriately small roll-off factor α is used [6].

After interpolation, the baseband signal in analog form can be up-converted to a real-valued passband signal. The passband OFDM signal $s(t)$ is generated from the equivalent complex baseband signal $x(t)$ as

$$s(t) = \mathrm{Re}\{x(t) e^{j2\pi f_c t}\} \tag{5.2}$$

where f_c is a carrier frequency offset, or also the first frequency in the OFDM band. If the signal is transmitted on the passband through the channel, the received signal is down-converted first before passing through the root-raised-cosine filter at the receiver.If the Nyquist criteria for no ISI is followed, the RRC filter yields a discrete signal in time domain. These samples can be directly applied to the DFT to retrieve the data $X[k]$. For details of this communication chain, [6] can be referred.

Chapter 6

System Design and the Simulink Model

For our simulations presented in chapter 7, we have designed an OFDM based passive-time-reversal model, named OFDM-TR, in Simulink. Section 6.1 and 6.2 in this chapter describe the design models used for performing time-reversal in an OFDM system and channel estimation for these simulations with their mathematical analysis. Section 6.3 presents the complete Simulink model used for simulation purposes with explanation of its various Simulink blocks.

6.1 Background of the Design of the OFDM-TR Model

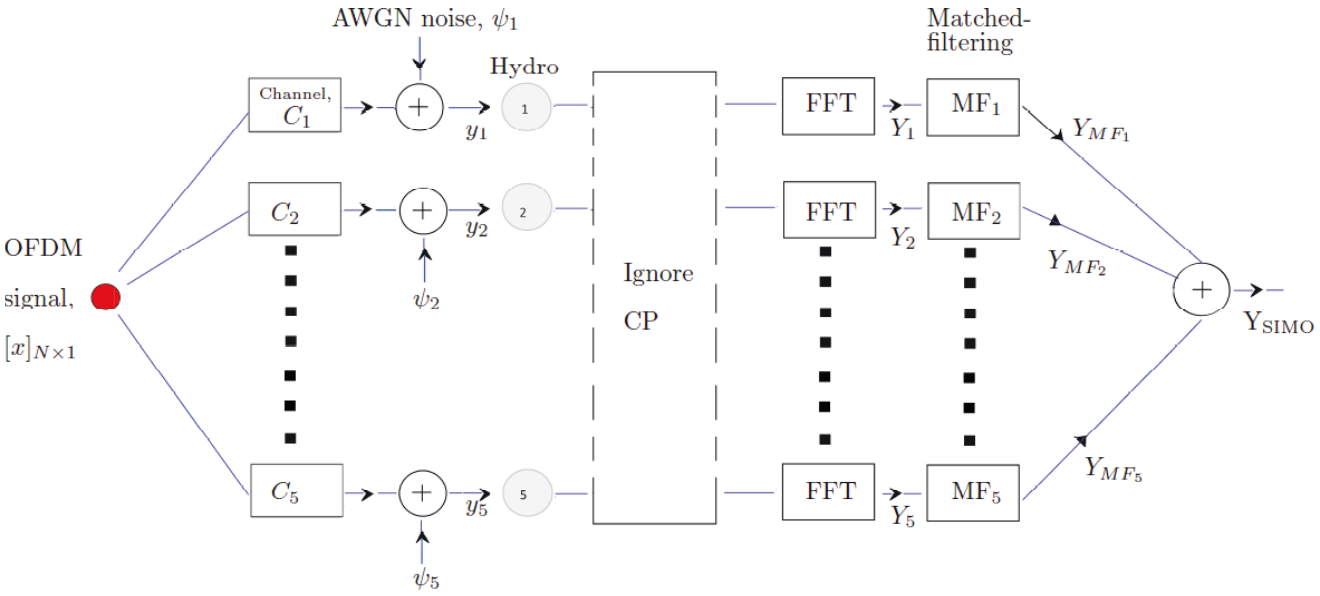

Figure 6.1: Block diagram of the TR model in Simulink.

We have developed an OFDM based time-reversal model for our simulations, which is motivated from passive-TR explained in section 2.1. For understanding the theoretical background of our OFDM-TR based single-input-multiple-output (SIMO) model, the

outlines of its design are illustrated in Fig. 6.1. A detailed block diagram of its working model is presented later in Fig. 6.8 and is discussed in section 6.3 with its implementation in Simulink. In that later section, we have also encompassed encoding/decoding, modulation/demodulation, channel estimation, and the iterative-receiver system used in our Simulink model.

For simplicity, we consider the simplified model in Fig. 6.1. Here, an OFDM data signal is transmitted through a SIMO system with 5 hydrophones and hence through 5 different channels. After removal of the CP, the received signal at any hydrophone is then matched filtered with the channel (either known or estimated) in frequency domain. These matched-filtered outputs from these 5 hydrophones are then summed to give us the final TR output named Y_{SIMO}. Let us now dive into the mathematical aspect of this model.

The received signal at any hydrophone h in discrete-time domain can be written as

$$y_h[n] = C_h * x[n] + \psi_h[n]$$

where $x[n]$, C_h and $\psi_h[n]$ represent the transmitted OFDM signal, the acoustic channel and the additive white gaussian noise (AWGN) at any hyrophone h respectively. Also, '$*$' represents convolution.

Since we transmit OFDM symbols containing CP and data parts, the channel performs a circular convolution, which in matrix form can be represented by multiplication of a circulant channel matrix with the transmitted signal. Therefore, vector representation of the received signal at h^{th} hydrophone after removing the CP part in time-domain becomes

$$y_h = \mathrm{H_h} x + \psi_h$$

where y_h, x and ψ_h are coloumn vectors of length N-by-1, and $\mathrm{H_h}$ is a circulant channel matrix of NxN with L channel taps as shown:

$$\mathbf{H_h} = \begin{bmatrix} f_1 & & & & f_L & \cdots & f_2 \\ \vdots & f_1 & & & & \ddots & \vdots \\ \vdots & \vdots & \ddots & & & & f_L \\ f_L & \vdots & \ddots & f_1 & & & \\ & f_L & \ddots & \vdots & f_1 & & \\ & & \ddots & \vdots & \vdots & \ddots & \\ & & & f_L & f_{L-1} & \cdots & f_1 \end{bmatrix}_h . \tag{6.1}$$

Equivalently, the above equation in frequency domain can be expressed as

$$Y_h = \mathrm{H}_\mathrm{h}^{(f)} X + \Psi_h$$

where the frequency-domain equivalent of the cicrulant matrix, $\mathrm{H}_\mathrm{h}^{(f)}$, is a diagonal matrix [2] as below

$$\mathbf{H_h}^{(f)} = \mathbf{F^H H_h F} = \begin{bmatrix} H[0] & & \\ & \ddots & \\ & & H[N-1] \end{bmatrix}_h . \tag{6.2}$$

and X is vector of dimensions Nx1 i.e. $[X[0], X[1],..., X[N-1]]^T$

Case 1: Matched-filtering with known channels

Assuming that the actual channels are known at the receiver and are used for matched-filtering as shown in Fig. 6.1. For any hydrophone, the output vector after matched-filtering in frequency domain is

$$\begin{aligned} Y_{MF_h} &= \mathrm{H}_\mathrm{h}^{(f)^*} \mathrm{H}_\mathrm{h}^{(f)} X + \mathrm{H}_\mathrm{h}^{(f)^*} \Psi_h \\ &= \mathrm{R}_\mathrm{h}^{(f)} X + N_{MF_h} \end{aligned} \tag{6.3}$$

where N_{MF_h} is the matched-filtered noise in frequency.

These outputs from all the 5 hydrophones are then summed to yield the MRC (Maximum Ratio Combining) result, which is

$$Y_{\text{SIMO}} = \sum_{h=1}^{5} \left(\mathrm{R}_{\mathrm{h}}^{(f)} X + N_{MF_h} \right) \tag{6.4}$$

Case 2: Matched-filtering with estimated channels

Considering that the actual channels are not known at the receiver for matched-filtering in Fig. 6.1, but only their estimates are provided using our estimator presented in section 6.2. Assume that $\hat{\mathrm{H}}_h^{(f)}$ are the channel estimates in frequency domain at any given hydrophone h. Therefore, equations 6.3 and 6.4 become

$$\begin{aligned} \hat{Y}_{MF_h} &= \hat{\mathrm{H}}_h^{(f)^*} \mathrm{H}_{\mathrm{h}}^{(f)} X + \hat{\mathrm{H}}_h^{(f)^*} \Psi_h \\ &= \hat{\mathrm{R}}_{\mathrm{h}}^{(f)} X + \hat{N}_{MF_h} \\ &\text{and} \\ \hat{Y}_{\text{SIMO}} &= \sum_{h=1}^{5} \left(\hat{\mathrm{R}}_{\mathrm{h}}^{(f)} X + \hat{N}_{MF_h} \right) \end{aligned} \tag{6.5}$$

where $\hat{Y}_{MF_h}$, $\hat{Y}_{\text{SIMO}}$, $\hat{\mathrm{R}}_{\mathrm{h}}^{(f)}$ and $\hat{N}_{MF_h}$ represent estimated equivalents of the actual vectors/matrices in equations 6.3 and 6.4.

Further, since the channel matrix in frequency is a diagonal matrix, we can say that the estimated channel matrix is also diagonal with some estimator noise, $\epsilon_{ij}^{(f)}$, added to its diagonal elements. Here, i represents the row number and j represents the coloumn number in the matrix. So, from Eq. 6.2, $\hat{\mathrm{H}}_h^{(f)}$ can be re-written as

$$\hat{\mathrm{H}}_h^{(f)} = \begin{bmatrix} H[0] + \epsilon_{11}^{(f)} & & \\ & \ddots & \\ & & H[N-1] + \epsilon_{NN}^{(f)} \end{bmatrix}_h$$

Or

$$= \mathrm{H}_{\mathrm{h}}^{(f)} + \epsilon_h^{(f)} \tag{6.6}$$

where $\epsilon_h^{(f)}$ is an NxN estimation-error-matrix for h_{th} hydrophone as follows

$$\epsilon_h^{(f)} = \begin{bmatrix} \epsilon_{11}^{(f)} & & \\ & \ddots & \\ & & \epsilon_{NN}^{(f)} \end{bmatrix}_h$$

Substituting these expressions in Eq. 6.5, we have

$$\begin{aligned} \hat{Y}_{MF_h} &= \hat{\mathrm{H}}_h^{(f)^*} \mathrm{H}_\mathrm{h}^{(f)} X + \hat{\mathrm{H}}_h^{(f)^*} \Psi_h \\ &= \left(\mathrm{H}_\mathrm{h}^{(f)*} + \epsilon_h^{(f)*}\right) \mathrm{H}_\mathrm{h}^{(f)} X \; + \; \left(\mathrm{H}_\mathrm{h}^{(f)*} + \epsilon_h^{(f)*}\right) \Psi_h \\ &= \underbrace{\mathrm{R}_\mathrm{h}^{(f)} X + N_{MF_h}}_{\text{with actual channels}} + \underbrace{\epsilon_h^{(f)*} \; \mathrm{H}_\mathrm{h}^{(f)} X + \epsilon_h^{(f)*} \; \Psi_h}_{\text{estimator noise}} \end{aligned}$$

and

$$\hat{Y}_{\mathrm{SIMO}} = \sum_{h=1}^{5} \left(\mathrm{R}_\mathrm{h}^{(f)} X + N_{MF_h} + \epsilon_h^{(f)*} \; \mathrm{H}_\mathrm{h}^{(f)} X + \epsilon_h^{(f)*} \; \Psi_h\right) \tag{6.7}$$

Estimator Noise:

Let us now quantify the noise that will be added due to the usage of our estimator.

1) **First term of the estimator noise:** Performing simple matrix multiplications, the first term in estimator-noise of Eq. 6.7 for $\hat{Y}_{MF_h}$ can be expressed in terms of an N x 1 matrix as

$$\epsilon_h^{(f)*} \; \mathrm{H}_\mathrm{h}^{(f)} X = A = \begin{bmatrix} \epsilon_{11}^{(f)*} \; H[0]X[0] \\ \vdots \\ \epsilon_{NN}^{(f)*} \; H[N-1]X[N-1] \end{bmatrix}_h$$

Considering 5 AWGN channels in Fig. 6.1, E[A] gives $[0]_{N\mathrm{x}1}$ matrix [$\because X$ is a deterministic signal, $\epsilon_{i,j}$ can be assumed to be Gaussian random variables with mean '0', and channel matrix of unit energy.]

Therefore, the variance of this matrix A becomes

$$
\begin{aligned}
\mathrm{var}(A) &= E\big[\ (A - E[A])\ (A - E[A])^H\ \big] \\
&= E[AA^H] \\
&= \begin{bmatrix} E\Big[\ \big|\ \epsilon_{11}^{(f)*}\ H[0]X[0]\ \big|^2\Big] & 0\cdots & 0 \\ \vdots & \ddots & \vdots \\ 0..... & 0 & E\Big[\ \big|\ \epsilon_{NN}^{(f)*}\ H[N-1]X[N-1]\ \big|^2\Big] \end{bmatrix}_h \\
&= \begin{bmatrix} \frac{\big|X[0]\big|^4}{N}\ E\Big[\ \big|\ \epsilon_{11}^{(f)*}\big|^2\Big] & 0\cdots & 0 \\ \vdots & \ddots & \vdots \\ 0..... & 0 & \frac{\big|X[N-1]\big|^4}{N} E\Big[\ \big|\ \epsilon_{NN}^{(f)*}\big|^2\Big]\ \ E\Big[\big|H[N-1]\ \big|^2\Big] \end{bmatrix}_h \\
&= \begin{bmatrix} \frac{\big|X[0]\big|^4}{N}\sigma^2_{\mathrm{MSE}_i} & 0\cdots & 0 \\ \vdots & \ddots & \vdots \\ 0..... & 0 & \frac{\big|X[N-1]\big|^4}{N}\sigma^2_{\mathrm{MSE}_i} \end{bmatrix}_h
\end{aligned}
\tag{6.8}
$$

where $\sigma^2_{\mathrm{MSE}_i}$ is the noise-variance due to the estimator for the i^{th} hydrophone.The resultant is a diagonal matrix of NxN.

2) **Second term of the estimator noise:** Variance of the second term in estimator-noise of Eq. 6.7 for $\hat{Y}_{MF_h}$ is

$$\mathrm{var}(\epsilon_h^{(f)*}\ \Psi_h) = \sigma^2_{\mathrm{MSE}_i}\ \sigma^2_w \tag{6.9}$$

where σ^2_w is the variance of Gaussian channel-noise.

Using equations 6.8 and 6.9, the total variance that will be added by the channel estimator in the samples of $\hat{Y}_{\mathrm{SIMO}}$ vector in Eq. 6.7 is given by

$$\text{Total variance added in } \hat{Y}_{\text{SIMO}} = \sigma^2_{\text{Total}} = \sigma^2_{\text{MSE}} \begin{bmatrix} \frac{\left|X[0]\right|^4}{N} + \sigma_w^2 \\ \vdots \\ \frac{\left|X[N-1]\right|^4}{N} + \sigma_w^2 \end{bmatrix} \tag{6.10}$$

where σ^2_{MSE} is the MSE variance added to all the 5 hydrophones due to the estimator. The formulation of MSE for our estimator presented is in section 6.2.2 of this thesis.

6.2 Channel Estimator and its Performance

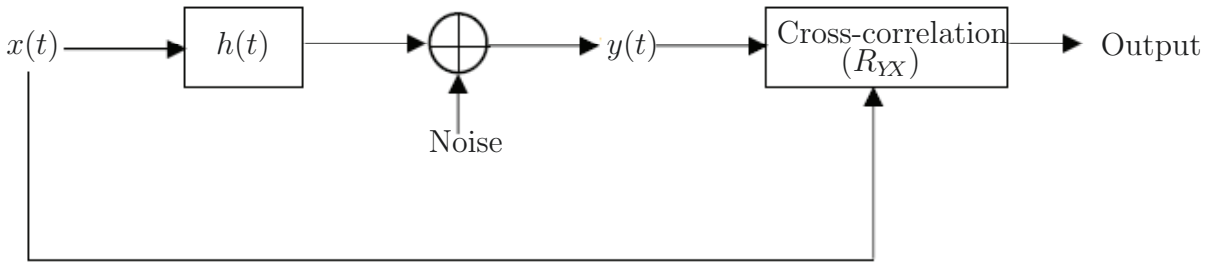

Figure 6.2: Estimating a static channel using a known sequence.

It can be shown that the channel response of a static channel can be estimated using the transmission of a reference signal with good auto-correlation properties. For example, PN sequences [3] , Walsh codes [12] and Barker codes [1] can be used for this purpose. The following mathematical formulation helps us understand how this can be achieved.

a) In the Continuous-Time Domain:

Consider a basic communication system with a time-invariant channel response, $h(t)$, as shown in Fig. 6.2. Here, $x(t)$ is the known reference sequence that is transmitted through $h(t)$ and $y(t)$ is the received signal.

Considering a noiseless environment for simplicity, $y(t)$ can be expressed simply as the convolution of the reference signal with the channel response

$$y(t) = \int_{-\infty}^{\infty} x(t-\tau)h(\tau)d(\tau). \tag{6.11}$$

The cross-correlation between the received and the original signal with lag 'ν' is given by:

$$R_{YX}(\nu) = \int_{-\infty}^{\infty} x^*(t-\nu)y(t)dt. \tag{6.12}$$

Substituting the expression for $y(t)$ from Eq. 6.11, (6.12) can be rewritten as

$$R_{YX}(\nu) = \int_{-\infty}^{\infty}\int_{-\infty}^{\infty} x^*(t-\nu)x(t-\tau)h(\tau)d\tau dt.$$

If we consider the original signal with an auto-correlation that integrates to zero everywhere except at τ=ν, the above equation simplifies to

$$R_{YX}(\nu) = \int_{-\infty}^{\infty} x^*(t-\nu)x(t-\nu)h(\nu)dt = h(\nu)E_x. \tag{6.13}$$

where $E_x = \int_{-\infty}^{\infty} x^2(t)dt$ is the energy of the reference signal $x(t)$.

This proves that the channel can be extracted using a known signal possessing ideal autocorrelation properties. However, no time-limited signal can have ideal cross-correlation, which is why we will use periodic signals below.

Subcase: Assume that $x(t)$ and $h(t)$ are two causal signals of finite duration, say $x(t)$ lies between $0 \le t \le t_1$ and $h(t)$ between $0 \le t \le t_2$; where $t_1 \ge t_2$. The above mathematical formulas can then be presented as

$$y(t) = \int_0^{t_1} x(t-\tau)h(\tau)d(\tau); \quad 0 \le t \le t_1 + t_2$$

and

$$\begin{aligned}
R_{YX}(\nu) &= \int_0^{t_1+t_2} x^*(t-\nu)y(t)dt \\
&= \int_0^{t_1+t_2}\int_0^{t_1} x^*(t-\nu)x(t-\tau)h(\tau)d(\tau)dt \\
&= \int_0^{t_1} h(\tau)\left[\int_0^{t_1+t_2} x^*(t-\nu)x(t-\tau)dt\right]d(\tau) \\
&= h(\nu)\int_0^{t_1+t_2} x^*(t-\nu)x(t-\nu)dt \\
&= h(\nu)E_x.
\end{aligned}$$

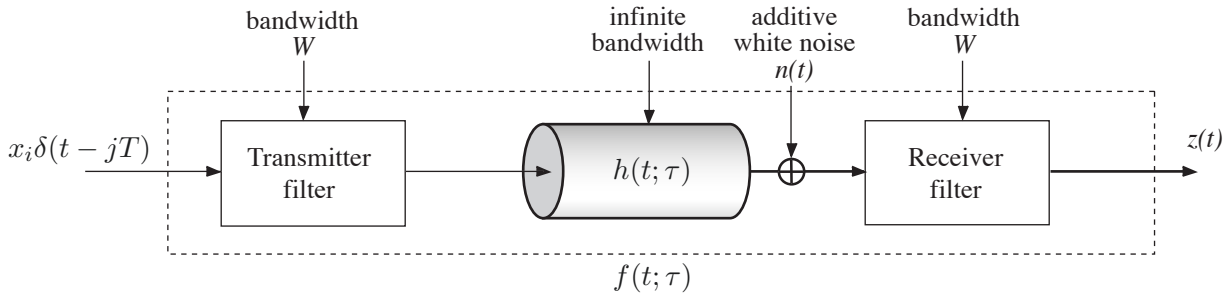

Figure 6.3: Filter model of a multipath fading channel.

b) In the Discrete-Time Domain:

Generation of Discrete Signal from a Continuous-Time Signal

Complex transmit samples x_i enter a pulse-shaping transmit filter with impulse response $g(t)$, then the channel, and are received by a matched receive filter as shown in Fig. 6.3. The output signal $z(t)$ is sampled at multiples of some sample time T_s. The overall structure is a discrete linear time-varying filter, given by [5]

$$f(t;\tau) = h(t,\tau) \star g(\tau) \star g^*(-\tau) = h(t,\tau) \star g_{\text{total}}(\tau).$$

and the sampled output signal z_k from Eq. 42 in [5] yields

$$z_k \quad = \sum_{l=1}^{L} x_{k-l} f_l(kT_s) + n_k.$$

Channel Model

A WSSUS (A Wide-Sense Stationary Uncorrelated Scattering) channel can be generated using the *sum-of-sinusoids* (SOS) model using Eq. 29 from [6], which creates the samples $h[n] = h(nT_s)$ according to

$$h[n]_{\text{Rayleigh}} = \frac{1}{\sqrt{L}} \sum_{m=1}^{L} e^{j(\phi_m + 2\pi f_m n T_s)} \tag{6.14}$$

where T_s is the sample time interval used to represent the continuous time variable t, L is the number of multipaths to model the channel tap n, ϕ_m are random phases uniformly distributed in the interval $[0, 2\pi]$ and f_m are the L Doppler frequencies

contributing to $h[n]$. If $L \to \infty$ it can be shown that the amplitude in Eq. 6.14 is Rayleigh distributed. If the amplitude is to be Ricean distributed, the channel samples can be generated by adding a bias term

$$h[n]_{\text{Rice}} = \frac{1}{\sqrt{L(1+K_R)}}\left[\sum_{m=1}^{L} e^{j(\phi_m + 2\pi f_m n T_s)} + \sqrt{K_R}\, e^{j(\phi_0 + 2\pi f_0 n T_s)}\right]$$

where K_R is the Rice factor given by the ratio of the power of the specular component to that of the diffused components in each channel tap and f_0 is the Doppler frequency of the specular component in each channel tap.

Channel Estimation for a Discrete-Time Signal

In the discrete domain, consider $x[n]$ and $h[n]$ as two causal signals of length N and M respectively. Equations 6.11 and 6.12 can be expressed as

$$y[n] = \sum_{k=0}^{\max(M,N)-1} x[n-k]h[k]; \quad 0 \le n \le M+N-2 \tag{6.15}$$

and

$$\begin{aligned} R_{YX}[l] &= \sum_{n=0}^{\max(M+N-1,M)-1} x^*[n-l]y[n] \\ &= \sum_{n=0}^{\max(M+N-1,M)-1} \sum_{k=0}^{\max(M,N)-1} x^*[n-l]x[n-k]h[k]. \end{aligned}$$

Using the ideal auto-correlation properties of the reference signal, the above equation is reduced to

$$R_{YX}[l] = h[l] \sum_{n=0}^{\max(M+N-1,M)-1} x^*[n-l]x[n-l] = h[l]E_x. \tag{6.16}$$

Hence, the information of the channel impulse response is extracted.

c) Noisy System in the Discrete-Time Domain:

Consider a discrete system model affected by Additive White Gaussian Noise (AWGN), as shown in Fig. 6.2. Let us suppose that $w[n]$ represents the n^{th} white Gaussian noise sample. Therefore, (6.15) can be re-written as

$$y[n] = \sum_{k=0}^{\max(M,N)-1} x[n-k]h[k] + w[n]; \; 0 \le n \le M+N-2$$

and

$$R_{YX}[l] = \sum_{n=0}^{\max(M+N-1,M)-1} x^*[n-l]y[n]. \tag{6.17}$$

Substituting the expression for $y[n]$ we get

$$\begin{aligned} R_{YX}[l] &= \sum_{n=0}^{\max(M+N-1,M)-1} \sum_{k=0}^{\max(M,N)-1} x^*[n-l] \Big(x[n-k]h[k] + w[n] \Big) \\ &= \sum_{k=0}^{\max(M,N)-1} h[k] \Bigg[\sum_{n=0}^{\max(M+N-1,M)-1} x^*[n-l]x[n-k] \Bigg] + \sum_{n=0}^{\max(M+N-1,M)-1} x^*[n-l]w[n]. \end{aligned}$$

In other words,

$$R_{YX}[l] = h[l]E_x + \sum_{n=0}^{\max(M+N-1,M)-1} x^*[n-l]w[n]. \tag{6.18}$$

The first term above is the noiseless channel and the second term is the noisy component of the cross-correlation.

Since $w[n]$ is a discrete stochastic Gaussian process, the cross-correlation function of $w[n]$ (a random process) and $x[n]$ (a deterministic process) is also a random Gaussian process. To characterize this Gaussian process, the first two moments are sufficient.

Define:

$$z[l] = \sum_{n=0}^{P} x^*[n-l]w[n]; \quad \text{where } P = \max(M+N-1, M) - 1.$$

Since $w[n]$ and $x[n]$ are independent of each other, and the mean of the white noise

is zero at any point in time, the first moment of the above cross-correlation vanishes:

$$\begin{aligned} E\big[z[l]\big] = \mu_Z[l] &= E\bigg[\sum_{n=0}^{P} x^*[n-l]w[n]\bigg] \\ &= \sum_{n=0}^{P} E\Big[x^*[n-l]w[n]\Big] \\ &= \sum_{n=0}^{P} E\big[x^*[n-l]\big]E\big[w[n]\big] \\ &= 0;\ \forall l \end{aligned}$$

Similarly, the second moment of $z[l]$ can be calculated as

$$\begin{aligned} E\big[z^2[l]\big] &= E\Big[z[l]z^*[l]\Big] \\ &= E\bigg[\Big(\sum_{n=0}^{P} x^*[n-l]w[n]\Big)\Big(\sum_{n'=0}^{P} x[n'-l]w^*[n']\Big)\bigg] \\ &= \sum_{n=0}^{P}\sum_{n'=0}^{P} E\Big[x^*[n-l]x[n'-l]\Big]E\Big[w[n]w^*[n']\Big]. \end{aligned}$$

For all $n \neq n'$, the above equation reduces to 0. This is because the ensemble auto-correlation of the WSS noise process is zero for all lags except $'0'$.

Therefore,

$$\begin{aligned} E\big[z^2[l]\big] &= \sum_{n=0}^{P} \big|x[n-l]\big|^2 E\Big[\big|w[n]\big|^2\Big] \\ &= \sigma_w^2 \sum_{n=0}^{P} \big|x[n-l]\big|^2 \\ &= \sigma_w^2 E_x;\ \text{where } \sigma_w^2 \text{ is the variance of the white noise process.} \end{aligned} \tag{6.19}$$

Since $E[z(l)] = 0$, this is also the variance of $z[l]$. Therefore, we can say that the random noise fluctuations in $z[l]$ have mean $'0'$ and variance $\sigma_w^2 E_x$.

The autocovariance of $z[l]$ can be found as follows:

$$\begin{aligned}
C_{ZZ}[l,l'] &= E\big[\big(z[l]-\mu_Z[l]\big)\big(z[l']-\mu_Z[l']\big)^*\big] \\
&= E\big[z[l]z^*[l']\big];\ \text{using result from mean of z[l]} \\
&= E\Big[\Big(\sum_{n=0}^{P} x^*[n-l]w[n]\Big)\Big(\sum_{n'=0}^{P} x^*[n'-l']w[n']\Big)^*\Big] \\
&= \sum_{n=0}^{P}\sum_{n'=0}^{P} E\Big[x^*[n-l]x[n'-l']w[n]w^*[n']\Big] \\
&= \sum_{n=0}^{P}\sum_{n'=0}^{P} E\big[x^*[n-l]x[n'-l']\big]E\big[w[n]w^*[n']\big]
\end{aligned}$$

$$= \begin{cases} \sigma_w^2 \sum_{n=0}^{P} x^*[n-l]x[n-l']; & \text{if } n=n' \\ 0; & \text{otherwise} \end{cases}$$

$$= \begin{cases} \sigma_w^2 E_x; & \text{if } n=n\text{' and } l=l' \\ 0; & \text{otherwise} \end{cases}$$

The above results hold only if the autocorrelation function of $x[n]$ is ideal, i.e.,

$$\sum_{n=0}^{N-1} x[n]x^*[n+\nu] = \begin{cases} E_x, & \text{if } \nu=0 \\ 0, & \text{if } \nu\neq 0 \end{cases}$$

6.2.1 Possibilities of a Reference Signal

1) **PN Sequences**: A maximum-length sequence (M-sequences), which is a type of pseudo-random binary sequence (PN sequence), can be used as a reference signal. If a PN sequence is long enough, it provides the desired auto-correlation characteristics. The periodic auto-correlation of such a sequences is almost uncorrelated at all lags except at lag '0'.

   Example:

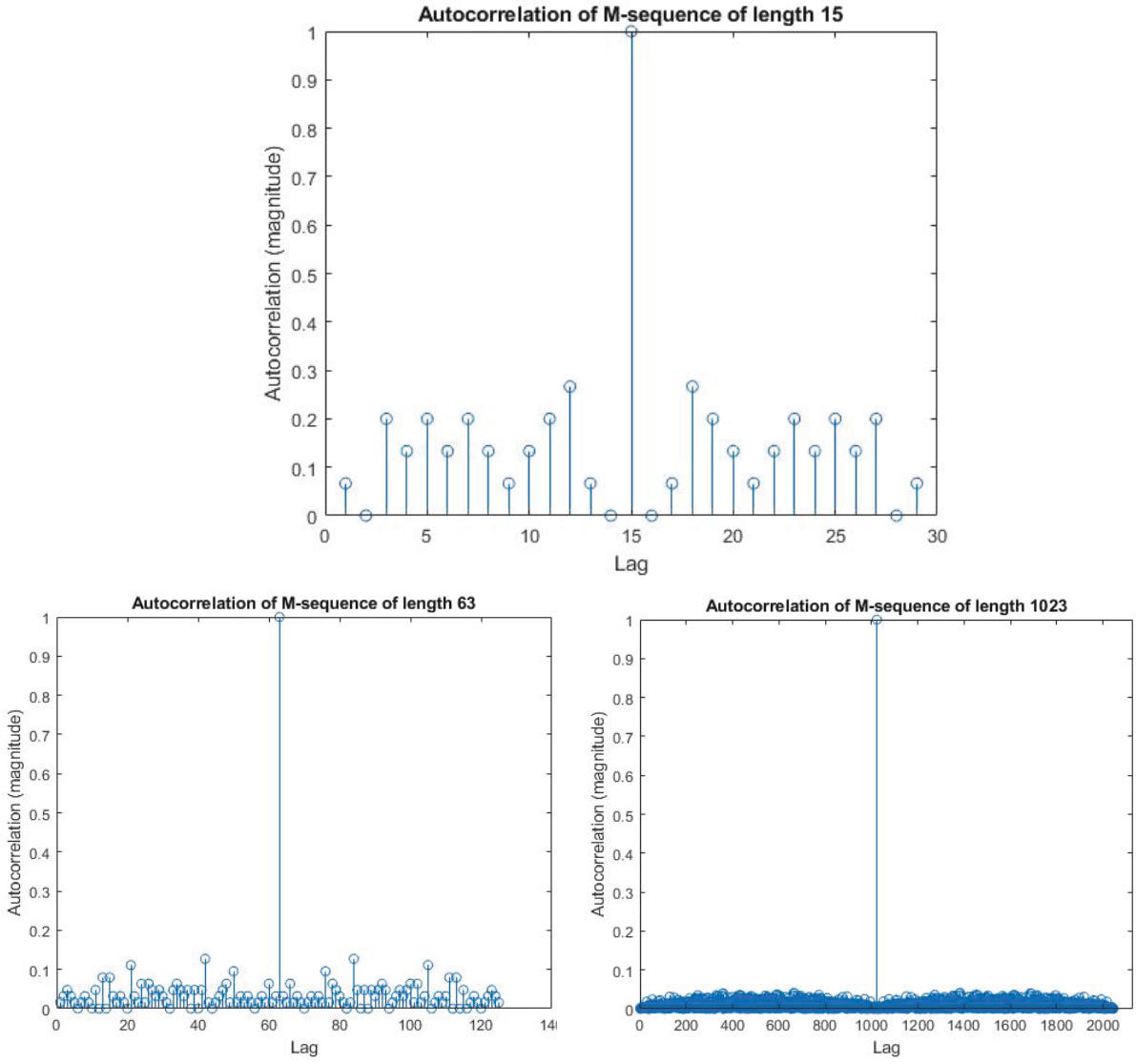

Figure 6.4: Auto-correlation function of M-sequences of lengths 15, 63 and 1023 showing better auto-correlation properties for higher lengths.

If $x[n]$ is an M-sequence of length N, its circular auto-correlation is given by

$$R_{XX}[n] = \frac{1}{N}\sum_{m=1}^{N} x[m]x^*[m+n]_N = \begin{cases} 1, & \text{if } n = 0, \\ -\frac{1}{N}, & \text{if } 0 < n < N \end{cases}$$

where$[m+n]_N$ represents circular shift in signal by n units.

2) **Barker Codes**: A Barker sequence is such a finite collection of +1 and -1 symbols such that the off-peak coefficients of its auto-correlation function are as small as possible.

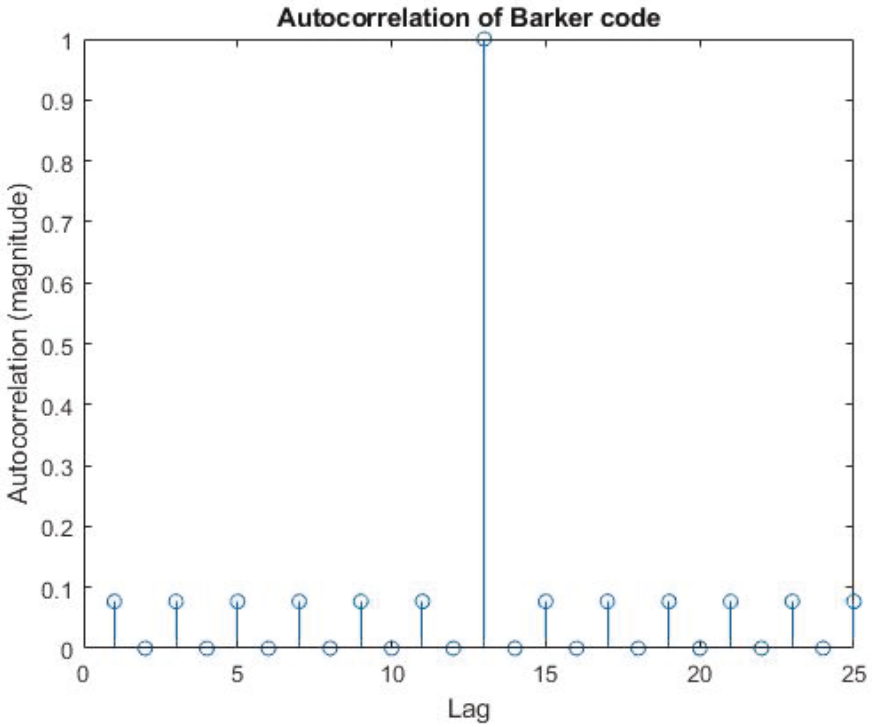

Figure 6.5: Auto-correlation function of Barker code sequence of length 13.

3) **Shift-Orthogonal Sequences**: A shift-orthogonal sequence can also be used as reference signal, where the sequence is orthogonal to each shift of itself.

A shift-orthogonal sequence can be defined in the frequency domain by a sequence $B_M[k] = \left[B_M[0], B_M[1], B_M[2], ...B_M[M-1]\right]$ of M frequency values, which are transformed into the time domain via

$$b_M[n] = \frac{1}{M}\sum_{k=0}^{M-1} B_M[k]e^{2\pi jkn/M}$$

and where $|B_M[k]| = 1$. We consider pilot sequences $b[n]$ with periodicity N_p

$$b[n] = \begin{cases} b_M[n \bmod M], & \text{if } 0 \leq n \leq N-1 \\ 0; & \text{if } n \geq N \end{cases}$$

where $N = N_p M$.

For a shift-orthogonal sequence, $b_M[n]$, the following condition holds

$$\sum_{i=0}^{M-1} b_M[i] b_M[i+s]_M = 0 \ \forall s \neq 0$$

where s represents an arbitrary shift.

This implies that the auto-correlation function of a shift-orthogonal sequence is ideal. For example, B_M symbols of length 64 are generated from a QPSK constellation in the frequency domain, whose transformation in to the time-domain is shown in Fig. 6.6. It can be observed that all the samples in this sequence are of unity amplitude and that the time-domain signal is shift-orthogonal as in Fig. 6.7.

Note: The peak-to-off-peak ratio in the auto-correlation function of the above three sequences are of great importance while choosing one over the another. For a length $63 - 64$, shift-orthogonal sequences exhibit the closest resemblance to the ideal delta Dirac function.

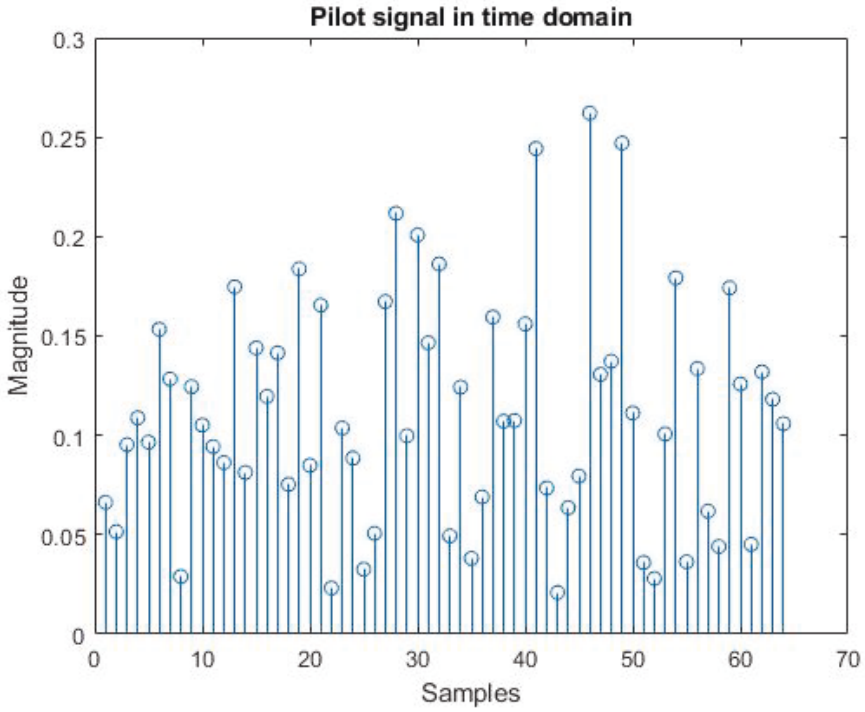

Figure 6.6: Shift-orthogonal sequence in the time domain for the frequency sequence $b^{(f)}$.

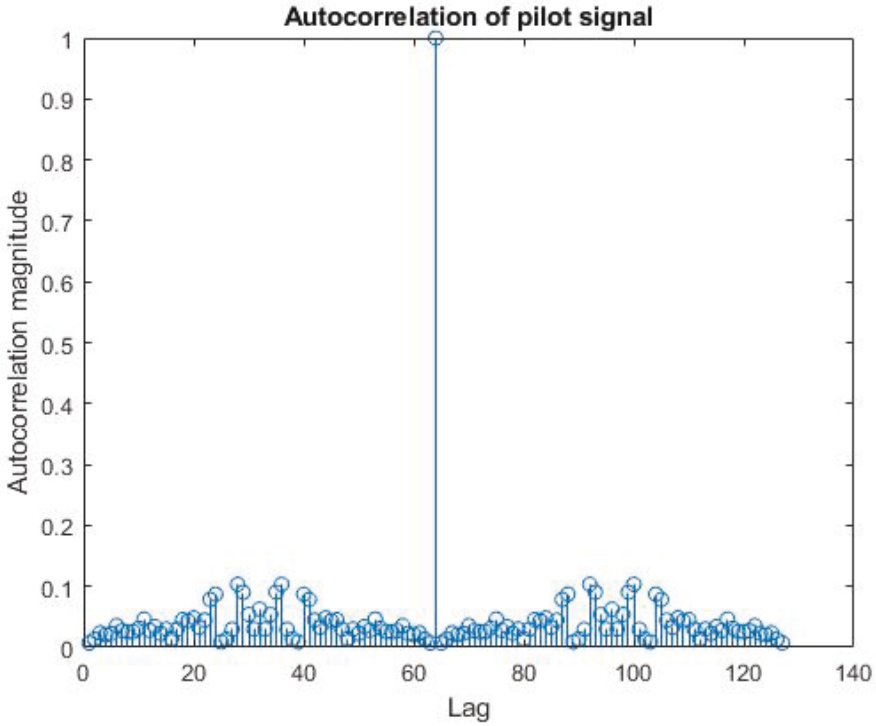

Figure 6.7: Auto-correlation function of the shift-orthogonal sequence of length 64.

6.2.2 Derivation of MSE Calculations for the Estimator in Simulink

[1] Let $B_M[k]$ denote the M FD-pilots given by

$$B_M[k] = a_m[k] \tag{6.20}$$

where the a_m are complex random coefficients with unit magnitude. The IFFT gives the TD pilots as

$$b_M[n] = \frac{1}{M} \sum_{m=0}^{M-1} a_m e^{j2\pi mn/M}. \tag{6.21}$$

We note that the *periodic* autocorrelation of $b_M[n]$ is just

$$R[l] = \delta[l]. \tag{6.22}$$

i.e., it is just a delta impulse of amplitude 1. Repeating $b_M[n]$ with a repetition rate of N_p, where N_p is the number of pre-ambles, yields the N-point TD pilots

$$b[n] = \frac{1}{M} \sum_{m=0}^{M-1} a_m e^{j2\pi mn/M} \tag{6.23}$$

where $N = N_p M$. The circular periodic cross-correlation of $b_M[n]$ with $b[n]$ is given by

$$(b_M[n] \star b[n])(l) = \sum_{r=0}^{N_p-1} \delta[n - (r+1)M]. \tag{6.24}$$

For estimating the channel, we use the cross-correlation of the received pilot signal with $b_M[n]$ as described in section 6.2. The performance of an estimator is quantified by its MSE.

Let the multipath channel be given by $h[n]$ and assume that the channel is stationary (i.e. there is no Doppler shift or spread). Assuming AWGN is added at the receiver, the received lowpass discrete-time signal $y[n]$ is given by

$$y[n] = h[n] * b[n] + w[n] \tag{6.25}$$

where $0 \leq n \leq N_h + N_p M - 1$. Assuming that $N_h \leq M$, and using a CP with length M changes the domain to $0 \leq n \leq M + N_p M - 1$.

[1] This derivation is a joint work done with my colleague Ali Bassam.

The estimator first cross-correlates $y[n]$ with a copy of $b_M[n]$, or alternatively convolves $y[n]$ with $b_M^*[-n]$. The output of such a convolution is given by

$$y[n] * b_M^*[-n] = h[n] * b[n] * b_M^*[-n] + w[n] * b_M^*[-n]. \tag{6.26}$$

where $0 \leq n \leq 2(M + N_p M) - 1$.

Using (6.24) we find that

$$y[n] * b_M^*[-n] = \sum_{r=0}^{N_p-1} h[n - rM] + w[n] * b_M^*[-n]. \tag{6.27}$$

Let $\hat{h}_r[n] = \hat{y}[n]|_{rM \leq n \leq 2rM-1}$ and $z_r[n] = w[n] * b_M[-n]|_{rM \leq n \leq 2rM-1}$. We then have

$$\hat{h}_r[n] = h[n - rM] + w_r[n]. \tag{6.28}$$

but since $N_h \leq M$, we have $h[n - rM] = h[n]$ and so

$$\hat{h}_r[n] = h[n] + w_r[n]. \tag{6.29}$$

which is a sample channel estimate from one of the preambles.

Finally the estimator averages over the N_p pre-ambles to yield the final sample estimate

$$\hat{h}[n] = \frac{1}{N_p} \sum_{r=0}^{N_p-1} \hat{h}_r[n] = h[n] + \frac{1}{N_p} \sum_{r=0}^{N_p-1} w_r[n]. \tag{6.30}$$

Taking the variance of the above expression yields

$$E[|\hat{h} - h|^2] = \frac{1}{N_p^2} E\left[\left|\sum_{r=0}^{N_p-1} w_r[n]\right|^2\right] \tag{6.31}$$

where $w_r[n]$ is also an i.i.d. Gaussian RV with mean 0 and variance to be determined. Since

$$E\left[\left|\sum_{r=0}^{N_p-1} w_r[n]\right|^2\right] = \sum_{r=0}^{N_p-1} E[|w_r[n]|^2] = N_p \sigma_w^2, \tag{6.32}$$

(6.21) becomes

$$E[|\hat{h} - h|^2] = \frac{1}{N_p^2} \sum_{r=0}^{N_p-1} E[|w_r[n]|^2] = \frac{\sigma_w^2}{N_p}. \tag{6.33}$$

Since we have N_h channel samples, we conclude that the MSE of our estimator is given by

$$\sigma_{\text{MSE}}^2 = E[|\hat{\mathbf{h}} - \mathbf{h}|^2] = \frac{N_h}{N_p} \sigma_w^2. \tag{6.34}$$

This implies that the MSE reduces with increase in number of preambles used for averaging of the channel estimates and has been verified experimentally as well.

6.3 Simulink Model and Explanation of its Various Blocks

The OFDM-TR model is an extension of the Simulink model presented in [6] and is heavily borrowed from [6]. A block diagram of our OFDM-TR model [2] is shown in Fig. 6.8. Note that this block diagram presents only the SISO view of the model and can be extended to SIMO system containing 5 hydrophones to produce the exact model as in our Simulink model. For detailed view of the complete Simulink model, please refer to Complete_model_estimator_with_TR_simulink.slx in packages with Ultra-maritime-digital-communications-centre (UMDCC). Various parts of this Simulink model are discussed separately to some detail in the following subsections.

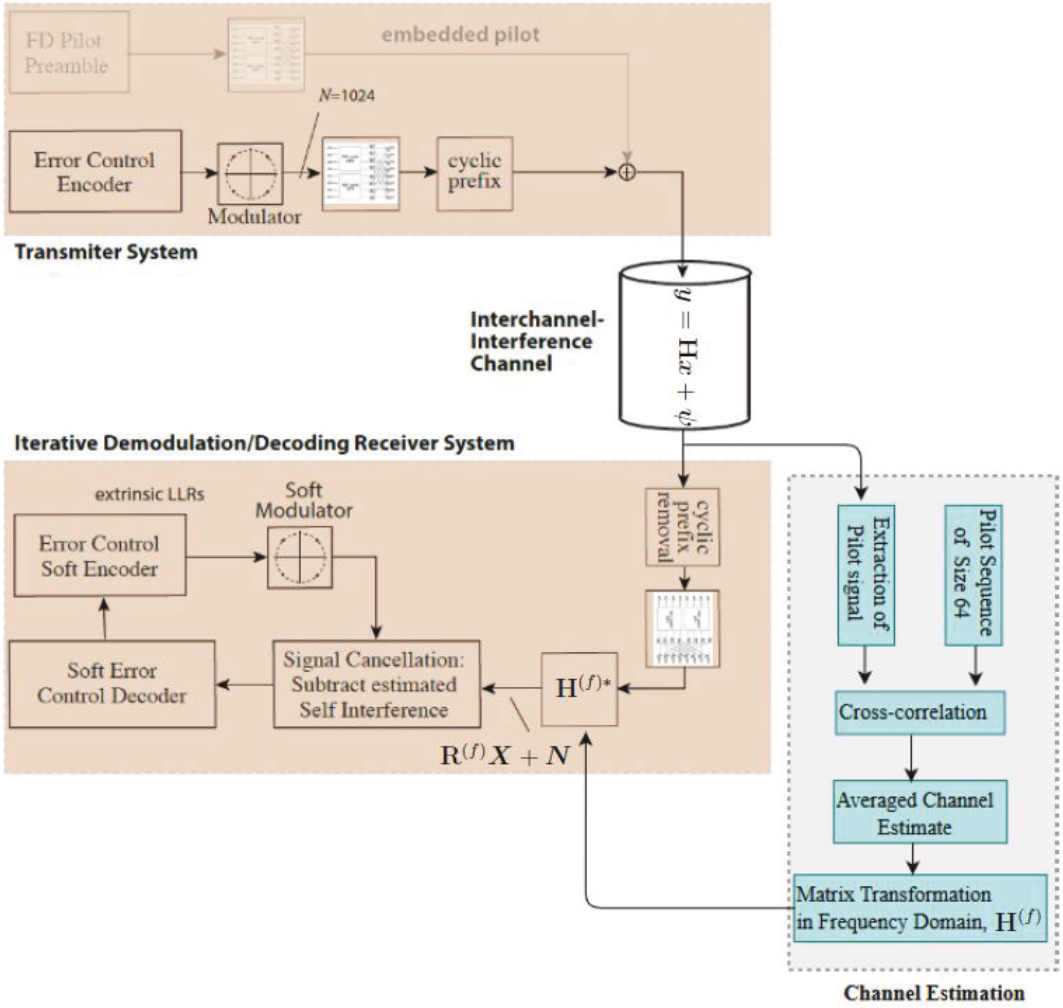

Figure 6.8: SISO representation of the Simulink model.

[2] My contribution in development of the Simulink model was to extend the model to include time-reversal signaling and channel estimation.

6.3.1 The Transmitter System

We create a sequence of shift-orthogonal preambles/pilots, each of size $N_{CP} = 64$, followed by OFDM based data symbols (of length $N + N_{CP}$ having data and CP part) for transmission. In our model, the power of the pilot and data symbols per sample is maintained unity, which can be experimented with for future applications. Preambles can be used to used to extract basic channel information such as Doppler spread and Doppler shift and delay power spectrum from the received signal.

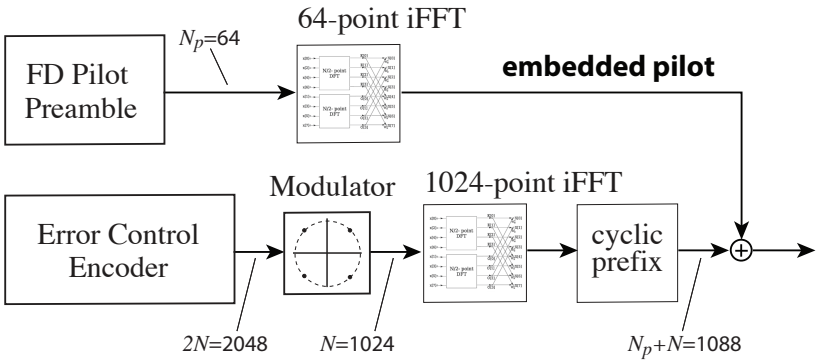

Figure 6.9: Block diagram for our Transmitter system.

For generating N_p repetitions of the preamble, we use 64 sized frame from a constellation of 8-PSK in frequency domain and transform those to time domain using the IFFT operation. The following MATLAB command was used for developing one preamble, which was then repeated N_p times in time format:
8*ifft(exp(pi*1i*randi([0,7],64,1)/4)).

We acknowledge the need of using an error correction code (ECC) or forward error correction (FEC) in an UWC due to the impairments it may carry during transmission. For an iterative receiver system, the strongest candidates for ECC to deal with acoustic channels causing inter-carrier interference (ICI) are: high rate low-density-parity-check (LDPC) and low rate repetition codes [11]. The LDPC codes, however, are sensitive to the fading risen in acoustic channels and convergence can not often be achieved. So, we choose repetition encoder for our model. Since the encoder in use is of low-rate, we achieve high spectral efficiencies by superposing 4 low-rate data streams from 4 users in our Simulink model.

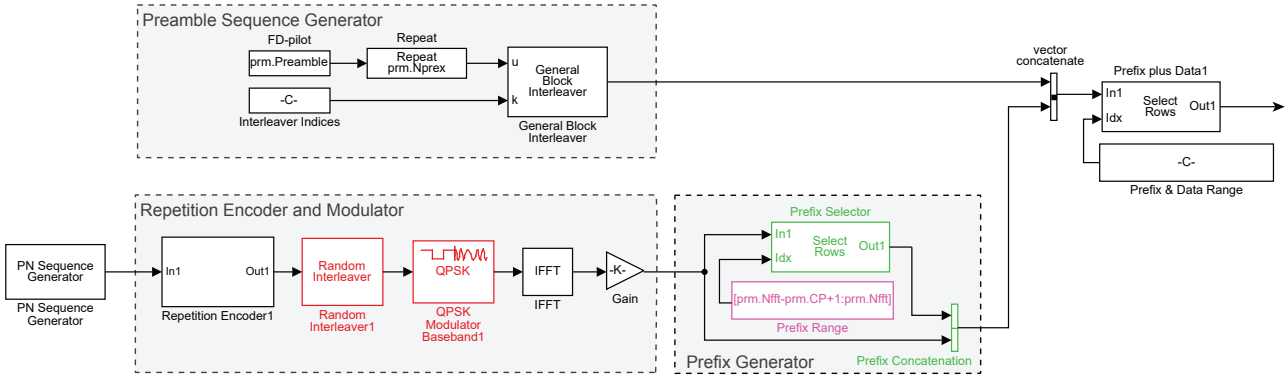

Figure 6.10: Simulink implementation of the transmitter system with one data stream. We have 4 such data streams in the complete model that are added up after QPSK modulation with gains of unity before going into the IFFT block.

Firstly, data-bits of length $N/2 = 512$ are generated through a random sequence generator (PN generator in our case) and then fed to a repetition encoder of rate $R = 1/4$, where redundant bits are added making it of length $2N = 2048$. This frame of $2N$ bits is then mapped to QPSK symbols of length $N = 1024$ and transformed to the time domain using an IFFT operation. Finally, a CP of length N_{CP} is appended in the beginning of this data signal before its transmission as in Fig. 6.9 and 6.10.

6.3.2 The Channel Model

For generating acoustic channels for simulations of our SIMO system, we have used a MATLAB script named Model_SIMO_Bellhop_v1.m given in the auxiliary files of [6]. The script is capable of producing channels in matrix form in both time and frequency domain as described in section 6.1.

The channel scenario of interest with its environmental, experimental specifications is first simulated in Bellhop ray-tracing program using an appropriate environmental file. The arrival information from these Bellhop results is then fed to the MATLAB script. The script computes RC filtering, fading effects based on SOS model, and also adds channel dynamics to the system by assigning a root-mean-square (rms) Mach factor, named ascal, for each signal bounce at the surface. The value of ascal factor indicates magnitude of time-selectivity or Doppler in the channel. The longer the interaction of multipaths with the surface, the wider Doppler spread, since surface waves are the main reasons for adding time-variations in acoustic channels.

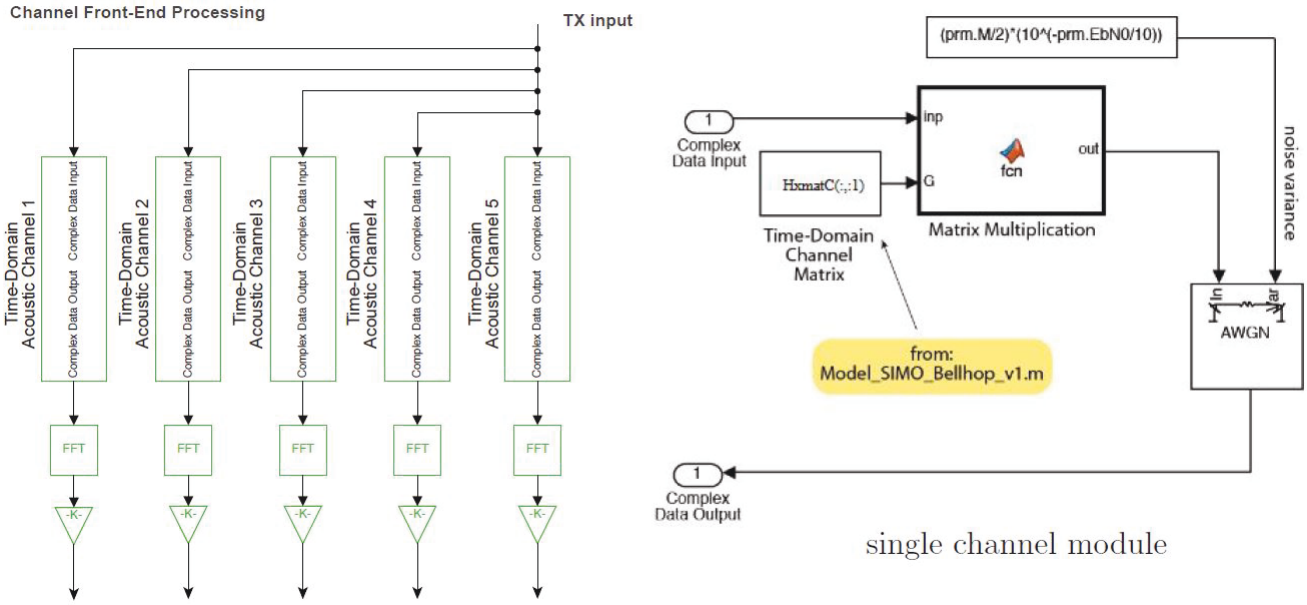

Figure 6.11: Implementing UWACs for 5 hydrophones that are extracted from Model_SIMO_Bellhop_v1.m.

Fig. 6.11 depicts the implementation of our SIMO model with 5 acoustic channels. On the right side of this figure, a single module of the SIMO system is elaborated, where channel effects are introduced by a multiplication of channel-matrix with the transmitted signal in time-domain. The background of this matrix multiplication has been described in section 6.1. The 'M' in this figure represents the repetition factor used for encoding and is 4 in our case, because we are using a rate of $R = 1/4$.

Though the SOS modeled multipath gains are normalized, the receive filter in the processing chain will partly add paths coherently. This leads to constructive and destructive interference in the discrete equivalent channel taps, which in turn is manifested in the fact that the discrete received channel power, i.e., the power of the diagonal elements in $\mathbf{R}^{(f)}$, is only approximately unity [6]. Also, due to the usage of 5 hydrophones in the SIMO system, we obtain an array gain, which is normalized out so that various arrangements can be directly compared for simulations in chapter 7. So, prm.EbN0 in Fig. 6.11 represents the normalized SNR-per-bit gain in dB.

6.3.3 Channel Estimation in the Simulink Model

A simple technique of cross-correlation is used for estimating the channels as explained in detail in section 6.2. Simulink implementation of this estimator is briefly shown in Fig. 6.12 for one hydrophone. Let's now calculate the mean squared error (MSE) of our channel estimator.

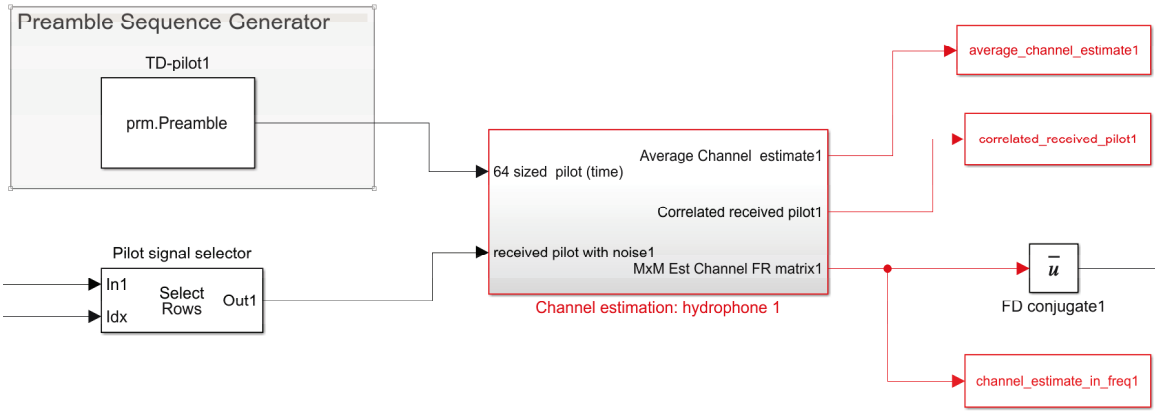

Figure 6.12: Channel estimator based on cross-correlation of the received pilot with the pilot signal at any hydrophone.

6.3.3.1 Some Channel Examples Tested with the Estimator and their MSE Performances

Theoretical MSE performance of the estimator is compared for the following channels for one hydrophone using Eq. 6.34 with its experimental performance from simulations and can be verified to match closely with one another for 0 Doppler cases. Our estimator is designed to estimate channels with delay spread ≤ 64 channel taps, where 64 is the separation between two preambles.

Example 1: Shifted-impulse channel

For this test, an impulse channel shifted in time was used in our Simulink model and MSE was averaged over 30 simulation runs, see Fig. 6.13. The AWGN variance that was added in the individual channels is also specified on x-axis of the figure. Here, "prm.M=4" represents the rate of our repetition encoder and "prm.EbN0" represents the SNR per bit in dB.

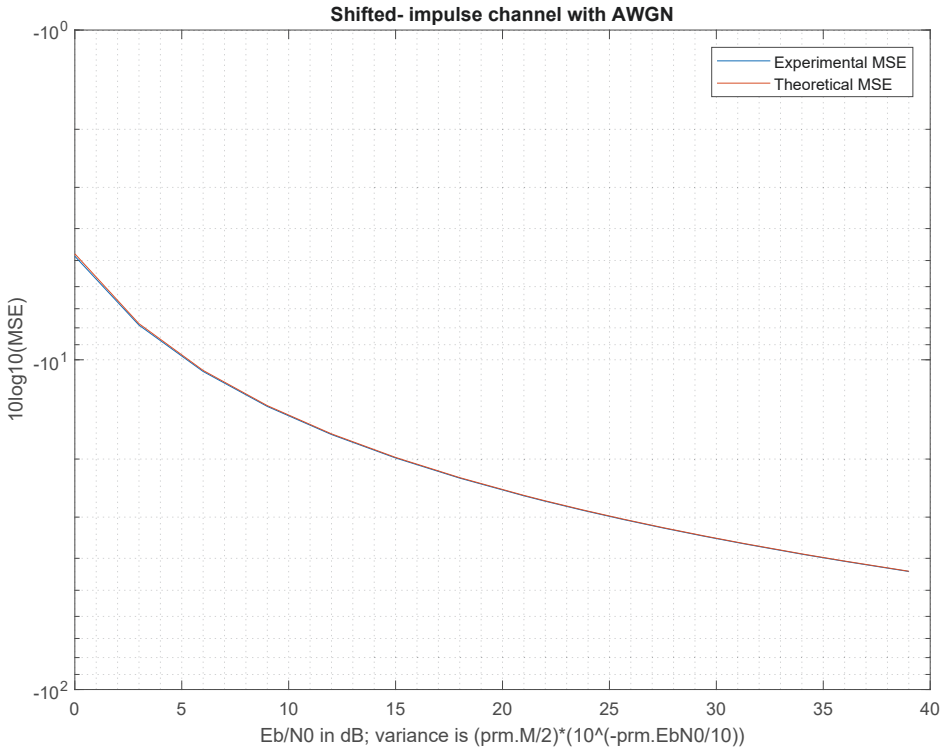

Figure 6.13: Comparison of MSE performance for a shifted-impulse channel

Example 2: No Doppler channel-1

The description of this channel is given in Appendix A. Important specifications are listed here:

$$\begin{cases} \text{1 km channel,} \\ \text{Bandwidth, } B = 320, \\ \text{Carrier Frequency, } fc = 2048, \\ \text{Sampling Rate } = Ts = 0.0031 \ s, \\ \text{Mean energy in } R^{(f)} \text{ over all hydrophones, i.e. } 1/5 \sum_{h=1}^{5} \mathrm{H_h^{(f)^*}} \mathrm{H_h^{(f)}} \text{ is 0.097979 dB,} \\ \text{Doppler (or ascal)= 0,} \\ \text{Number of preambles used, } N_p = 8 \end{cases} \tag{6.35}$$

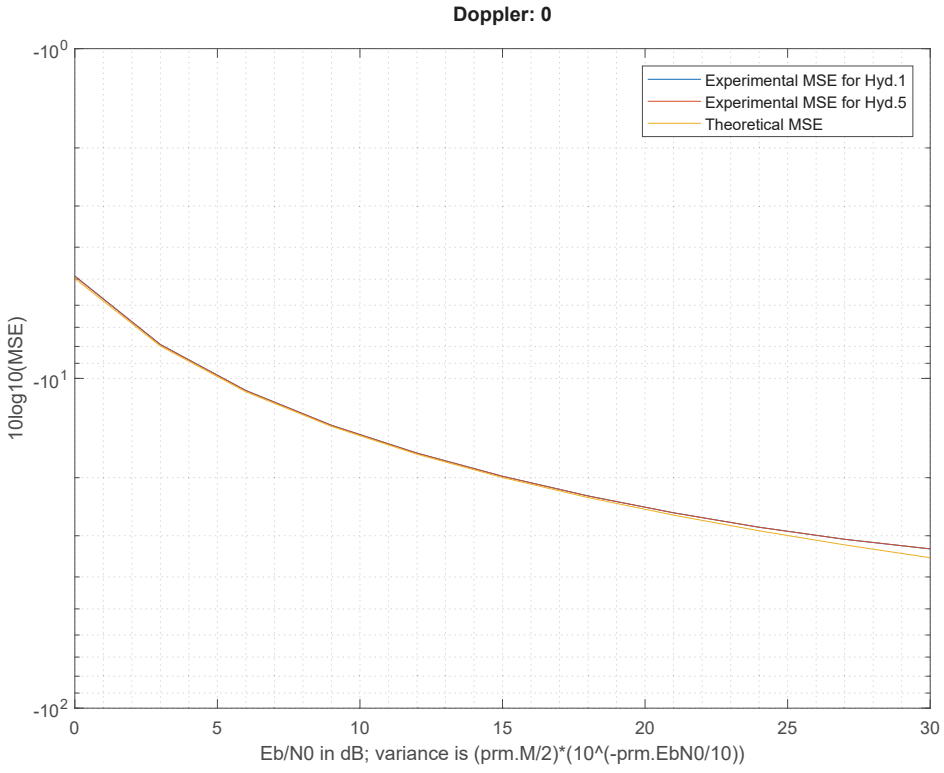

Figure 6.14: Comparison of MSE performance for channel-1

Example 3 and 4: Since our estimator was originally designed for static channels,

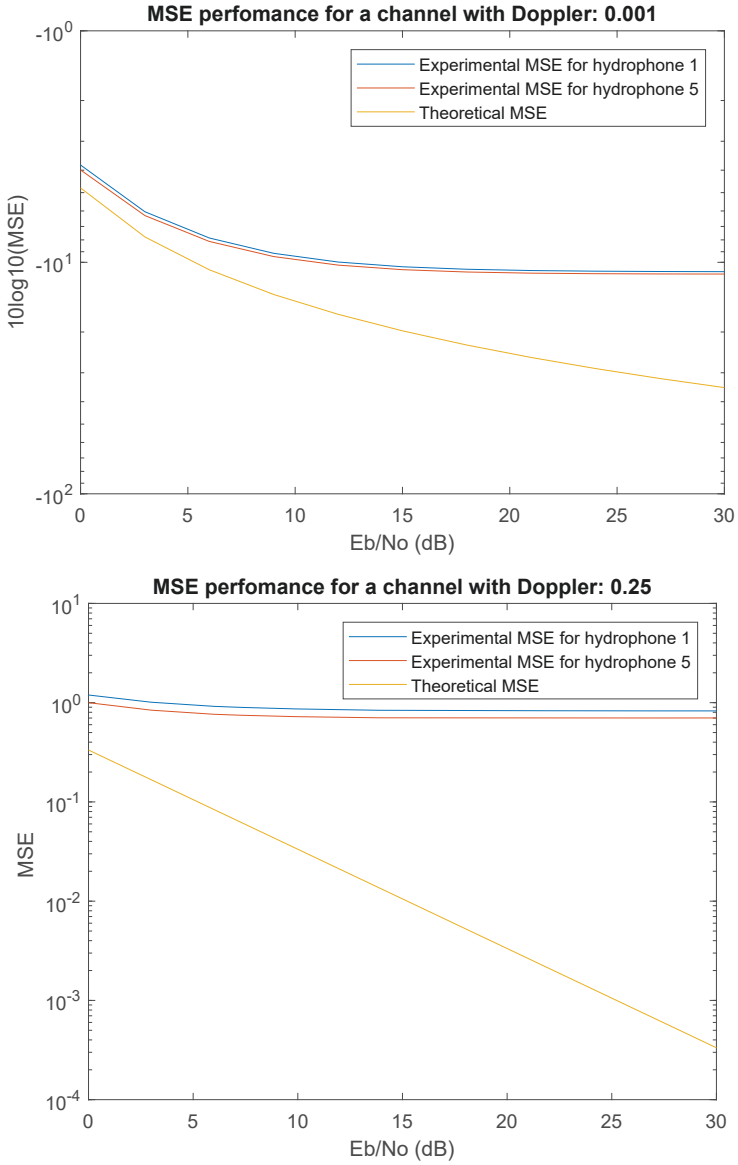

Figure 6.15: Comparison of MSE performance for a channel with ascal=0.001 and 0.25

it is evident from these examples that the estimator works very well for static fading channels with no time-variations in them. However, its performance starts deteriorating quickly for any Dopplers added in the channel. Hence, we will require an adaptive estimator for time-varying channels. Another possible solution is to use the present estimator again and again in each coherence-time window of the channel, where channel can be sufficiently assumed to be static.

6.3.4 Time-Reversal or MRC in Frequency Domain

Fig. 6.16 is the Simulink implementation of the design model explained in section 6.1 and allows matched-filtering in frequency domain on the data-signal received after transmission. The output of the MRC receiver is an energy-normalized matched filter signal in the frequency domain, which will be processed by the iterative data receiver for the purpose of removing ICI and decoding original data streams. (see Figure 6.8, where $\boldsymbol{Y}_{\mathrm{MF}}/N_h = \mathbf{R}^{(f)}\boldsymbol{X} + \boldsymbol{N}$). We can see that Eq. 6.4 is being realized in this sub-system of the Simulink model.

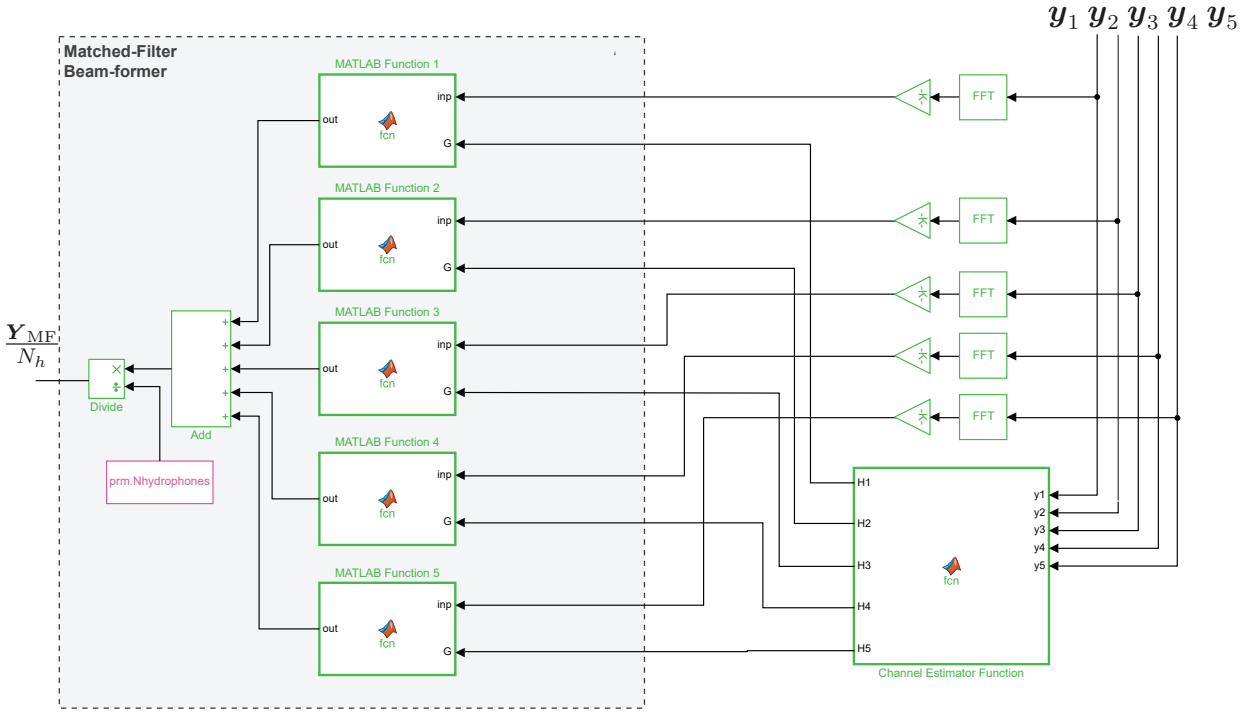

Figure 6.16: Maximum-ratio combined (MRC) beamforming receiver.

.

6.3.5 The Receiver Chain

Decoding and demodulation is achieved via iterative cancellation as shown in Figure 6.8. The iterative decoding system is not the focus of this thesis work and is briefly discussed here. For details of its working, section 4.4.4 in [6] can be referred.

The received signal is repeatedly decoded with a soft-output decoder which produces log-likelihood ratios of the data bits depending on their current probabilities in any given iteration. These log-likelihood ratios are then converted into soft bits, real numbers in the range $[-1, 1]$, encoded, modulated, and then used to subtract the self-interference created by the non-ideal channel $\mathbf{R}$, that is, by the off-diagonal elements of $\mathbf{R}$. Ideally this process will completely remove the off-diagonal elements and render a fully diagonalized channel model after I iterations given by

$$\begin{aligned} \boldsymbol{Y}_{\mathrm{MF}}^{(I)} &= \operatorname{diag}\left\{\mathbf{H}^{(f*)}\mathbf{H}^{(f)}\right\}\boldsymbol{X} + \boldsymbol{N} \\ &= \operatorname{diag}\left\{\mathbf{R}^{(f)}\right\}\boldsymbol{X} + \boldsymbol{N} \end{aligned} \tag{6.36}$$

and thus have removed the effects of interchannel-interference and restored the ideal diagonalized OFDM frequency-domain channel (6.2).

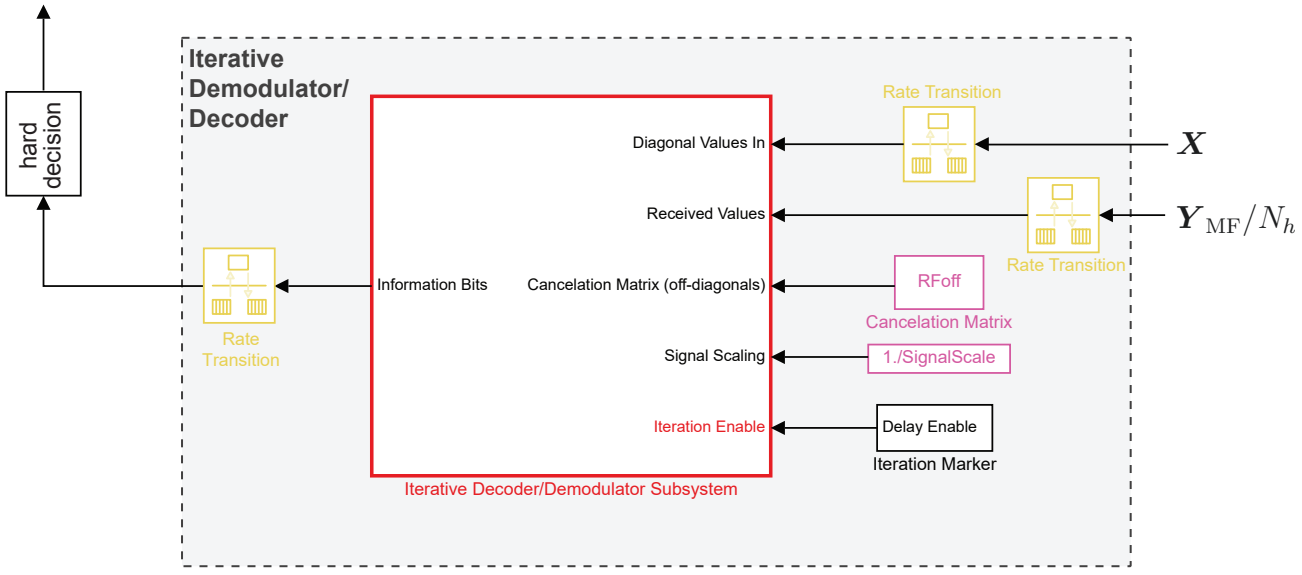

Figure 6.17: Generic iterative demodulator/decoder block for one user.

Chapter 7

Simulation Results of the OFDM-TR Model in Simulink

Various test-channels of interest, described in appendix A, are first generated through a MATLAB-Bellhop script called Model_SIMO_Bellhop_v1.m and then fed into our complete Simulink model, called Complete_model_estimator_with_TR_simulink.slx, for generation of the following bit-error-rate (BER) results. These simulation results are simulated for all the 4 users in the model for two cases: 1) when channels are assumed to be known at the 5 receivers and are used for matched-filtering in MRC combining without any use of the estimator. The corresponding BERs for this case are marked by a legend 'No est.', indicating no use of the estimator. 2) when channel estimates are calculated from the estimator and used for matched-filtering in MRC combining. The BERs for this case are marked by a legend 'Est.', indicating use of the estimator.

7.1 Gaussian Channel

First of all the simulations undertaken through the complete OFDM-TR model is for a Gaussian channel. A Gaussian channel matrix is developed in a separate MATLAB script before inputting it to the Simulink model.

The original model is developed to estimate upto 64 channel taps and use those estimates for MRC combining process. For an AWGN channel, however, we have only one channel tap that is to be estimated. Therefore, the other 63 taps were forced to zero to produce results shown in Fig. 7.1. These outcomes comply with the theoretical results for an ideal QPSK and prove the MSE performance of the channel estimator for an AWGN channel as in section 6.3.3.1 .

Since, we are also interested in calculating the degradation in signal-to-noise-ratio (SNR) due to use of our estimator, we re-simulate results for AWGN channel without forcing 63 taps equal to zero as done earlier and hence use the original Simulink as it

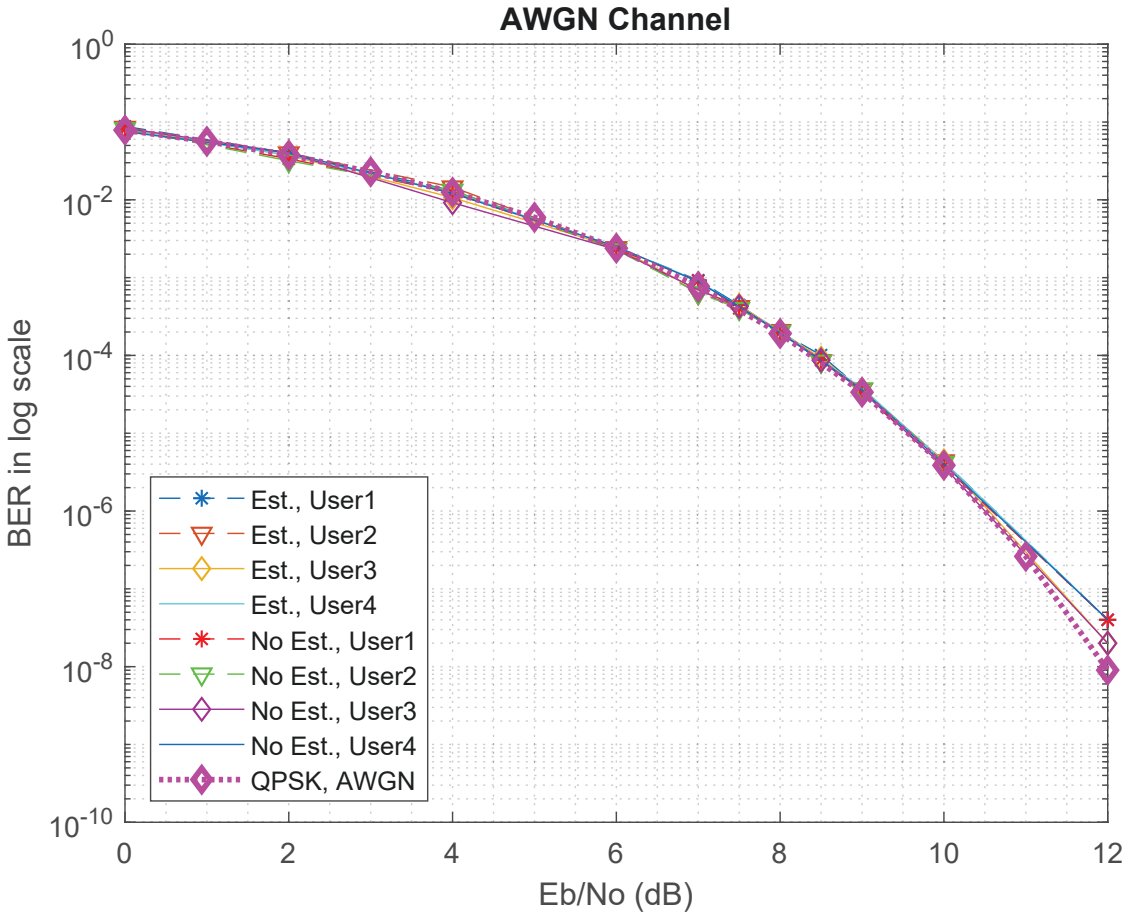

Figure 7.1: The BER performances of the channel estimator are compared on an AWGN channel with one channel-tap using the Simulink model presented in Section 6.2.

is. Fig. 7.2 shows BER performances for the original model for an AWGN channel.

For this simulation, the model explained in Section 6.2 is used. Here is a summary of the parameters employed

$$\text{Eb/N0 vector} = [0, 2, 4, 6, 7, 7.5, 8, 8.5, 9, 10, 12]$$
$$10^6, 6 * 10^6, 10^7, 5 * 10^7],$$
$$\text{Number of hydrophones } (N_{hyd}) = 5,$$
$$\text{Number of channel taps } (N_h) = 64,$$
$$\text{Energy of the pilot signal } (E_x) = 64.$$

There have been enough number of transmissions at each Eb/N0 to calculate BERs.

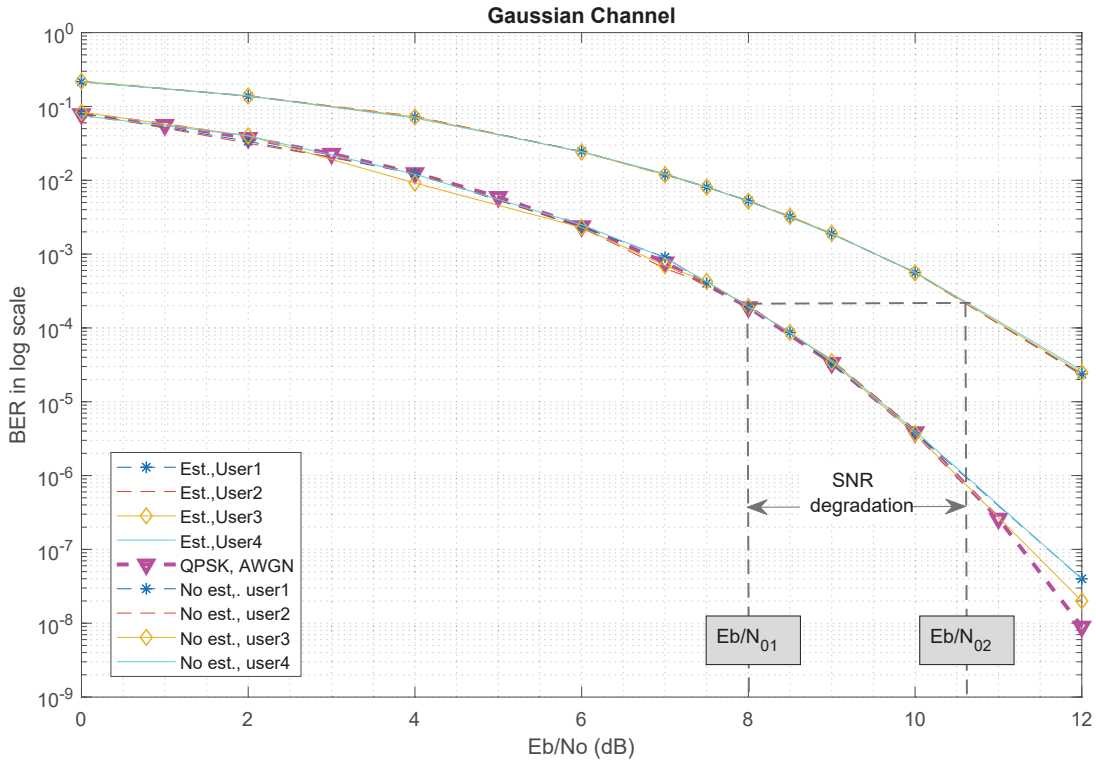

Figure 7.2: The BER performances of the channel estimator are compared on an AWGN channel using the Simulink model presented in Section 6.2.

The pilot signal, $b_M[n]$ of size 64, is generated in MATLAB using shift-orthogonal 8-PSK sequences. [1]

Derivation of the SNR

For a simple channel like AWGN, we can say that the loss in SNR between the experimental and ideal graphs at any given BER is due to the noise added by the channel estimator. From the figure, this degradation in dB and linear scale can be written as

$$\begin{aligned}\Delta\text{SNR}(dB) &= \left(\frac{Eb}{N_{02}}\right)_{dB} - \left(\frac{Eb}{N_{01}}\right)_{dB} \\ &= 10\,\log_{10}\left(\frac{Eb}{N_{02}}\right)_{l} - 10\,\log_{10}\left(\frac{Eb}{N_{01}}\right)_{l} \\ &= 10\,\log_{10}\left(\frac{N_{01}}{N_{02}}\right)_{l} \end{aligned} \tag{7.1}$$

[1] The seed for random generator is 251 and for AWGN Simulink blocks for the 5 hydrophones are set to: {488611166, 6441, 7837, 251, and 6377}

and

$$\Delta\text{SNR}(l) = \left(\frac{N_{01}}{N_{02}}\right)_l \tag{7.2}$$

Using Eq. 6.10, we note that N_{01} can be expressed in terms of N_{02} as

$$N_{02} = N_{01} + \sigma^2_{\text{MSE}} \left(\frac{\left|X[0]\right|^4}{N} + \sigma^2_w\right) \tag{7.3}$$

For a SISO model, we require only one channel estimator. Hence, the variance of the estimator can be derived from Equations 6.18 and 6.34 as

$$\sigma^2_{\text{MSE}_i} = \frac{N_h}{E_x N_p}\sigma^2_w.$$

However, for a SIMO model as used for Fig. 6.2, the total variance is

$$\sigma^2_{\text{MSE}} = \frac{N_h N_{hyd}}{E_x N_p}\sigma^2_w, \text{where } N_{hyd} \text{ is the number of hydrophones} \tag{7.4}$$

Using Equations 7.3, 7.4 and 6.10, the SNR degradation in Eq. 7.2 for a SIMO system is

$$\begin{aligned}
\Delta\text{SNR}(l) &= \left(\frac{N_{01}}{N_{01} + \sigma^2_{\text{MSE}}\left(\frac{\left|X[0]\right|^4}{N} + \sigma^2_w\right)}\right)_l \\
&= \left(\frac{5\sigma^2_w}{5\sigma^2_w + \sigma^2_{\text{MSE}}\left(\frac{\left|X[0]\right|^4}{N} + \sigma^2_w\right)}\right)_l \\
&\quad [\because N_{01} \text{ is the variance of the WGN process}]
\end{aligned} \tag{7.5}$$

For our simulations in Fig. 7.2, the estimates from the first and last preamble were ignored before taking the average as those two were affected by the cross-correlation noise. Hence, only 6 preambles out of 8 were used.

For our simulation model where $N_{hyd} = 5$, $N_h = 64$ and pilot energy of 64, the above formula at Eb/N0 =$\{0, 2, 4, 6\}$ dB gives us an expected SNR degradation of {-4.27, -3.14, -2.23, -1.54} dB. These theoretical degradations at various Eb/N0s are near to what we realize in the simulation results. The difference in the two is anticipated from the assumption we have made in Eq. 6.9 that estimation-error-matrix and noise vector are Gaussian distributed and independent.

Therefore, we can say that it is evident from Fig. 7.2 that the SNR degradation approaches its theoretical value everywhere, which is given by Eq. 7.5.

7.2 Static Frequency-Selective Channel

Test Channel: Channel-1

Important specifications of the channel are outlined below. For details of the Channel-1 extracted from 1 km channel, see appendix A.

$$\begin{cases} \text{1 km channel,} \\ \text{Bandwidth, } B = 320, \\ \text{Carrier Frequency, } fc = 2048, \\ \text{Sampling Rate } = Ts = 0.0031 \ s, \\ \text{Mean energy in } R^{(f)} \text{ over all hydrophones, i.e. } 1/5 \sum_{h=1}^{5} \mathrm{H_h^{(f)^*}} \mathrm{H_h^{(f)}} \text{ is 0.097979 dB,} \\ \text{Doppler (or ascal)= 0,} \\ \text{Number of preambles used, } N_p = 8 \end{cases} \tag{7.6}$$

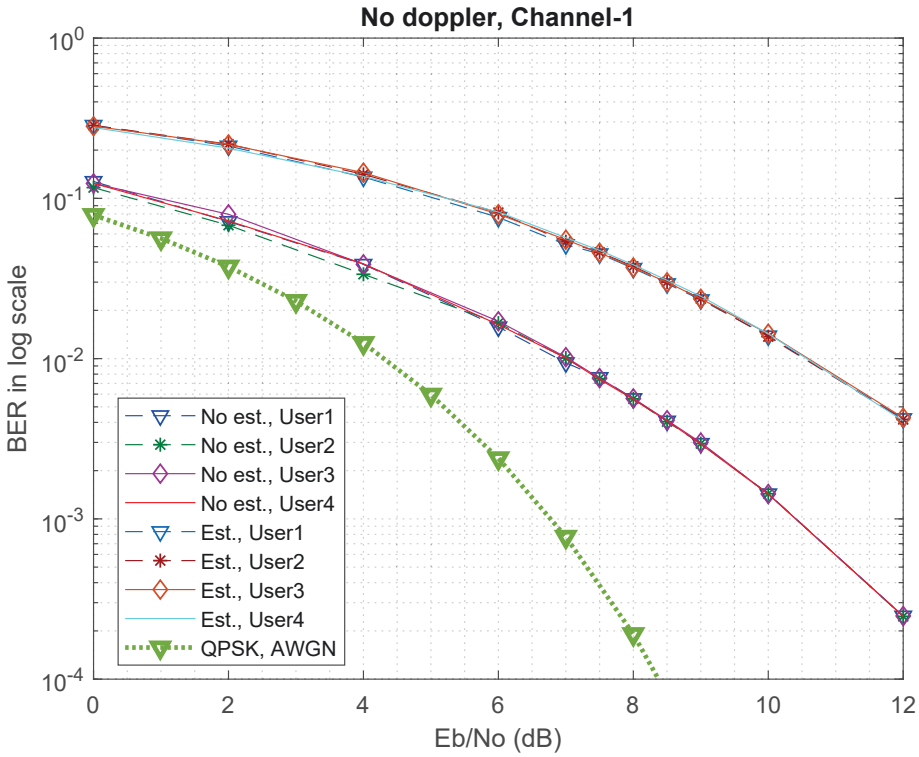

Figure 7.3: The BER performances of the channel estimator are compared on a no Doppler channel-1 using the Simulink model.

Test Channel: Channel-2

Important specifications of the channel are outlined below. For details of the Channel-2 from 1 km channel, see appendix A.

$$\begin{cases} \text{1 km channel,} \\ \text{Bandwidth, } B = 320, \\ \text{Carrier Frequency, } fc = 2048, \\ \text{Sampling Rate } = Ts = 0.0031 \ s, \\ \text{Mean energy in } R^{(f)} \text{ over all hydrophones, i.e. } 1/5 \sum_{h=1}^{5} \mathrm{H_h^{(f)^*}} \mathrm{H_h^{(f)}} \text{ is 0.18365 dB,} \\ \text{Doppler (or ascal)= 0,} \\ \text{Number of preambles used, } N_p = 8 \end{cases} \tag{7.7}$$

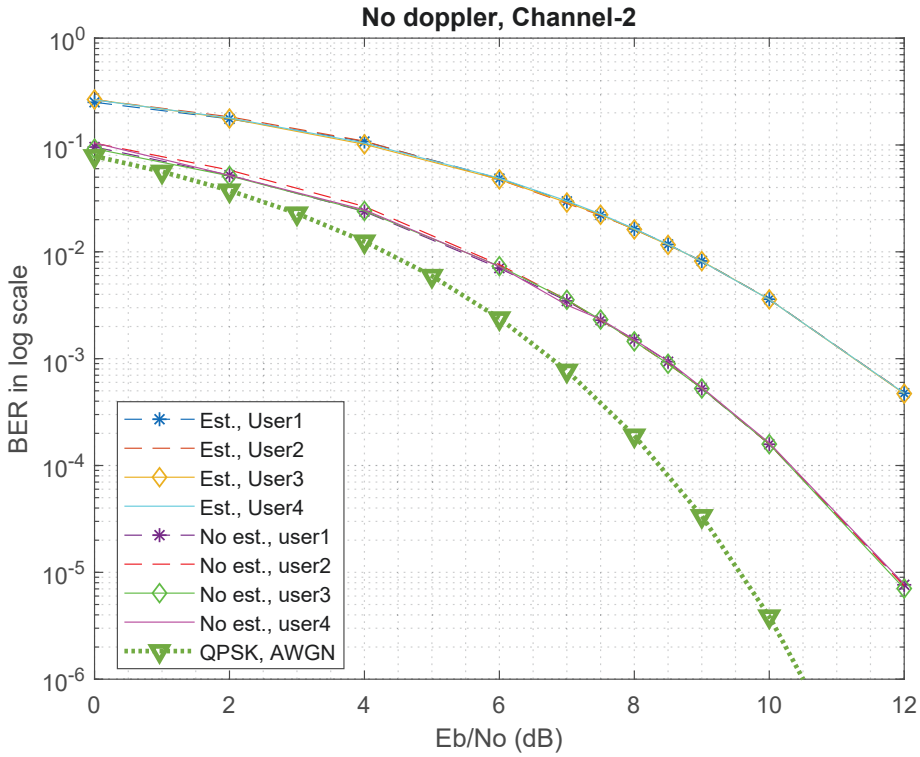

Figure 7.4: The BER performances of the channel estimator are compared on a no Doppler channel-2 using the Simulink model.

7.3 Channel with Low Doppler

Test Channel: Channel-3

For the generation of this particular channel, arrival information from 1-km channel was considered but with different bandwidth and carrier frequency to see the impact of these parameters on the TR performance.

$$\begin{cases} \text{1 km channel,} \\ \text{Bandwidth, } B = 1000, \\ \text{Carrier Frequency, } fc = 3500, \\ \text{Sampling Rate } = Ts = 10^{-3}\ s, \\ \text{Mean energy in } R^{(f)} \text{ over all hydrophones, i.e. } 1/5 \sum_{h=1}^{5} \mathrm{H}_{\mathrm{h}}^{(f)^*} \mathrm{H}_{\mathrm{h}}^{(f)} \text{ is -0.1926 dB,} \\ \text{Doppler (or ascal)= 0.001,} \\ \text{Number of preambles used, } N_p = 8 \end{cases} \tag{7.8}$$

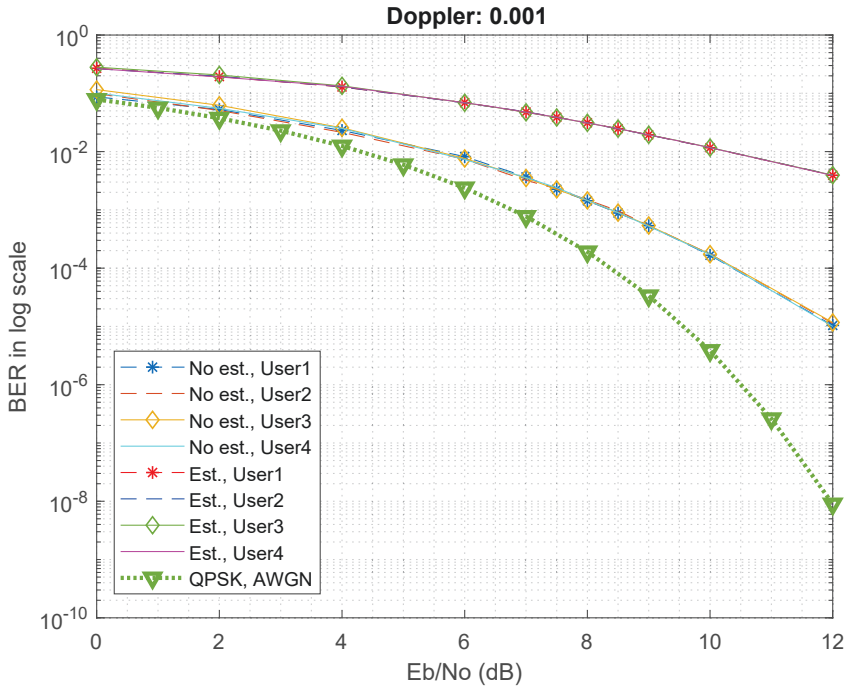

Figure 7.5: The BER performances of the channel estimator are compared on a 0.001 Doppler channel-3 using the Simulink model.

Test Channel: Channel-4

Important specifications of the channel are outlined below. For details of the Channel-4 extracted from 1 km channel, see appendix A.

$$\begin{cases} \text{1 km channel,} \\ \text{Bandwidth, } B = 320, \\ \text{Carrier Frequency, } fc = 2048, \\ \text{Sampling Rate } = Ts = 0.0031 \ s, \\ \text{Mean energy in } R^{(f)} \text{ over all hydrophones, i.e. } 1/5 \sum_{h=1}^{5} \mathrm{H}_{\mathrm{h}}^{(f)^*} \mathrm{H}_{\mathrm{h}}^{(f)} \text{ is -0.0062121 dB,} \\ \text{Doppler (or ascal)= 0.01,} \\ \text{Number of preambles used, } N_p = 8 \end{cases} \tag{7.9}$$

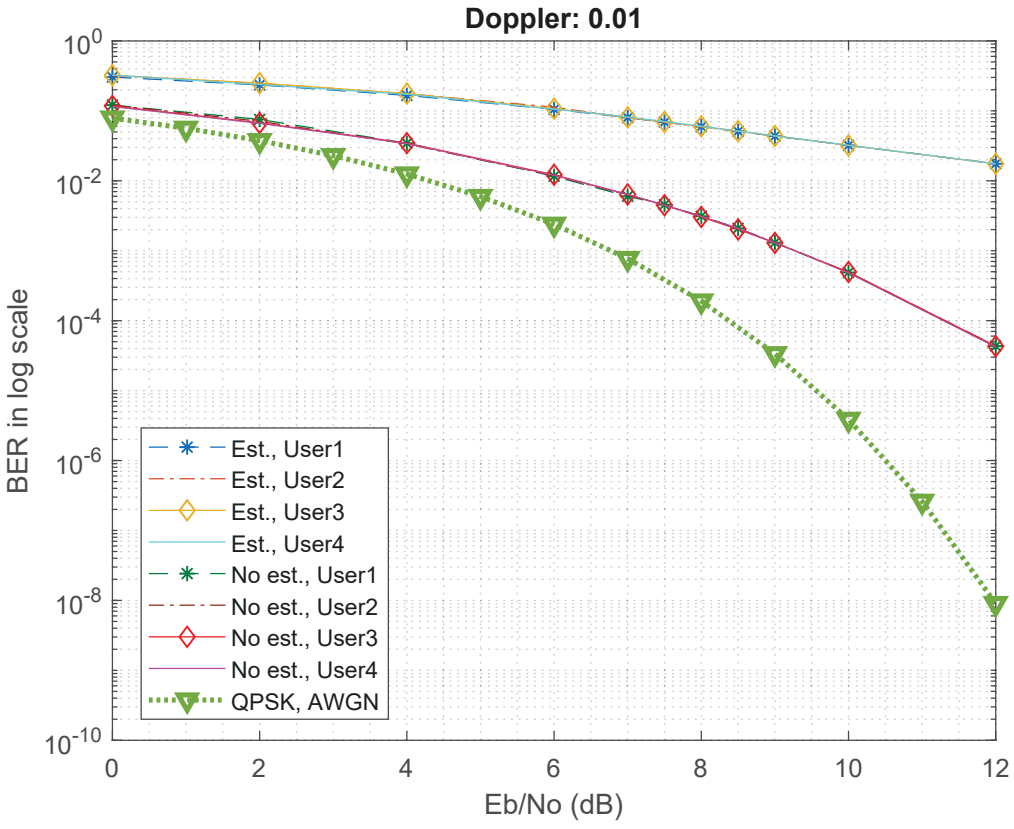

Figure 7.6: The BER performances of the channel estimator are compared on a 0.01 Doppler channel-4 using the Simulink model.

7.4 Channel with Low Doppler from Literature

Test Channel: H.C. Song-Bellhop

This channel has been discussed from literature in section 4.2. Visualization of its channel matrix in time and frequnecy domain is plotted in appendix A. Since there were no surface bounces observed for this channel example, setting $ascal = 0.25$ in the MATLAB-Bellhop script was irrelevant, and hence no Doppler was added due to surface waves in the channel model for simulations presented in Fig. 7.7.

$$\begin{cases} \text{H.C. Song channel,} \\ \text{Bandwidth, } B = 1000;\ \text{Carrier Frequency, } fc = 3500;\ \text{Sampling Rate , } Ts = 10^{-3}\ s, \\ \text{Mean energy in } R^{(f)} \text{ over all hydrophones is -0.36076 dB,} \\ \text{Doppler (or ascal)= 0.25;}\ \text{Number of preambles used, } N_p = 8. \end{cases} \tag{7.10}$$

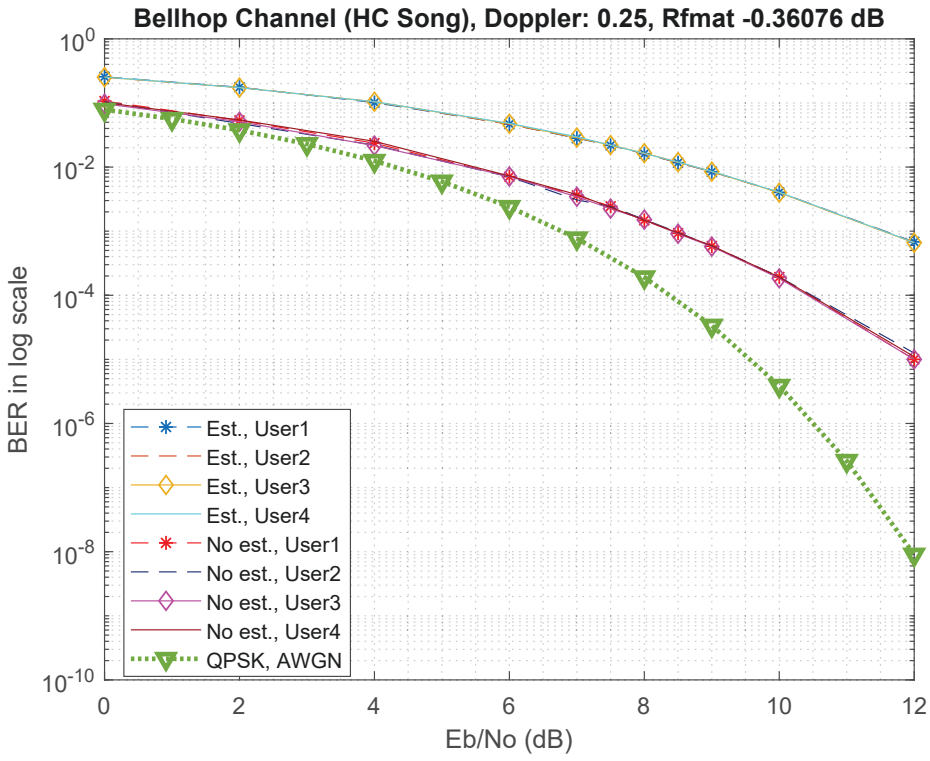

Figure 7.7: The BER performances of the channel estimator are compared for the channel from section 4.2 using the Simulink model.

7.5 Channel with Higher Doppler

Test Channel: Channel-5

See appendix A for more details of the channel.

$$\begin{cases} \text{1 km channel,} \\ \text{Bandwidth, } B = 320;\ \text{Carrier Frequency, } fc = 2048;\ \text{Sampling Rate } = Ts = 0.0031\ s, \\ \text{Mean energy in } R^{(f)} \text{ over all hydrophones is -0.856 dB,} \\ \text{Doppler (or ascal)= 0.25;}\ \text{Number of preambles used, } N_p = 8. \end{cases}$$

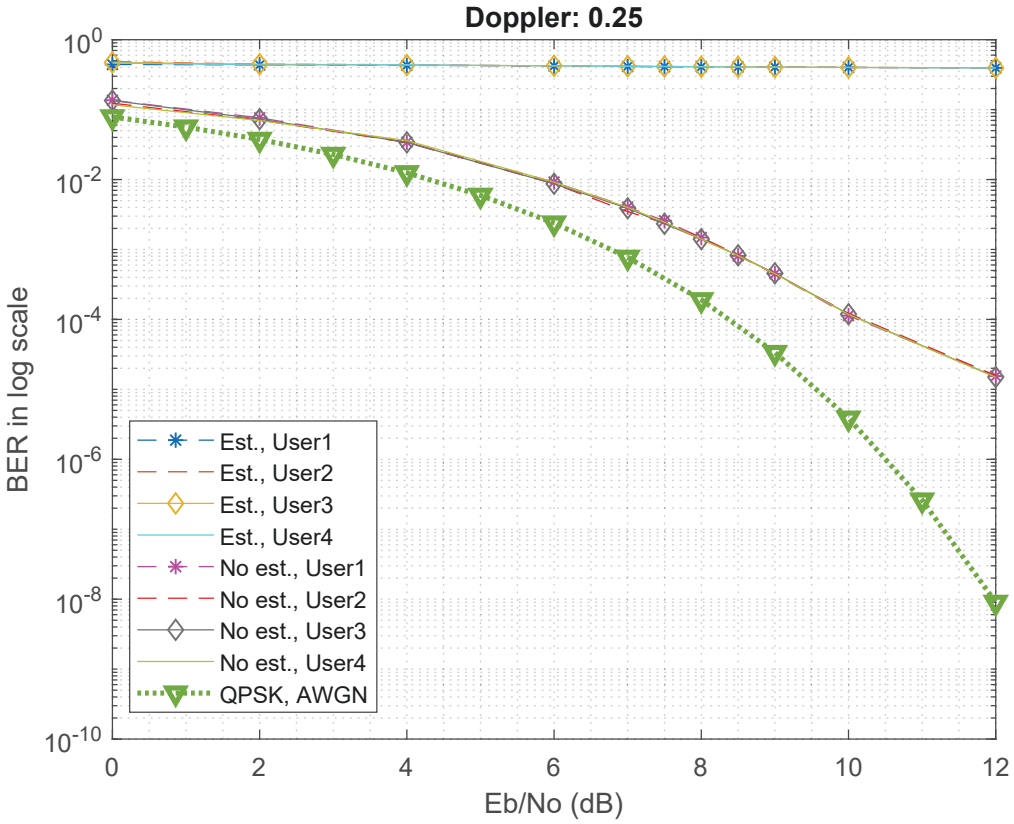

Figure 7.8: The BER performances of the channel estimator are compared on a 0.25 Doppler channel-5 using the Simulink model.

7.6 Comparison of Various Test Channels for Known and Estimated Channels

A summary of performance of our OFDM-TR Simulink model for various simulations listed so far in this chapter is demonstrated in Fig. 7.10 for one out of the 4 users. This figure shows comparison of the test channels for the cases where actual channels are assumed to be known at the receiver end and are used for matched-filtering. A similar comparison has been made for the BER performance for user 1 for the cases where rather the estimated channels are used for matched-filtering. This is demonstrated in Fig. 7.9.

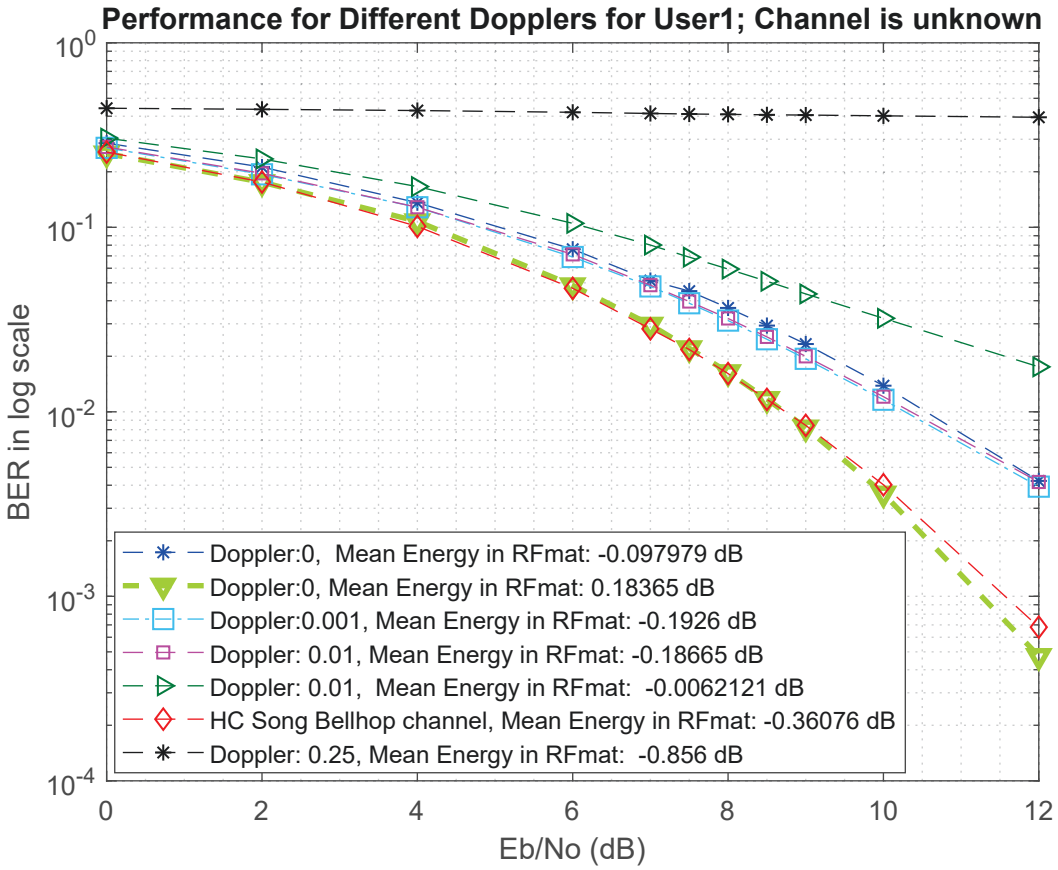

Figure 7.9: The BER performances of the channel estimator are compared for various Dopplers using the OFDM-TR Simulink model.

From figures 7.9 and 7.10, it is clear that the performance of time-reversal generally worsens with an increase in Doppler in the channel. However, only two curves do not follow this trend. Since, only one realization of various test channels was used for

BER simulations, these two off-trend channels seem to be unfortunate cases of time and frequency selectivity as given in appendix A. It is also to be noted that these results are for a heavy data transmission with a superposition of 4 data streams as discussed earlier. These performances can be further enhanced by using less number of data streams and more number of iterative cancellations for removing ICI in the channel.

In Fig. 7.9, the reason of the degradation in performance with higher Dopplers as compared to in 7.10 is mainly fact that our non-adaptive estimator was designed only for static channels and its performance starts failing for higher Dopplers as is expected.

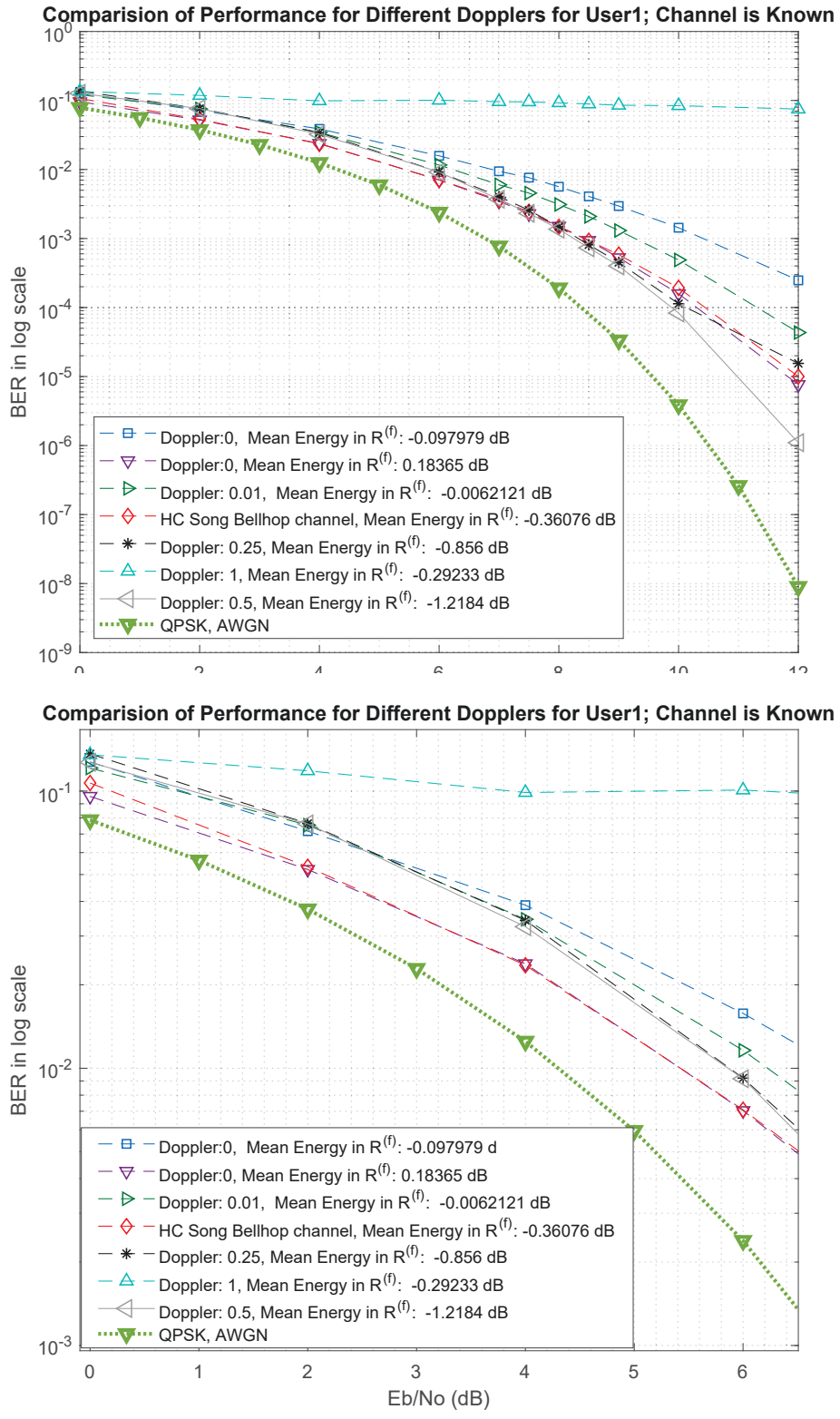

Figure 7.10: The BER performances of the OFDM-TR model are compared for various Dopplers when channels are known. Bottom graph illustrates the zoomed-in view of this comparison.

Chapter 8

Conclusions and Future Work

In this thesis work, applicability of time-reversal signalling and the presented channel estimator was tested in various acoustic channel environments. It was found from the Bellhop simulations that in propagation case studied by [14], time-reversal is indeed applicable for transmission over long distances since the Doppler spread inducing surface reflections are largely absent in the received signal. This also underlined the importance of transmitter-receiver placement in an UWA channels. Secondly, we developed an OFDM based time-reversal simulation model in MATLAB/Simulink to test performance of TR against various Dopplers. It was demonstrated that TR is adequate for channels only with low Dopplers and that its performance degrades quickly for high Dopplers. This also agrees with the conclusion from Bellhop simulations of the channel discussed from literature in [14].

Finally, it was shown that our basic estimator was designed for static channels and works well for very low Doppler scenarios with some expected degradation in SNR. Its performance fails heavily for higher Dopplers. Therefore, either an adaptive channel estimation or re-calculation of channel impulse response using our estimator would be needed to serve TR for higher Doppler environments. A block-by-block approach can be useful in such cases, where the signal is transmitted only for durations within coherence time so the channel can be assumed to be time-invariant and hence our estimator can be used. For the duration outside coherence time, the estimator would need to be updated either by using frequent transmission of probe signals or using an estimation algorithm. Further, the present model does not incorporate Doppler shift but only Doppler spreads and hence a provision for compensation of Doppler shift can be another enhancement as a part of future work.

Bibliography

[1] Barker-code. available at:
https://en.wikipedia.org/wiki/barker-code.

[2] Circulant-matrices. (n.d.). [ebook] available at:
http://web.mit.edu/18.06/www/spring17/circulant-matrices.pdf.

[3] Pseudo-noise-sequences. available at:
https://paginas.fe.up.pt/ hmiranda/cm/pseudo-noise-sequences.pdf.

[4] Geoffrey F Edelmann, T Akal, William S Hodgkiss, Seongil Kim, William A Kuperman, and Hee Chun Song. An initial demonstration of underwater acoustic communication using time reversal. *IEEE journal of oceanic engineering*, 27(3):602–609, 2002.

[5] C. Schlegel et al. Umdcc report, 2016. available at http://umdcc.ca/resources/.

[6] C. Schlegel et al. Umdcc report, 2017. available at http://umdcc.ca/resources/.

[7] Jens M Hovem. Ray trace modeling of underwater sound propagation. In *Modeling and Measurement Methods for Acoustic Waves and for Acoustic Microdevices*. InTech, 2013.

[8] University of Rhode Island and Inner Space Center. Discovery of sound in the sea, 2017.

[9] Michael B Porter. The bellhop manual and users guide: Preliminary draft. *Heat, Light, and Sound Research, Inc., La Jolla, CA, USA, Tech. Rep*, 2011.

[10] Daniel Rouseff, Darrell R Jackson, Warren LJ Fox, Christopher D Jones, James A Ritcey, and David R Dowling. Underwater acoustic communication by passive-phase conjugation: Theory and experimental results. *IEEE Journal of Oceanic Engineering*, 26(4):821–831, 2001.

[11] Christian Schlegel and Marat V Burnashev. The interplay between error control coding and iterative signal cancelation. *IEEE Transactions on Signal Processing*, 65(11):3020–3031, 2017.

[12] Kunal Singhal. Walsh-codes, pn sequences and their role in cdma technology. *CSE Department, IIT Delhi*, pages 1–4, 2012.

[13] H. C. Song. An overview of underwater time-reversal communication. *IEEE Journal of Oceanic Engineering*, 41(3):644–655, July 2016.

[14] H. C. Song, W. S. Hodgkiss, W. A. Kuperman, M. Stevenson, and T. Akal. Improvement of time-reversal communications using adaptive channel equalizers. *IEEE Journal of Oceanic Engineering*, 31(2):487–496, April 2006.

[15] HC Song and WS Hodgkiss. Self-synchronization and spatial diversity of passive time reversal communication. *The Journal of the Acoustical Society of America*, 137(5):2974–2977, 2015.

[16] HC Song, WA Kuperman, and WS Hodgkiss. Basin-scale time reversal communications. *The Journal of the Acoustical Society of America*, 125(1):212–217, 2009.

[17] Milica Stojanovic. Retrofocusing techniques for high rate acoustic communications. *The Journal of the Acoustical Society of America*, 117(3):1173–1185, 2005.

[18] Milica Stojanovic, J Catipovic, and John G Proakis. Adaptive multichannel combining and equalization for underwater acoustic communications. *The Journal of the Acoustical Society of America*, 94(3):1621–1631, 1993.

[19] Robert J Urick. *Principles of underwater sound for engineers*. Tata McGraw-Hill Education, 1967.

[20] Wikipedia contributors. Speed of sound — Wikipedia, the free encyclopedia, 2018.

[21] TC Yang. Temporal resolutions of time-reversal and passive-phase conjugation for underwater acoustic communications. *IEEE Journal of Oceanic Engineering*, 28(2):229–245, 2003.

[22] TC Yang. Channel q function and capacity. In *OCEANS, 2005. Proceedings of MTS/IEEE*, pages 273–277. IEEE, 2005.

Appendices

Appendix A

Test Channels

A.1 1 km Channel

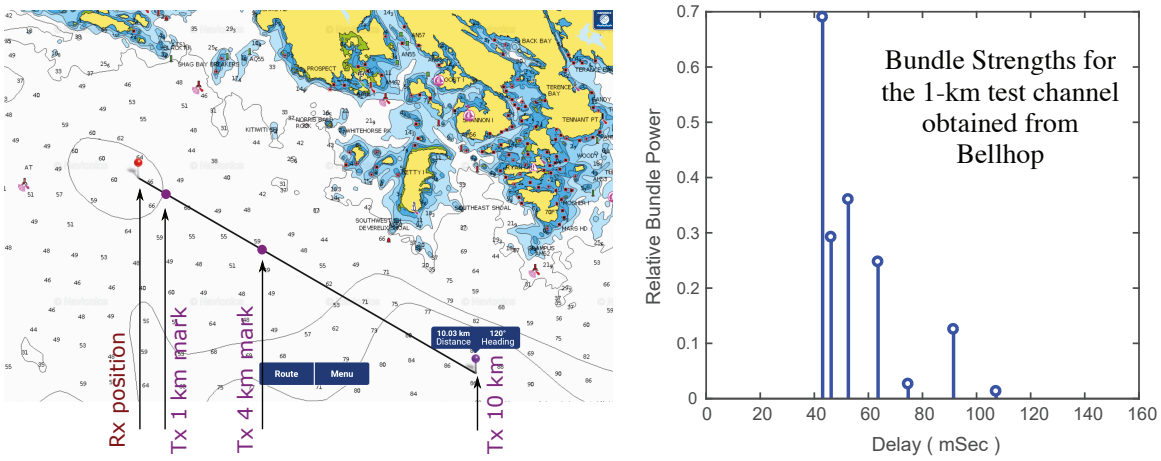

Figure A.1: Location of the Dalhousie channel measurements and the realization of power-delay profile for 1 km channel in Bellhop [6].

Dalhousie conducted a measurement campaign in Summer 2017 in the Bay of St. Margaret, Nova Scotia, Canada with an aim to better understand and analyze real acoustic environments for various transmission ranges. The experiment has been discussed in details in [6].

For the simulations performed in this thesis, we have used 1-km channel measurements, which are briefly summarized here. The site was a shallow-water environment with depths of about 60-80 m and 1 km of transmission range with hard bottom. OFDM symbol duration was set to N = 1024 samples. The carrier frequency used for transmission was 2048 Hz with a bandwidth of 320 Hz. A root-raised cosine filtering with a roll-off 0.2 was applied at the transmitter and receiver. The power-delay profile of this channel scenario was realized in Bellhop and is produced in Fig. A.1. The Doppler spectrum for the 1-km channel with its Doppler-delay profile is depicted in Fig. A.2. For this channel, Bellhop anticipates a path loss of 52 dB. A vertical

line receive hydrophone-array with 5 elements was considered, which were kept 36 cm apart.

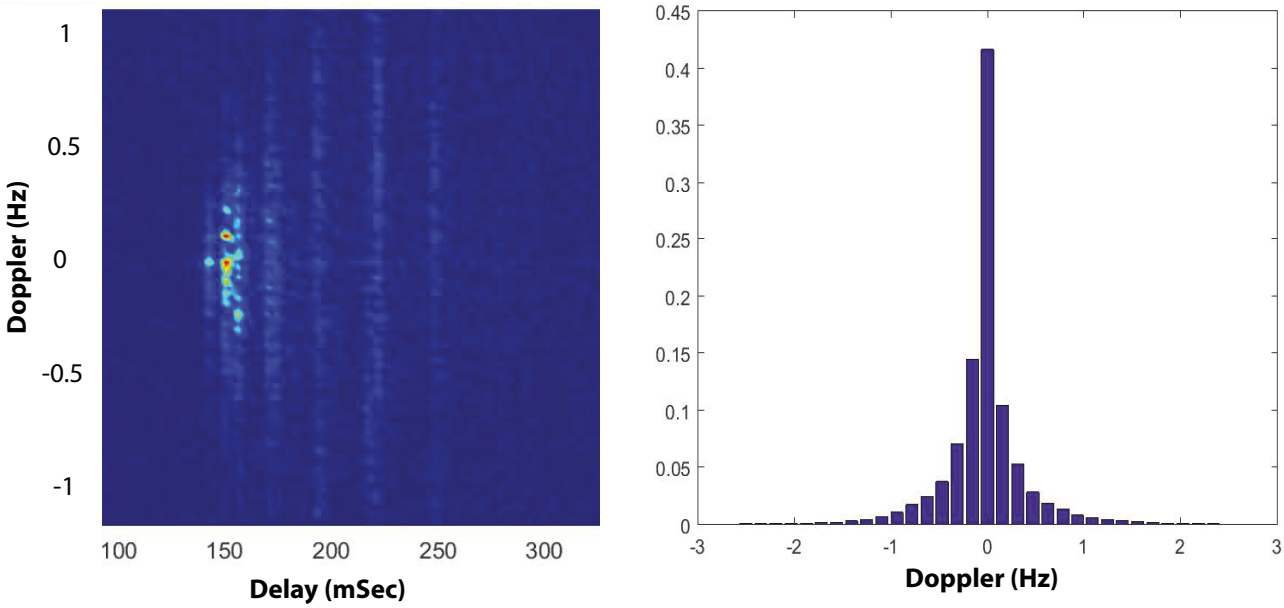

Figure A.2: Doppler-delay profile and Doppler spectrum for the 1-km St. Margaret's test channel.

Channel matrix for 1 km channel was generated with the help of Model_SIMO_Bellhop_v1.m and is produced in Figure A.3 in a 3-D plot structure. An rms Doppler spread of 0.25 Hz per bounce at fc = 2048 Hz was assumed for the generation of SOS samples and the channel matrix.

For our simulations in chapter 7, we extracted a couple of test channels from 1-km channel experiment. This was done using arrival information from the 1 km channel in Model_SIMO_Bellhop_v1.m and setting Doppler per bounce to various values to have a realistic idea of the behavior of an acoustic environment with different Dopplers. The plots for channel matrices in time, frequency for all these channel scenarios are produced below along with other important specifications.

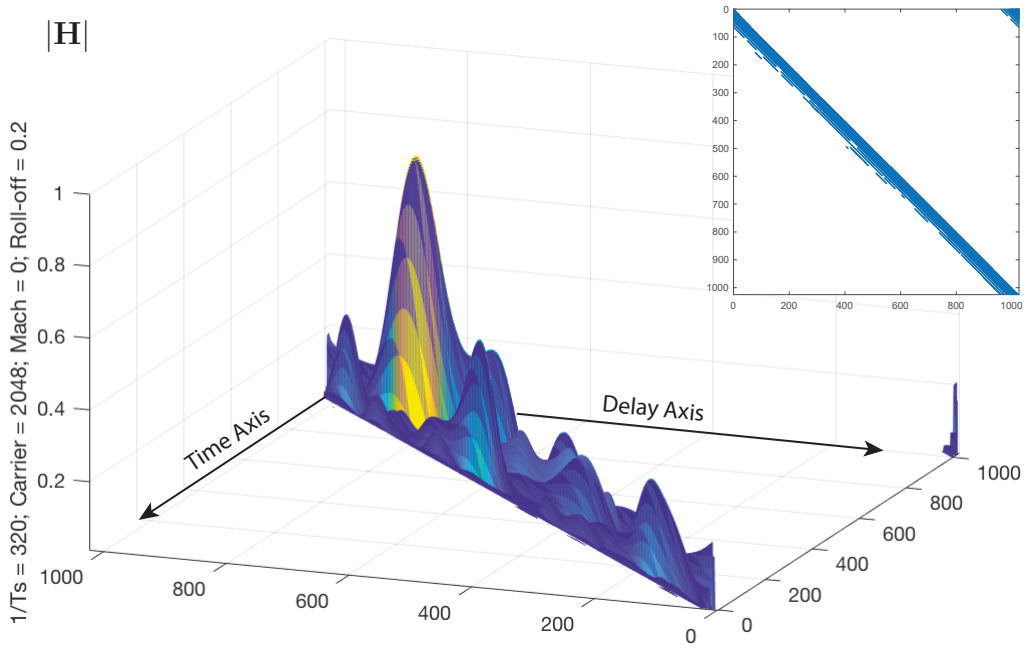

Figure A.3: Circulant channel matrix **H** for the 1-km St. Margaret's Bay channel.

channel-1

$$\begin{cases} \text{1 km channel,} \\ \text{Bandwidth, } B = 320;\ \text{Carrier Frequency, } fc = 2048;\ \text{Sampling Rate } = Ts = 0.0031\ s, \\ \text{Mean energy in } R^{(f)} \text{ over all hydrophones is -0.097979 dB,} \\ \text{Doppler (or ascal)= 0;}\ \text{Number of preambles used, } N_p = 8. \end{cases}$$

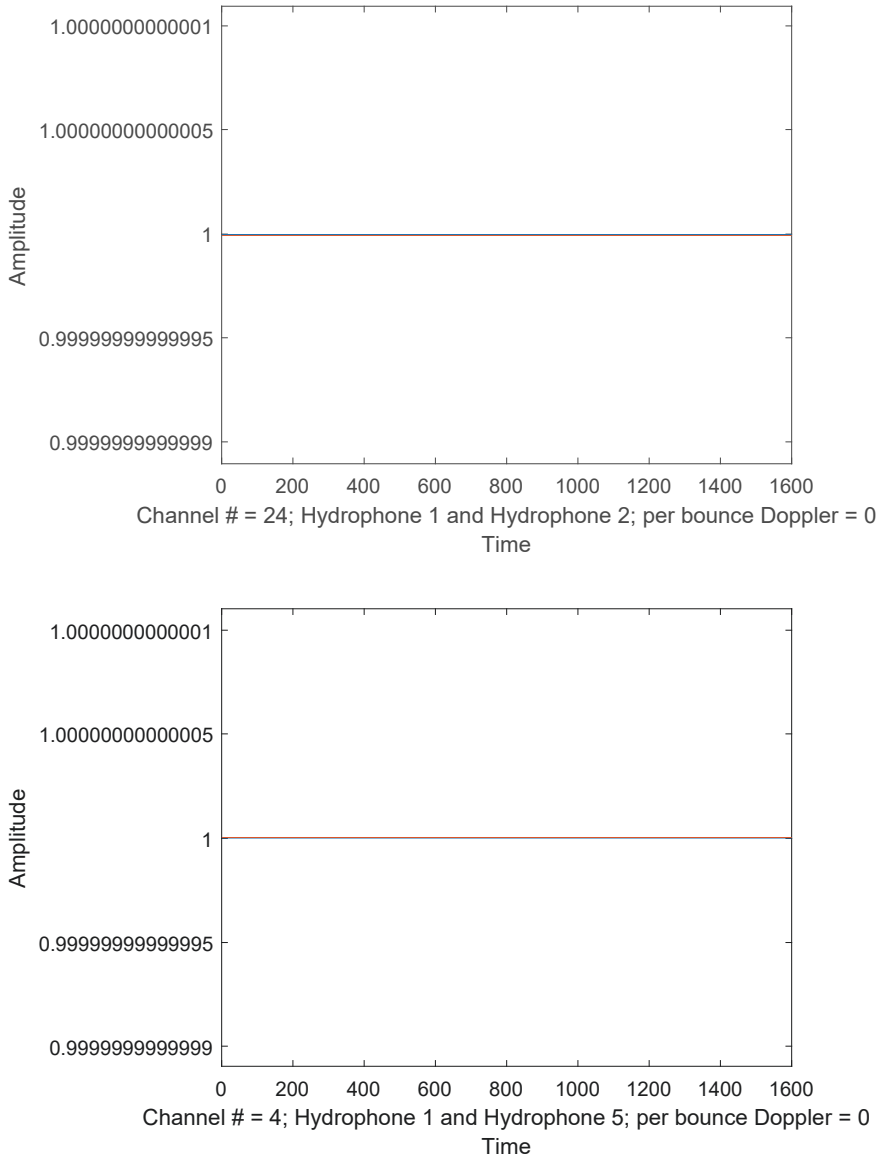

Figure A.4: Time variation of the 24th discrete tap at the 1st and 2nd, and of the 4th tap at the 1st and 5th hydrophones for Doppler factor $(ascal) = 0$.

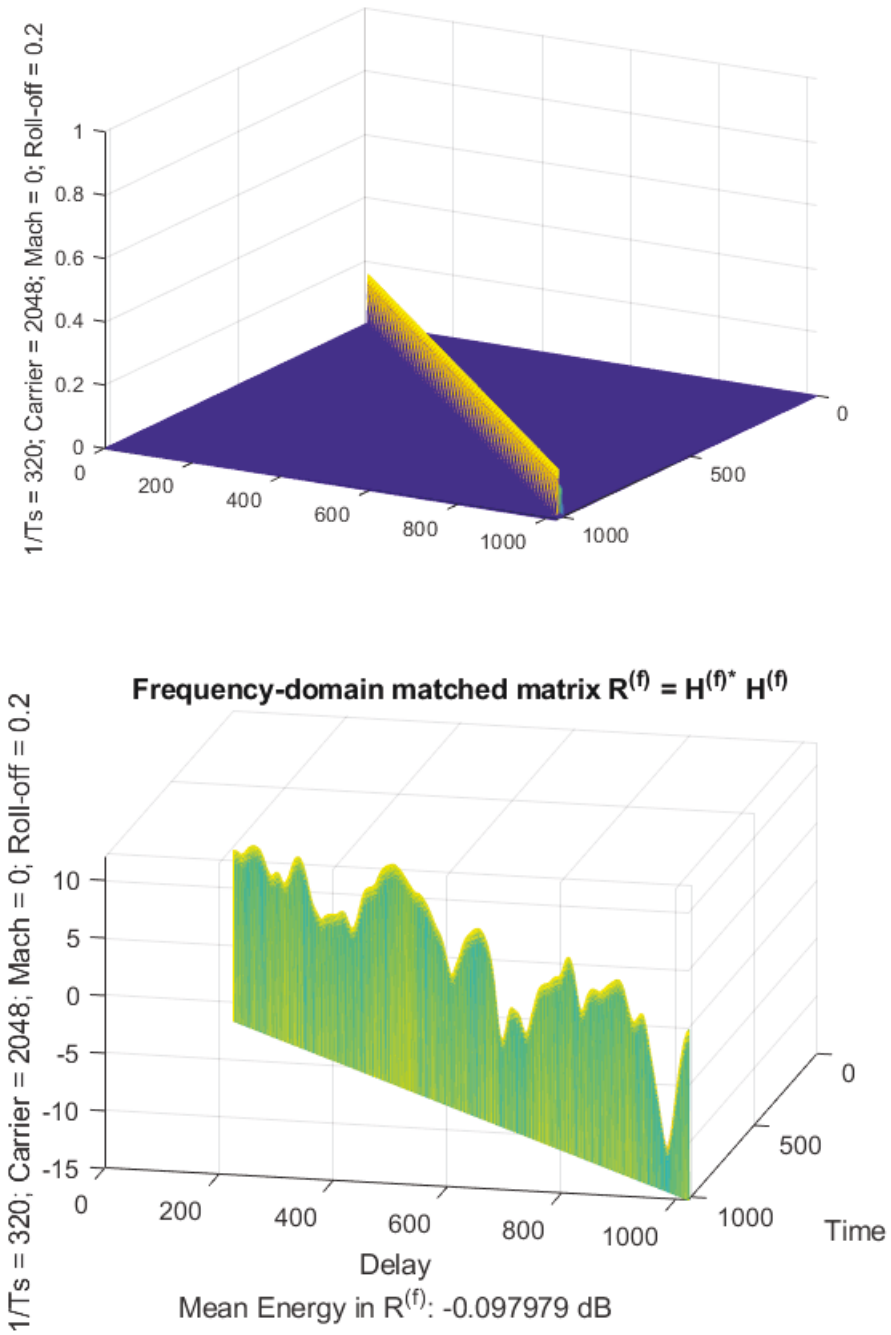

Figure A.5: Channel matrix, H, in time-delay and match-filtered H matrix in frequency domain for Doppler factor $(ascal) = 0$.

channel-2

$$\begin{cases} \text{1 km channel,} \\ \text{Bandwidth, } B = 320;\ \text{Carrier Frequency, } fc = 2048;\ \text{Sampling Rate } = Ts = 0.0031\ s, \\ \text{Mean energy in } R^{(f)} \text{ over all hydrophones is 0.18365 dB} \\ \text{Doppler (or ascal)= 0; Number of preambles used, } N_p = 8. \end{cases} \tag{A.1}$$

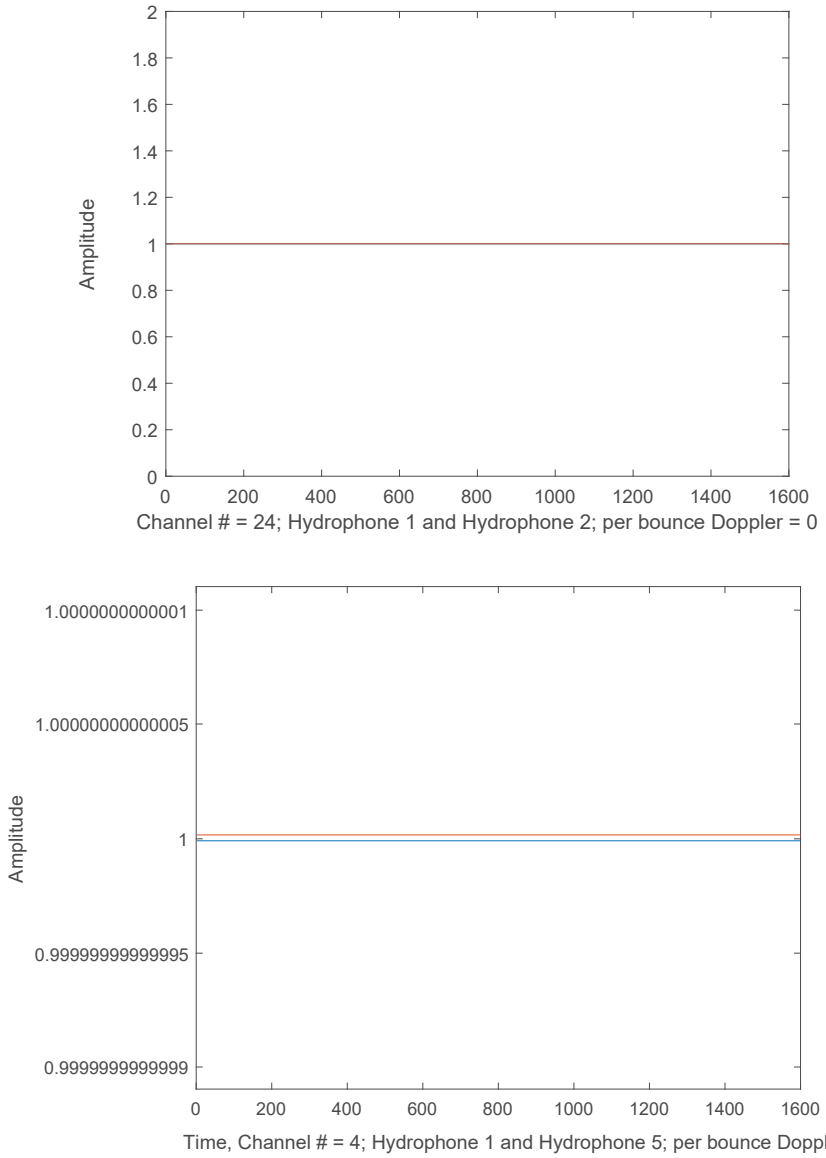

Figure A.6: Time variation of the 24th discrete tap at the 1st and 2nd, and of the 4th tap at the 1st and 5th hydrophones for Doppler factor $(ascal) = 0$.

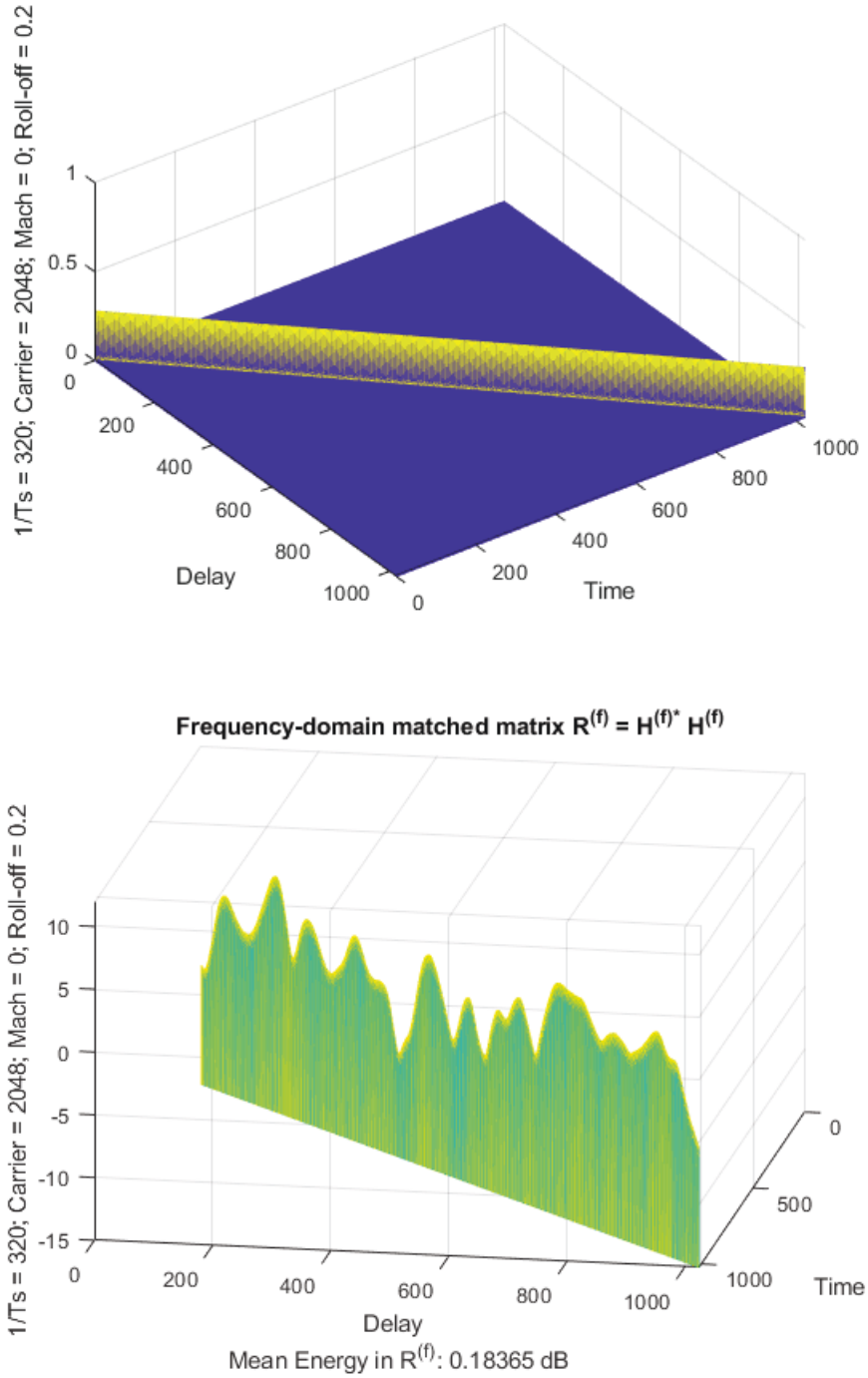

Figure A.7: Channel matrix, H, in time-delay and match-filtered H matrix in frequency domain for Doppler factor $(ascal) = 0$.

channel-3

$$\begin{cases} \text{1 km channel,} \\ \text{Bandwidth, } B = 1000;\ \text{Carrier Frequency, } fc = 3500;\ \text{Sampling Rate } = Ts = 10^{-3}\ s, \\ \text{Mean energy in } R^{(f)} \text{ over all hydrophones is -0.1926 dB,} \\ \text{Doppler (or ascal)= 0.001;}\ \text{Number of preambles used, } N_p = 8 \end{cases} \tag{A.2}$$

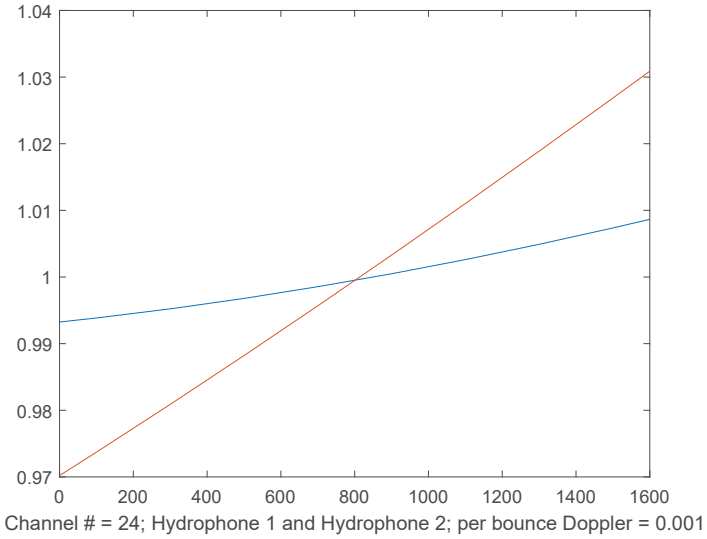

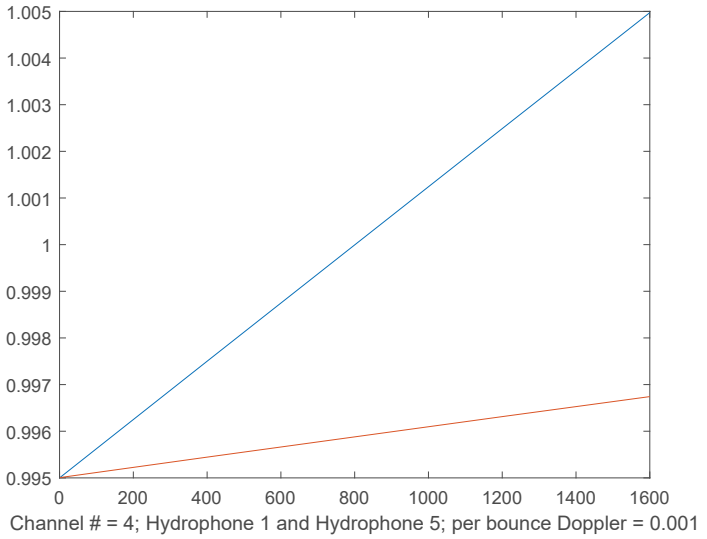

Figure A.8: Time variation of the 24th discrete tap at the 1st and 2nd, and of the 4th tap at the 1st and 5th hydrophones for Doppler factor $(ascal) = 0.001$.

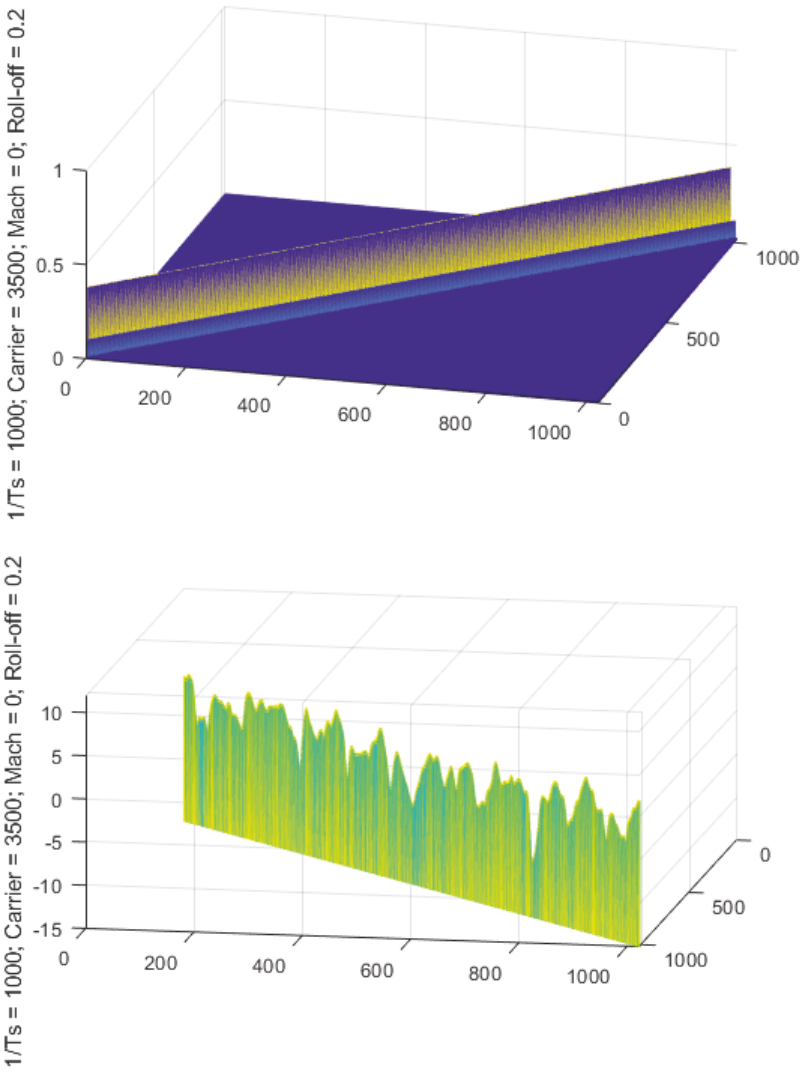

Figure A.9: Channel matrix, H, in time-delay and match-filtered H matrix in frequency domain for Doppler factor $(ascal) = 0.001$.

channel-4

$$\begin{cases} \text{1 km channel,} \\ \text{Bandwidth, } B = 320;\ \text{Carrier Frequency, } fc = 2048;\ \text{Sampling Rate } = Ts = 0.0031\ s, \\ \text{Mean energy in } R^{(f)} \text{ over all hydrophones is -0.0062121 dB,} \end{cases} \tag{A.3}$$

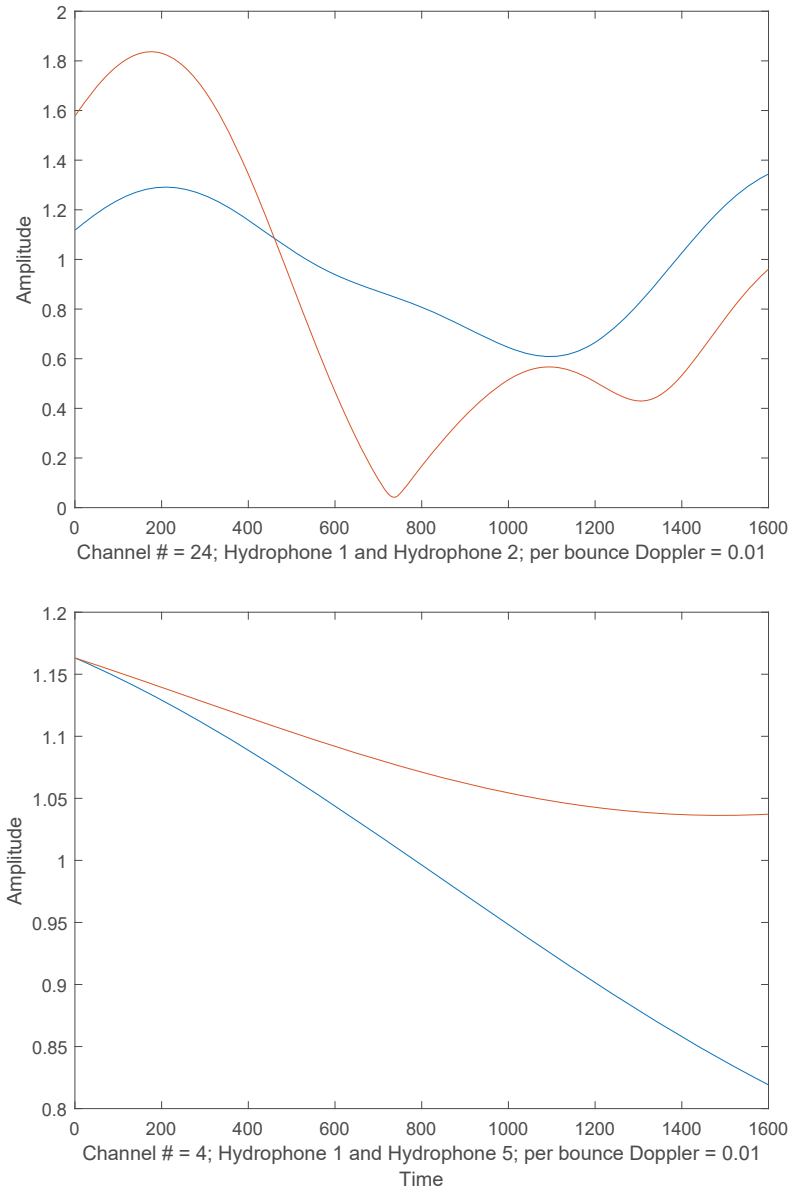

Figure A.10: Time variation of the 24th discrete tap at the 1st and 2nd, and of the 4th tap at the 1st and 5th hydrophones for Doppler factor $(ascal) = 0.01$.

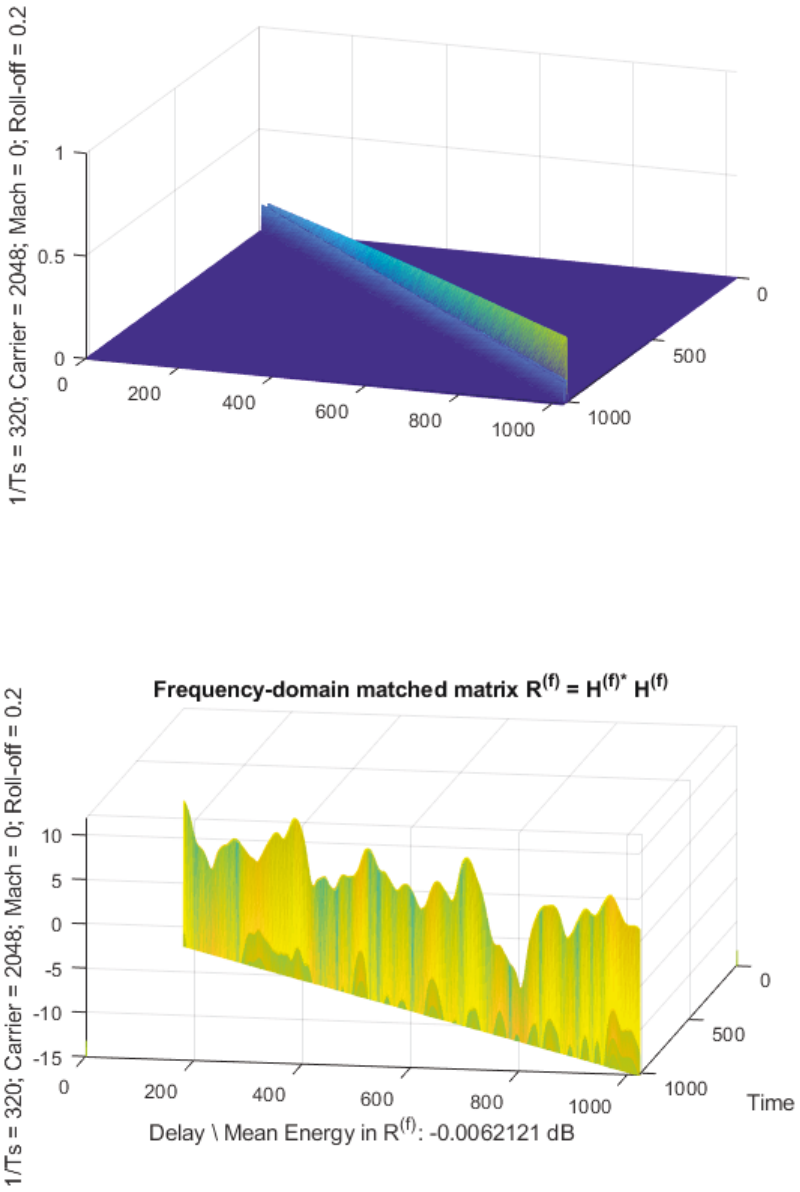

Figure A.11: Channel matrix, H, in time-delay and match-filtered H matrix in frequency domain for Doppler factor $(ascal) = 0.01$.

channel-5

$$\begin{cases} \text{1 km channel,} \\ \text{Bandwidth, } B = 320;\ \text{Carrier Frequency, } fc = 2048;\ \text{Sampling Rate } = Ts = 0.0031\ s, \\ \text{Mean energy in } R^{(f)} \text{ over all hydrophones is -0.856 dB,} \\ \text{Doppler (or ascal)= 0.25;\ Number of preambles used, } N_p = 8 \end{cases} \tag{A.4}$$

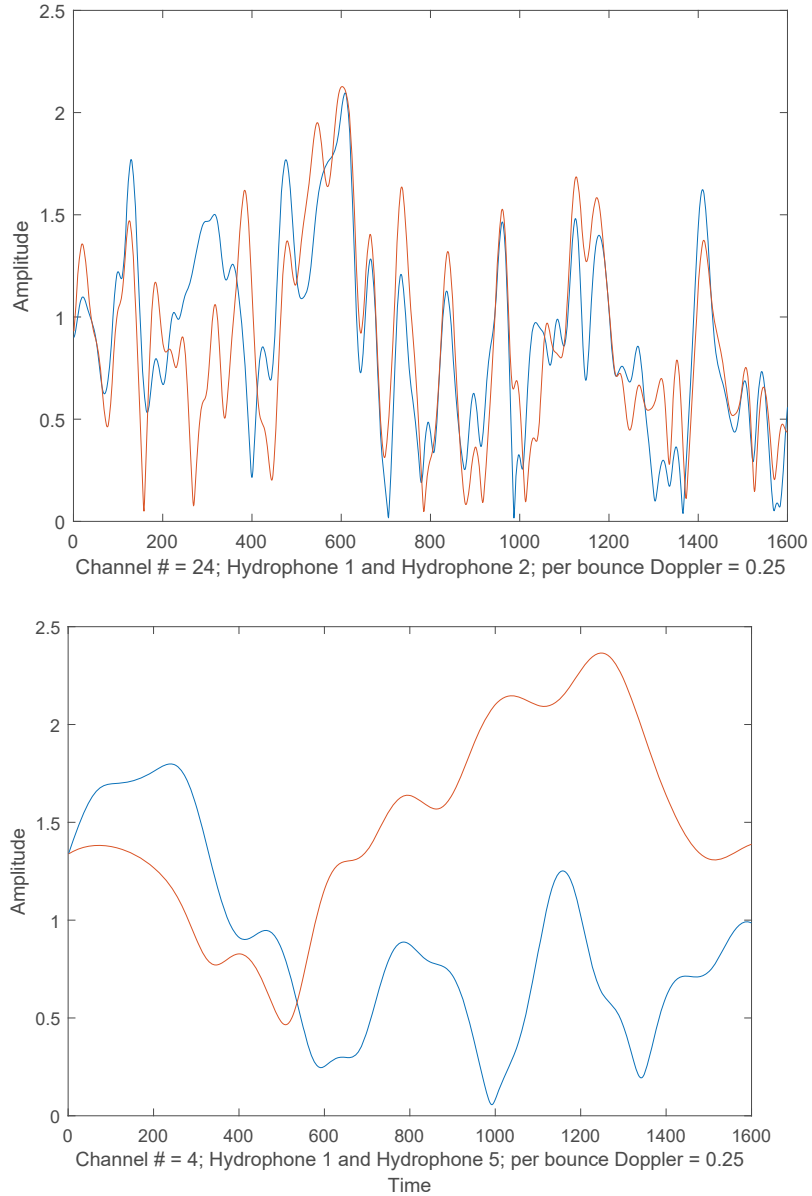

Figure A.12: Time variation of the 24th discrete tap at the 1st and 2nd, and of the 4th tap at the 1st and 5th hydrophones for Doppler factor $(ascal) = 0.25$.

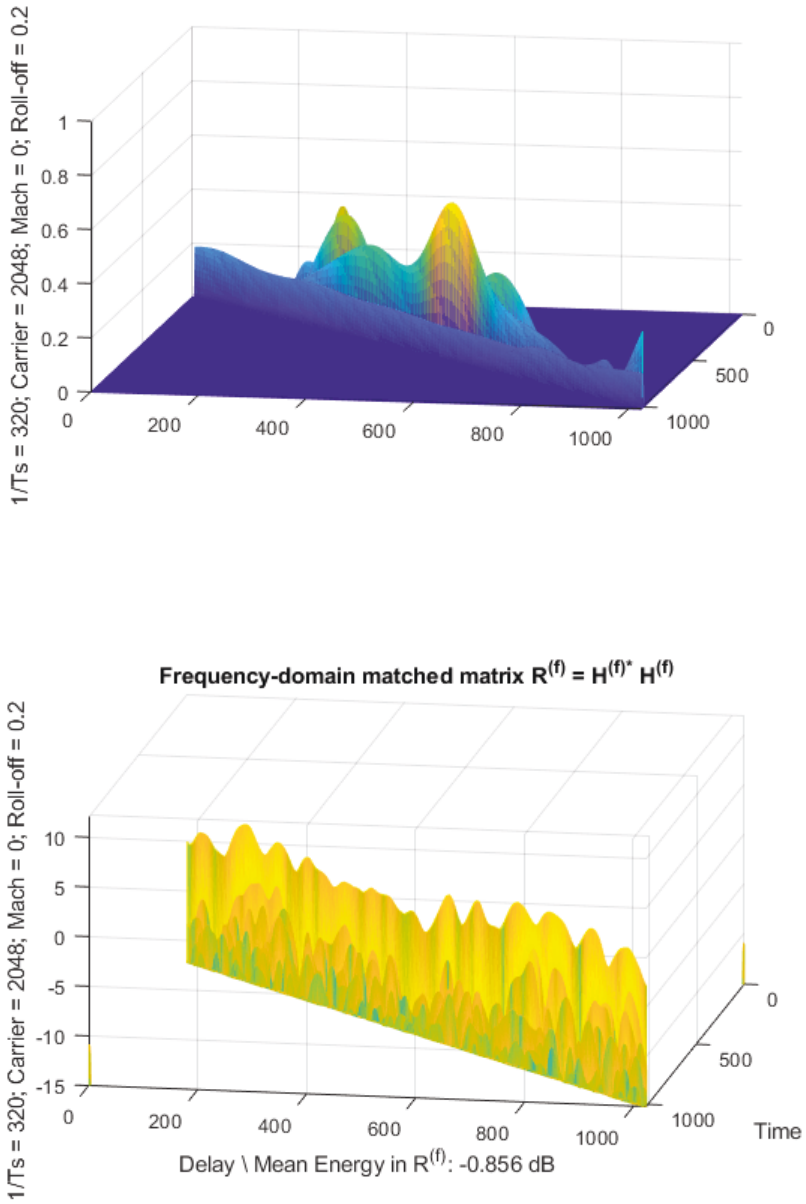

Figure A.13: Channel matrix, H, in time-delay and match-filtered H matrix in frequency domain for Doppler factor $(ascal) = 0.25$.

channel-6

$$\begin{cases} \text{1 km channel,} \\ \text{Bandwidth, } B = 320;\ \text{Carrier Frequency, } fc = 2048;\ \text{Sampling Rate } = Ts = 0.0031\ s, \\ \text{Mean energy in } R^{(f)} \text{ over all hydrophones is -1.2184 dB,} \\ \text{Doppler (or ascal)= 0.5;}\ \text{Number of preambles used, } N_p = 8 \end{cases} \tag{A.5}$$

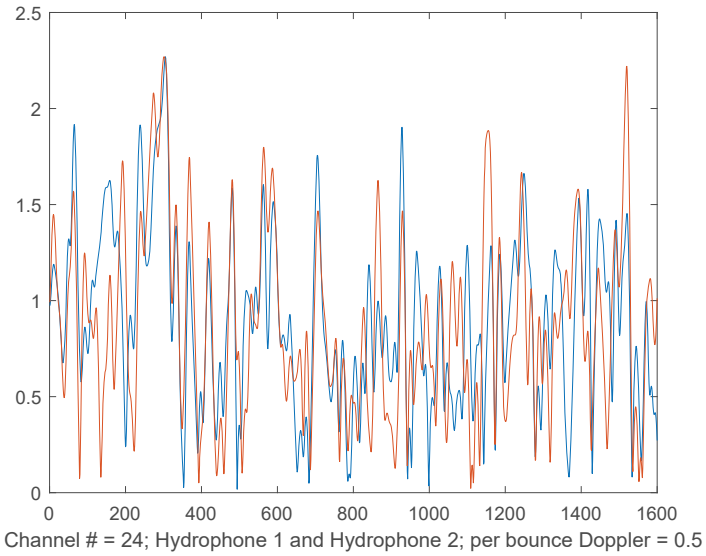

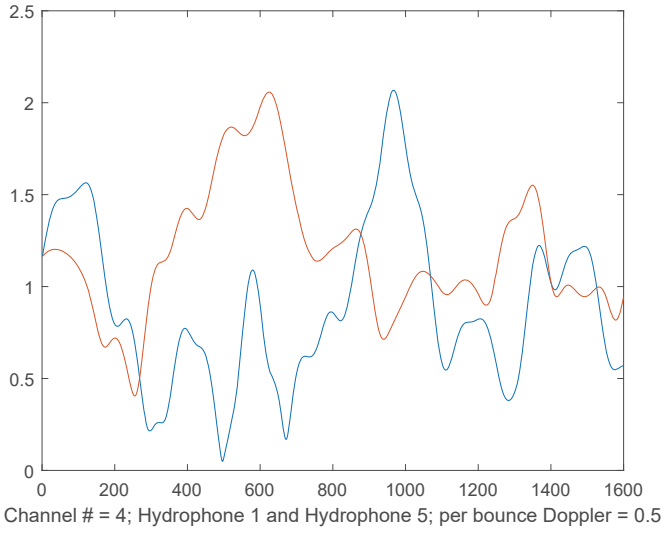

Figure A.14: Time variation of the 24th discrete tap at the 1st and 2nd, and of the 4th tap at the 1st and 5th hydrophones for Doppler factor $(ascal) = 0.5$.

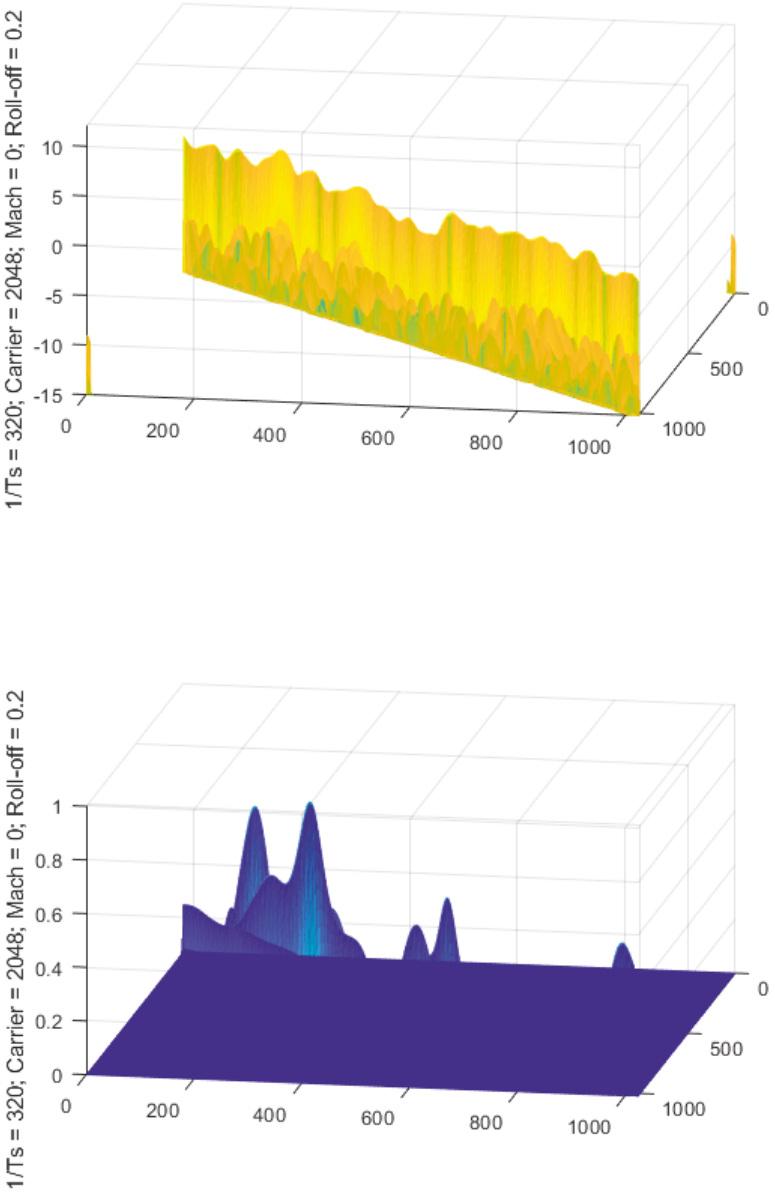

Figure A.15: Channel matrix, H, in time-delay and match-filtered H matrix in frequency domain for Doppler factor $(ascal) = 0.5$.

channel-7

$$\begin{cases} \text{1 km channel,} \\ \text{Bandwidth, } B = 320;\ \text{Carrier Frequency, } fc = 2048;\ \text{Sampling Rate } = Ts = 0.0031\ s, \\ \text{Mean energy in } R^{(f)} \text{ over all hydrophones is -0.29233 dB,} \\ \text{Doppler (or ascal)= 1;\ Number of preambles used, } N_p = 8 \end{cases} \tag{A.6}$$

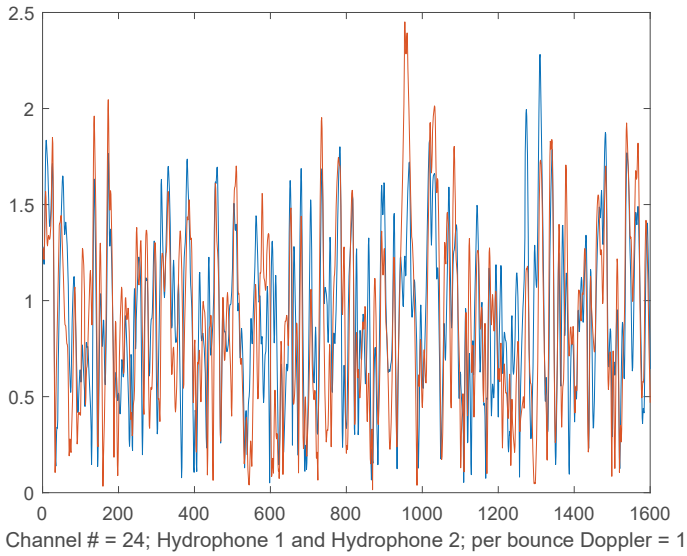

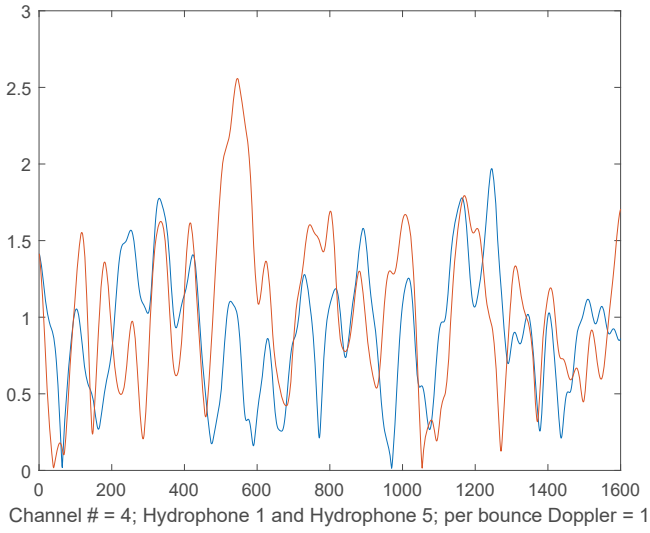

Figure A.16: Time variation of the 24th discrete tap at the 1st and 2nd, and of the 4th tap at the 1st and 5th hydrophones for Doppler factor $(ascal) = 1$.

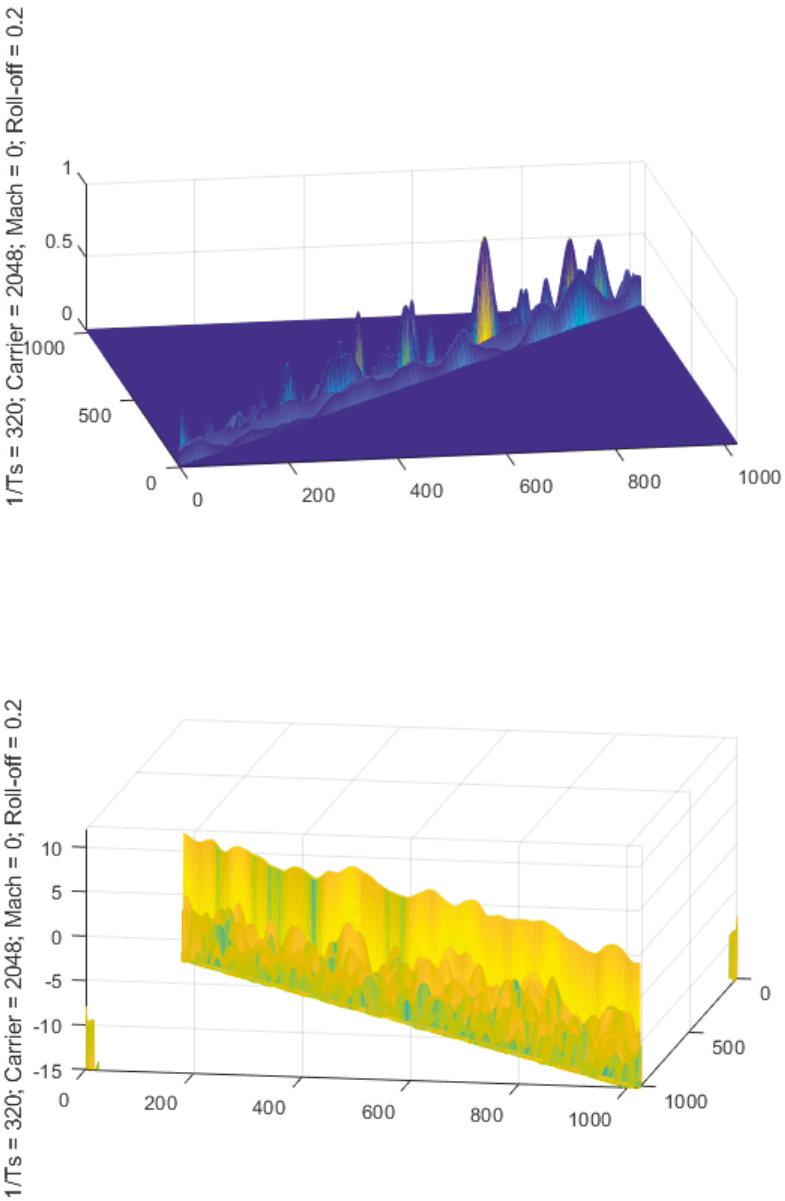

Figure A.17: Channel matrix, H, in time-delay and match-filtered H matrix in frequency domain for Doppler factor $(ascal) = 1$.

A.2 H.C. Song-Bellhop Channel

This channel is taken from literature as described in section 4.2. The channel matrices for this experiment as found from Bellhop simulations are shown here.

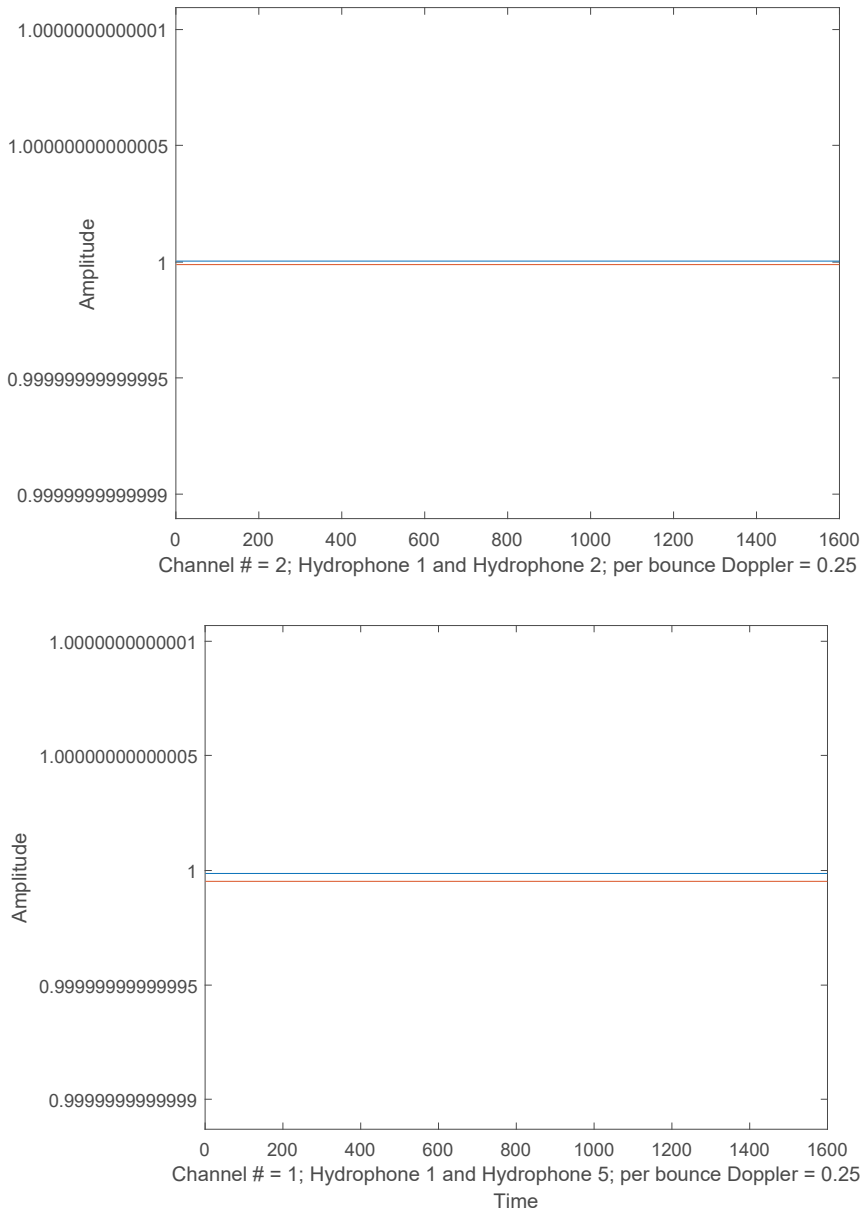

Figure A.18: Time variation of the 24th discrete tap at the 1st and 2nd, and of the 4th tap at the 1st and 5th hydrophones.

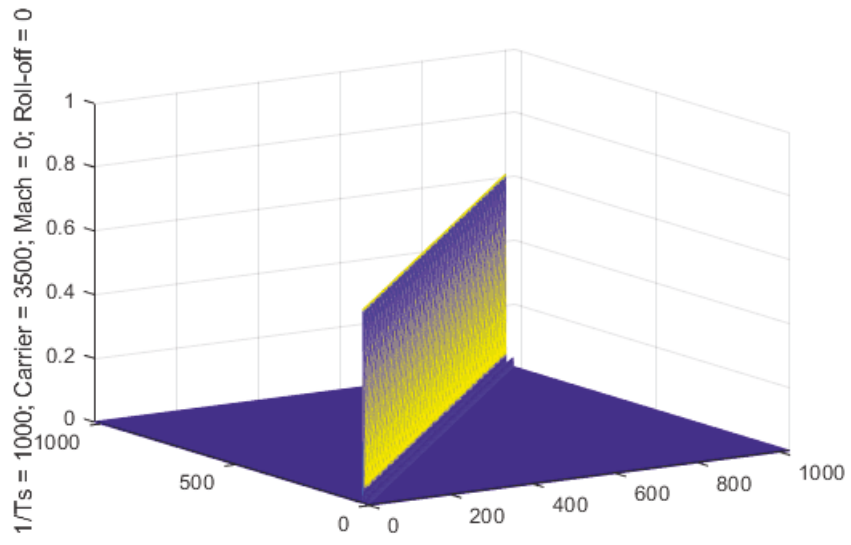
1/Ts = 1000; Carrier = 3500; Mach = 0; Roll-off = 0
1
0.8
0.6
0.4
0.2
0
1000
500
0
0
200
400
600
800
1000

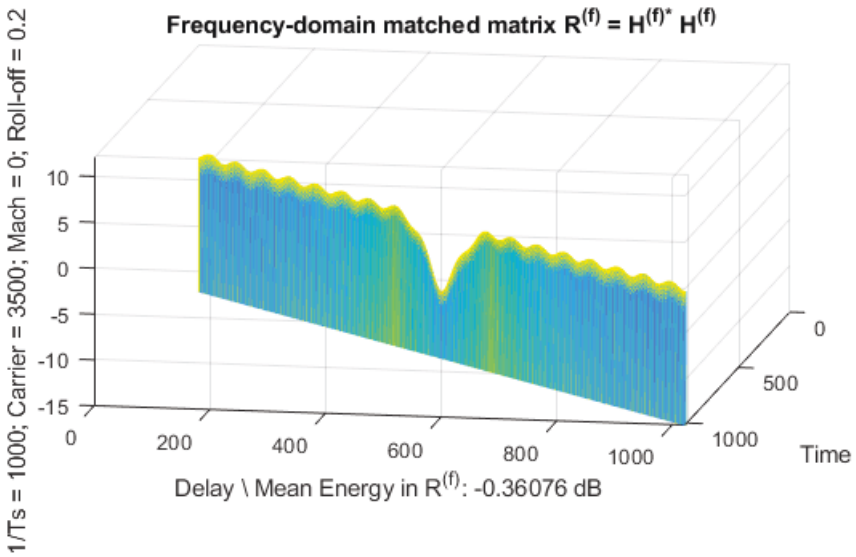
Frequency-domain matched matrix R(f) = H(f)* H(f)
1/Ts = 1000; Carrier = 3500; Mach = 0; Roll-off = 0.2
10
5
0
-5
-10
-15
0
200
400
600
800
1000
0
500
1000
Time
Delay \ Mean Energy in R(f): -0.36076 dB